

NKS-314  
ISBN 978-87-7893-393-5

---

# A study on the coolability of debris bed geometry variations using 2D and 3D models

Eveliina Takasuo, Veikko Taivassalo, Ville Hovi

VTT Technical Research Centre of Finland

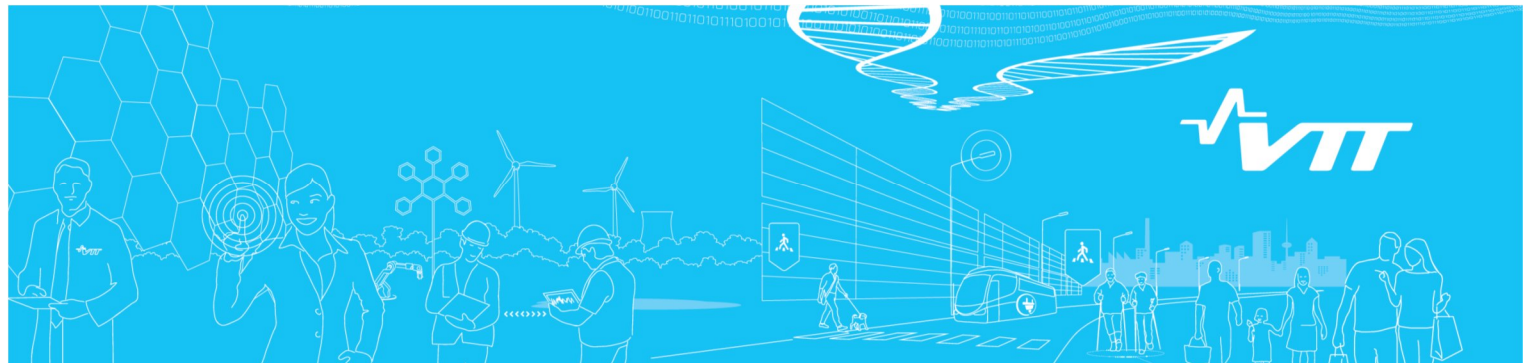
June 2014

## **Abstract**

In the first and second parts of the present work, the coolability of porous debris beds with different geometries (spatial distributions) has been assessed by using 2D and 3D simulation methods. The 2D simulations were conducted with the MEWA code by Stuttgart University. The 3D simulations were performed with the commercial CFD code Fluent, after the implementation of the porous media models as user defined functions into the code. The focus of the MEWA simulations was on the following multi-dimensionally flooded debris bed geometries: fully flooded cylinder (open sidewall and top), laterally flooded cylinder (open sidewall) and the cone on a closed cylindrical base. These geometries comprise the COOLOCE experimental series 10-12. In the Fluent simulations, the focus was on the verification of the model implementation, comparisons to MEWA results and the extension of the modelling approach to full 3D. Full 3D calculations were conducted for the conical test bed. In the third part, an insight into the uncertainty in the experimental determination of DHF is provided. Experiments with a top-flooded bed have been conducted with the COOLOCE facility at VTT and the POMECO facility at KTH with the same particle material. The comparisons revealed the effect of the non-modifiable part of the test set-up such as the heating and instrumentation systems.

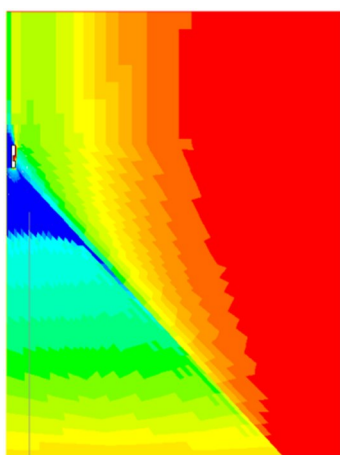
## **Key words**

severe accident, debris bed, coolability, numerical simulation, CFD



## RESEARCH REPORT










VTT-R-00676-14



# A study on the coolability of debris bed geometry variations using 2D and 3D models

Authors: Eveliina Takasuo, Veikko Taivassalo, Ville Hovi

Confidentiality: Public

<b>Report's title</b> A study on the coolability of debris bed geometry variations using 2D and 3D models					
<b>Customer, contact person, address</b> SAFIR2014 National Research Programme on Nuclear Power Plant Safety		<b>Order reference</b> 3/2012SAF			
<b>Project name</b> Core Debris Coolability		<b>Project number/Short name</b> 77466/COOLOCE-E			
<b>Author(s)</b> Eveliina Takasuo, Veikko Taivassalo, Ville Hovi		<b>Pages</b> 66			
<b>Keywords</b> nuclear power, severe accident, debris bed, coolability, numerical simulation, CFD		<b>Report identification code</b> VTT-R-00676-14			
<b>Summary</b> <p>In the first and second parts of the present work, the coolability of porous debris beds with different geometries (spatial distributions) has been assessed by using 2D and 3D simulation methods. The 2D simulations were conducted with the MEWA code by Stuttgart University. The 3D simulations were performed with the commercial CFD code Fluent, after the implementation of the porous media models as user defined functions into the code.</p> <p>The focus of the MEWA simulations was on the following multi-dimensionally flooded debris bed geometries: fully flooded cylinder (open sidewall and top), laterally flooded cylinder (open sidewall) and the cone on a closed cylindrical base. These geometries comprise the COOLOCE experimental series 10-12. In the Fluent simulations, the focus was on the verification of the model implementation, comparisons to MEWA results and the extension of the modelling approach to full 3D. Full 3D calculations were conducted for the conical test bed.</p> <p>In the third part, an insight into the uncertainty in the experimental determination of DHF is provided. Experiments with a top-flooded bed have been conducted with the COOLOCE facility at VTT and the POMECO facility at KTH with the same particle material. The comparisons revealed the effect of the non-modifiable part of the test set-up such as the heating and instrumentation systems.</p>					
<b>Confidentiality</b>	Public				
Espoo 10.2.2014 <table border="0"> <tr> <td style="vertical-align: top;"> <b>Written by</b>    Eveliina Takasuo  Senior Scientist </td> <td style="vertical-align: top;"> <b>Reviewed by</b>    Mikko Ilvonen  Principal Scientist </td> <td style="vertical-align: top;"> <b>Accepted by</b>    Anitta Hämäläinen  Research Team Leader </td> </tr> </table>			<b>Written by</b>  Eveliina Takasuo Senior Scientist	<b>Reviewed by</b>  Mikko Ilvonen Principal Scientist	<b>Accepted by</b>  Anitta Hämäläinen Research Team Leader
<b>Written by</b>  Eveliina Takasuo Senior Scientist	<b>Reviewed by</b>  Mikko Ilvonen Principal Scientist	<b>Accepted by</b>  Anitta Hämäläinen Research Team Leader			
<b>VTT's contact address</b> PO Box 1000, 02044-VTT, Finland					
<b>Distribution (customer and VTT)</b> SAFIR2014 Reference Group 5 VTT: Timo Vanttola, Kaisa Simola, Jari Hämäläinen, Vesa Suolanen					
<i>The use of the name of the VTT Technical Research Centre of Finland (VTT) in advertising or publication in part of this report is only permissible with written authorisation from the VTT Technical Research Centre of Finland.</i>					



## Contents

---

Contents.....	2
1. Introduction.....	3
2. Debris bed spatial configurations .....	4
3. Modelling principles .....	6
3.1 Drag force models .....	6
3.2 Heat transfer models.....	7
4. MEWA simulations.....	9
4.1 Fully flooded cylinder (COOLOCE-10) .....	9
4.2 Laterally flooded cylinder (COOLOCE-11) .....	14
4.3 Cone on a cylindrical base (COOLOCE-12).....	16
4.4 Summary .....	18
5. CFD simulations.....	20
5.1 Physical models and implementation .....	20
5.1.2 Turbulence modelling.....	22
5.1.3 Verification of the CFD implementation .....	24
5.2 Results .....	27
5.2.1 Cylindrical bed .....	27
5.2.2 Conical bed.....	28
5.2.3 Fully flooded cylinder .....	42
5.2.4 Laterally flooded cylinder .....	48
5.3 Summary .....	53
6. Experimental DHF comparisons (POMECO and COOLOCE) .....	55
6.1 Results.....	57
6.1.1 Size measurements of spherical particles .....	57
6.2 DHF results and comparisons.....	59
6.2.1 Analytical solution method .....	59
6.2.2 Analytical and experimental DHFs .....	60
6.3 Summary .....	63
7. Conclusions .....	63
References.....	64

## 1. Introduction

---

A debris bed (particle bed) that consists of fragmented and solidified corium may be formed as a result of a core melt accident in a nuclear power reactor. Depending on the design of the reactor, such a debris bed may be formed in the containment (ex-vessel) or inside the pressure vessel (in-vessel). The issue of corium coolability has received considerable attention since the accident at Fukushima in March 2011 which apparently resulted in various degrees of core melting in Units 1–3. In the Nordic type boiling water reactors in Finland and Sweden, the long-term cooling of the debris in a deep water pool in the containment has been adopted as a part of the severe accident management strategy.

In case of reactor pressure vessel failure, the molten corium is discharged into the lower drywell of the containment (flooded from the suppression pool) where the melt droplets are quenched by water and solidified into the form of particulate debris. The particles settle to the bottom of the pool forming a porous debris bed from which decay heat must be removed in order to prevent re-melting of the debris and possible large thermal loads to the containment structures. In this type of debris configuration, the heat removal is achieved mainly through the boiling of the coolant that infiltrates the pores of the bed. To ensure continuous cooling, it is important that the cooling water has adequate access into the pores of the debris bed to replace the evaporating mass flow. The limiting condition to the coolability in most studies is given by the dryout heat flux (or power density) which results in local loss of coolant, i.e. dryout. However, the final limit to whether a re-melting occurs is given by the temperature of the debris particles. In this study, the occurrence of dryout is primarily investigated but, in addition, we also examine the debris temperature increase in post-dryout conditions.

The formation of the debris bed is a stochastic process whose outcome cannot be fully predicted. In addition to the processes occurring in the water pool, the accident scenario has an effect on the final debris bed configuration. For instance, the pressure vessel failure mode, pressure and timing determine the melt jet speed, diameter and temperature which have an effect on the fragmentation and quenching processes and the final particle size. It is clear that the debris bed may be highly complex in terms of particle size, morphology and the spatial distribution (i.e. geometry) of particles, and it is not possible to take into account all possible debris beds in the evaluation of coolability. Therefore, the experimental and analytical research work has to focus on certain range of particle size, particle shape, porosity, debris bed geometry and flow mode which can be considered representative in a realistic severe accident scenario. The evaluation of representativeness is based on existing experimental data and the knowledge of the Three Mile Island accident.

The COOLOCE test facility is a laboratory-scale facility at VTT specifically designed to investigate the coolability of porous particle beds of different shapes (geometries) and flow modes. Different types of multi-dimensional flooding modes (achieved through different bed geometries) and their effect on the coolability have been examined. In this paper, we use “multi-dimensional flooding” to describe all types of flow modes not including pure top or bottom flooding which can be treated as one-dimensional flow in isotropic, homogenous beds. The COOLOCE experiments were started in 2010-2011 with the main objective of comparing the dryout power of a conical (heap-like) particle bed configuration to that of a cylindrical (evenly distributed) configuration (Takasuo et al. 2012a). In 2012, experiments were conducted with irregular gravel as the simulant material (COOLOCE-8) and initially subcooled pool (COOLOCE-9) (Takasuo et al. 2012b).

After this, the focus was again on the effect of different flow modes and geometries on coolability. A cylindrical bed with lateral and top flooding was investigated in COOLOCE-10 and a cylindrical bed with lateral flooding only in COOLOCE-11 (Takasuo et al. 2013a,b). In the former of the test series, all surfaces except bottom were open to flooding and in the latter an agglomerate simulant was placed on top of the test bed so that only lateral flooding was allowed. The COOLOCE-12 test series which examined a geometry variation

approximating a reactor scenario in which the debris bed has partially settled against the wall of the spreading area, with a conical heap of debris on the top (Takasuo et al. 2013c). The geometry is a cone on a cylindrical base, flooded through the surface of the conical part and with impermeable sidewall in the cylindrical part. Simulations suggest that this type of debris bed may be formed as a result of spreading of the debris particles by natural circulation flows in the pool.

The validation of simulation codes against experiments is a crucial part of the coolability research. Reactor scale experiments are non-existent which means that the reactor scenarios have to be analysed using simulation codes. The comparison of simulations and experiments reveal how well the simulations and the applied models are capable of reproducing the real-world dryout behaviour. Validation of the simulation codes is the main objective of the present work. From the experimental studies, this requires that the experiments are well-designed so that the behaviour of the realistic debris bed is adequately reproduced with the experimental facility. For instance, the particles in experiments are often heated by electrical resistance heaters with no internal heating. Different types of heating methods have been applied in the past experiments but, to the authors' knowledge, no direct comparisons or cross-checking of the results between different experimental facilities have been performed. Such a comparative study is presented in this report, in addition to the coolability simulations.

The presented work consists of three parts. Firstly, we present the **2D simulations of three different multi-dimensionally flooded debris bed configurations** and compare the simulated dryout power to the experimental results. The top-flooded configuration (experiments COOLOCE-3-5) serves as a reference case against which the multi-dimensionally flooded cases are compared in order to find out which geometries are easily coolable and which are less so. The simulations have been conducted with the MEWA code (Bürger et al. 2006).

Secondly, the **simulations of the different debris bed geometries by using a CFD type approach are presented**. This is the first attempt known to the authors to model debris bed dryout by using a multi-purpose CFD solver. The work was motivated by the interest to take the modelling to a more detailed level by including the possibility to account for irregular (non-symmetric) bed geometries and a more realistic model for the water pool. The main differences compared to the 2D approach are discussed.

Finally, an **insight into the uncertainty in the experimental determination of DHF is provided**. Experiments with a top-flooded bed have been conducted with the COOLOCE facility at VTT and the POMEKO facility at KTH (Kudinov et al. 2013). The simulant material and the other test parameters were as similar as possible in the two experiments which facilitates the estimation of the effect of the non-modifiable part of the test set-up such as the heating and instrumentation systems.

## 2. Debris bed spatial configurations

Five different debris bed spatial distributions, i.e. geometries, have been addressed in the COOLOCE experiments. The conceptual images of the geometries are illustrated in Fig. 1. The MEWA simulations in this report focus on the modelling of geometries (c) the cylindrical bed with flooding through both top and sidewall (fully flooded cylinder), (d) cylinder with blocked top to simulate a large agglomerate (laterally flooded cylinder) and (e) the conical bed with a cylindrical bottom. In the CFD simulations, the conical debris bed (a), the fully flooded cylinder (c) and the laterally flooded cylinder (d) are emphasized. In addition, the implementation of the models to the CFD solver is verified by 3D calculations of a simple 1D geometry and the basic top-flooded cylinder (b) is briefly discussed.

The height of all the test beds is 270 mm. The base diameter of the fully conical bed is 500 mm and the diameter of the cylindrical beds is approximately 310 mm. The decay heat is simulated by resistance heating and dryout is determined based on temperature increase measured with thermocouples. The test facility has been described in several previous reports (Takasuo et al. 2012b and 2013a,b,c) and a journal article by Takasuo et al. (2012a).

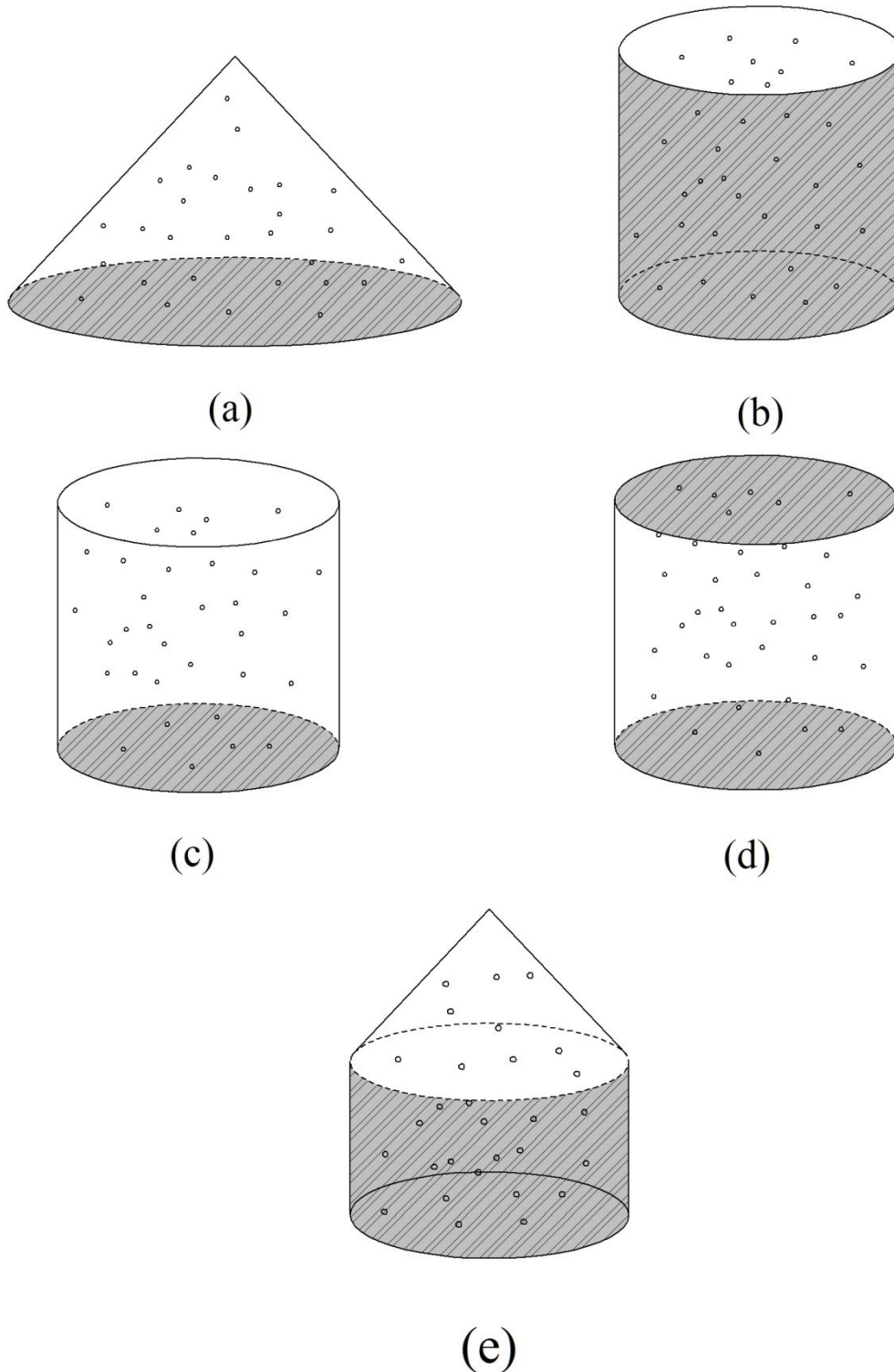


*Fig. 1. Debris bed geometries in the COOLOCE experiments: (a) conical bed, (b) top-flooded cylindrical bed, (c) fully flooded cylinder, (d) cylinder with lateral flooding only and (e) conical heap on a closed cylindrical base (impermeable walls darkened).*

### 3. Modelling principles

The multi-dimensional modelling of the debris bed dryout behaviour is based on solving the two-phase flow conservation equations, namely, the mass, momentum and energy conservation for the gas and liquid phases. The closure models for the frictional forces and heat transfer are well-known models found in the literature. The general form of the conservation equations is given below. The mass conservation is

$$\frac{\partial}{\partial t}(\varepsilon\alpha_i\rho_i) + \nabla \cdot (\varepsilon\alpha_i\rho_i\vec{v}_i) = \Gamma \quad (1)$$

where  $\varepsilon$  is porosity (-),  $\alpha_i$  is the volume fraction of the phase  $i$  ( $i=g, i=l$ ),  $\rho_i$  is the phase density ( $\text{kg/m}^3$ ),  $\vec{v}_i$  is phase velocity ( $\text{m/s}$ ) and  $\Gamma$  is the source term due to evaporation ( $\text{kg/m}^3/\text{s}$ ). The momentum equation is

$$\frac{\partial}{\partial t}(\varepsilon\alpha_i\rho_i\vec{v}_i) + \nabla \cdot (\varepsilon\alpha_i\rho_i\vec{v}_i\vec{v}_i) = -\varepsilon\alpha_i\nabla p_i + \varepsilon\alpha_i\rho_i\vec{g} + \nabla \cdot (\varepsilon\alpha_i\vec{\tau}_i) + \vec{F}_{s,i} + \vec{F}_i \quad (2)$$

where  $p_i$  is pressure (Pa),  $\vec{\tau}_i$  is the viscous stress tensor ( $\text{N/m}^2$ ),  $\vec{F}_{s,i}$  is the drag force between the solid particles and the fluid phase  $i$  ( $\text{N/m}^3$ ) and  $\vec{F}_i$  is the interfacial drag (gas-liquid drag) on the phase  $i$  ( $\text{N/m}^3$ ). The energy conservation equation for the fluid phases is

$$\frac{\partial}{\partial t}(\varepsilon\alpha_i\rho_i h_i) + \nabla \cdot (\varepsilon\alpha_i\rho_i\vec{v}_i h_i) = \nabla \cdot (\lambda_{eff,i}\nabla T_i) + Q_{s,i} + Q_{evap,i} \quad (3)$$

where  $h_i$  is the specific enthalpy of phase  $i$  ( $\text{J/kg}$ ),  $T_i$  is the phase temperature (K),  $Q_{s,i}$  is the heat flux from the solid phase to the fluid ( $\text{W/m}^3$ ) and  $Q_{evap,i}$  is the heat flux by evaporation ( $\text{W/m}^3$ ). The effective thermal conductivity  $\lambda_{eff,i}$  ( $\text{W/m/K}$ ) is calculated from the phase thermal conductivity,  $\lambda_{eff,i} = \lambda_i\varepsilon\alpha_i$ . In addition, energy conservation is solved for the solid phase:

$$\frac{\partial}{\partial t}((1-\varepsilon)\rho_s h_s) = \nabla \cdot (\lambda_{eff,s}\nabla T_s) + Q_{s,decay} - Q_{s,sat} - Q_{s,g} - Q_{s,l} \quad (4)$$

where  $Q_{s,decay}$  is the internal heat source of the material (decay heat or test facility heaters),  $Q_{s,sat}$  is the heat flux directed to evaporation and  $Q_{s,g}$  and  $Q_{s,l}$  are the heat fluxes from the solid particles directly to the fluid phases ( $Q_{s,l}$  is important mainly in dryout conditions and  $Q_{s,l}$  if the liquid phase is subcooled). For the effective thermal conductivity of the porous medium  $\lambda_{eff,s}$ , a separate model that accounts for convection and radiation is applied (Imura & Takegoshi, 1974, and Vortmeyer, 1978).

#### 3.1 Drag force models

In the MEWA 2D code, a simplified form of the momentum equations is used in which viscous stress term is not taken into account. For the drag forces between the solid and the fluid phases  $\vec{F}_{s,i}$  in Eq. (2), let us write  $\vec{F}_{s,l}$  for the liquid-solid drag and  $\vec{F}_{s,g}$  for the liquid-gas drag, and  $\alpha = \alpha_g$  for the void fraction. The drag forces are expressed as functions of superficial phase velocity  $\vec{j}_i$  by using the concepts of permeability  $K$  and passability  $\eta$ , and relative permeability  $K_r$  and relative passability  $\eta_r$ :

$$\vec{F}_{s,l} = \varepsilon(1-\alpha) \left( \frac{\mu_L}{KK_{rl}} \vec{j}_l + \frac{\rho_L}{\eta\eta_{rl}} |\vec{j}_l| \vec{j}_l \right) \quad (5)$$

$$\vec{F}_{s,g} = \varepsilon \alpha \left( \frac{\mu_g}{K K_{rg}} \vec{J}_g + \frac{\rho_g}{\eta \eta_{rg}} |\vec{J}_g| \vec{J}_g \right) \quad (6)$$

The relation between the physical and superficial velocities is

$$\vec{J}_l = \varepsilon (1 - \alpha) \vec{v}_l \quad (7)$$

$$\vec{J}_g = \varepsilon \alpha \vec{v}_g \quad (8)$$

Permeability and passability describe the capability of porous medium to transmit fluid. They are expressed according to Ergun (1952) as

$$K = \frac{\varepsilon^3 d^2}{150(1 - \varepsilon)^2} \quad (9)$$

$$\eta = \frac{\varepsilon^3 d}{1.75(1 - \varepsilon)} \quad (10)$$

The presence of the other fluid phase in the two-phase flow is taken account by using relative permeability  $K_r$  (-) and relative passability  $\eta_r$  (-) which are functions of the void fraction

$$K_{rl} = (1 - \alpha)^n, K_{rg} = \alpha^n \quad (11)$$

$$\eta_{rl} = (1 - \alpha)^m, \eta_{rg} = \alpha^m \quad (12)$$

The powers of relative permeability and passability depend on the author (and the respective experiments). For the relative permeability,  $n = 3$  is typically used. For the relative passability, Lipinski (1982) suggested  $m = 3$ . Reed (1982) suggested  $m=5$  which yields a somewhat increased friction and was later used also by Lipinski (1984). Later, Hu and Theofanous (1991) proposed  $m=6$ . These three models that differ from each other only in the relative passability are the “classical” models used to predict the formation of dryout with no consideration of the gas-liquid drag. As the empirical models aim to describe the total pressure loss, the gas-liquid drag is implicitly included in the models.

In the models that account for the interfacial drag term  $\vec{F}_l$ , there are two alternative approaches. Schulenberg & Müller (1986) proposed an empirical correlation for the interfacial drag based on pressure measurements. Tung and Dhir (1988) developed a more detailed model in which the drag coefficients are calculated according to flow regimes which were determined based on visual observations. The Tung and Dhir model was later modified by Schmidt (2004) and Rahman (2013) to increase the capability of the model to predict dryout heat flux in both top and bottom flooding conditions. The detailed description of the models with interfacial drag (as well as the other models applied in MEWA) can be found in Rahman (2013).

## 3.2 Heat transfer models

Initially and in pre-dryout conditions in the simulations, the solid particles, liquid and gas are practically in thermal equilibrium at saturation temperature. Heat is transferred from the debris mainly by phase change of water to steam. The heat transfer from the solid particles to steam becomes important in near-dryout conditions and especially after dryout has been reached and the temperature of the solid starts to increase. The boiling rate is calculated by dividing the heat flux from the solid with the latent heat of evaporation:



$$\Gamma = \frac{Q_{s,sat}}{\Delta H_{evap}} \quad (13)$$

To calculate the boiling heat transfer coefficient, the Rohsenow correlation (Rohsenow, 1952) is applied for nucleate pool boiling regime and the Lienhard correlation (Lienhard, 1987) for the film boiling regime (with transition zone calculated by an interpolation function). Heat transfer from solid to steam is assumed to occur when the solid temperature is above saturation temperature and the gas fraction is 0.7 or greater. The heat flux from solid to gas is

$$Q_{s,g} = a_{s,g} h_{s,g} (T_s - T_g) \quad (14)$$

The interfacial area density is obtained from porosity and the particle diameter  $D_p$ :

$$a_{s,g} = \frac{6 \cdot (1 - \varepsilon)}{D_p} F(\alpha) \quad (15)$$

$$F(\alpha) = \begin{cases} 0 & \text{if } \alpha < 0.7 \\ \frac{\alpha - 0.7}{0.3} & \text{if } \alpha \geq 0.7 \end{cases} \quad (16)$$

The heat transfer coefficient from solid to steam is

$$h_{s,g} = \frac{Nu_{s,g} \lambda_g}{D_p} \quad (17)$$

The Nusselt number is calculated according to the Ranz-Marshall correlation (1952):

$$Nu_{s,g} = 2 + 0.6 \sqrt{Re_g} \cdot \sqrt[3]{Pr_g} \quad (18)$$

where the Reynolds number is

$$Re_g = \frac{|\vec{v}_g \rho_g D_p|}{\eta_g} \quad (19)$$

In MEWA, this correlation is applied in the form that omits the Prandtl number term, shortening the correlation to

$$Nu_{s,g} = 2 + 0.6 \sqrt{Re_g} \quad (20)$$

The MEWA documentation does not give explanation to the omission but, apparently, it is because the cubic root of the Prandtl number is very close to 1.0 due to the low thermal conductivity of the steam phase.

## 4. MEWA simulations

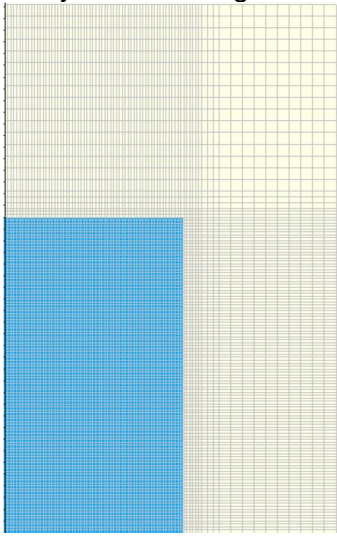
The 2D simulations were performed with the MEWA code, a dedicated severe accident code that has been developed by the University of Stuttgart (IKE Institute). The code has been used at VTT throughout the COOLOCE project to model the performed experiments. In the MEWA simulations, the main focus is on comparing the experimental and simulated dryout power with the objective of finding out how well the dryout power is predicted by the models for the pressure range of the experiments. In previous studies of the conical and cylindrical debris beds, the agreement between the experiments and simulations ranged from very good to reasonable (Takasuo et al. 2012c).

### 4.1 Fully flooded cylinder (COOLOCE-10)

The motivation for the fully flooded cylinder experiment was to investigate a general approximation of a heap-like bed without the sharp tip (apex) of the fully conical bed. It has been shown that dryout typically occurs in the tip of the cone, i.e. at the highest point of the geometry, in a small region where the highest amount of steam (and the longest distance from the bottom to the “outlet”) can be found. However, it is not certain that such a tip is always formed in a heap-like bed. This is why other geometries, in addition to the conical bed, which combine lateral and top flooding should be considered in order to achieve a good basis for the model and code validation.

The MEWA simulation set-up and the computational grid for the fully flooded cylinder are presented in Table 1. The porosity is taken as measured for the experimental bed based on the particles mass and the particle diameter is the mean diameter of the ceramic beads (see Section 6.1.1). It is noteworthy that homogenous heating (uniform power density) is applied in the porous region.

Table 1. Simulation set-up for C-10.

Particle diameter	0.97 mm	Axisymmetric 2D grid 
Porosity	0.392	
Material density	4200 kg/m <sup>3</sup>	
Thermal conductivity	2.0 W/mK	
Specific heat capacity	775 J/kgK	
Grid cell size in porous zone	2.5 mm x 2.5 mm	
Time step size	Controlled by the code, 1.0e-6 – 2.0s	
Heating method	Homogenous (constant power density)	
Pressure	Experimental, 1.3-2.93 bar	
Boundary conditions (top)	Pressure, saturated liquid inflow	
Boundary conditions (side and bottom)	Adiabatic, no flow-through	

In MEWA, the pool is not distinguished from the porous bed with separate “free-flow” models. In the pool region, the porous media model is used to produce some background friction representing significantly smaller flow resistance than in the porous region. Here, we use 99% porosity and 10 mm particle diameter. Thus, the starting point is that the drag forces of a real bubbly flow in a pool are not mechanistically reproduced.



The simulated dryout power using the drag force models of Reed, Tung & Dhir (TD) and modified Tung & Dhir (MTD) is compared to the experimental results in Fig. 2. It was found that the dryout power is somewhat dependent on the drag force model. The best apparent prediction is obtained using the Reed model. The TD model and especially the MTD model overestimate DHF by 15-30%. The differences between the models are seen in the saturation and temperature distributions obtained with the three models, illustrated in Fig. 3 - Fig. 5. The illustrations show the steady-state (or quasi-steady-state) to which the simulated system stabilizes at the dryout power level at the pressure of 2.0 bar. For clarity, the graphs are shown with and without velocity vectors.

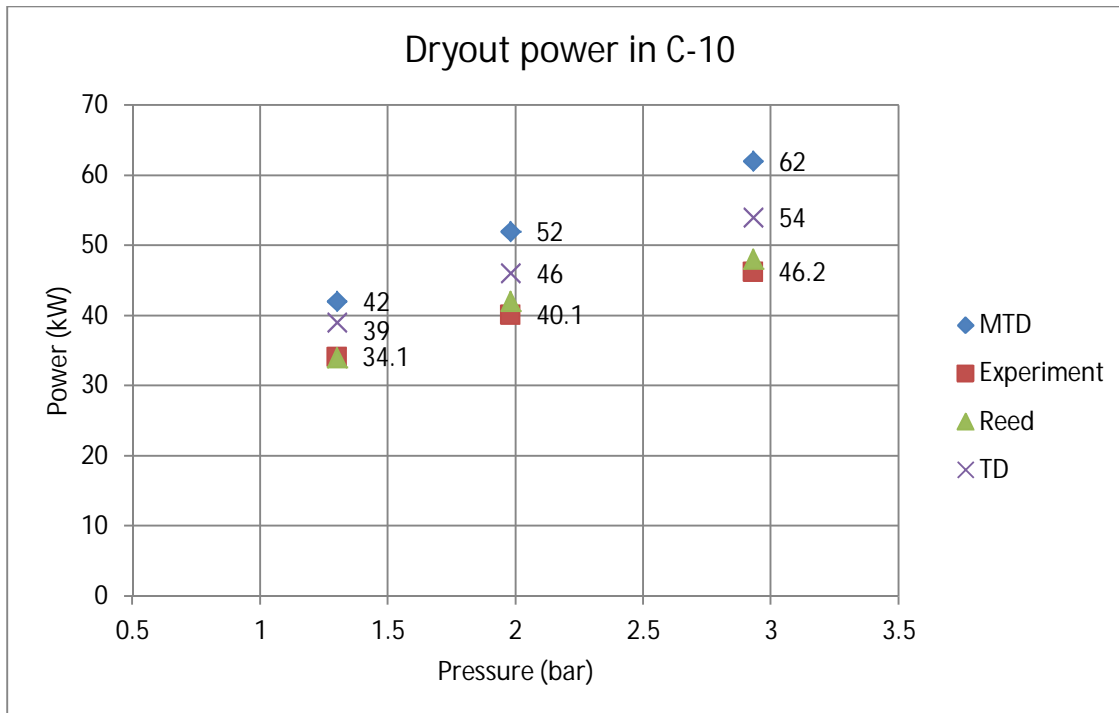


Fig. 2. Experimental and simulated dryout power in C-10 (fully flooded cylinder).

In general, the models correctly predict that dryout is formed in the upper part of the geometry. Below the height of 0.2 m, the saturation distributions are very similar in all the cases. In the models in which the gas-liquid drag is accounted for, a strong circulation is formed in the pool since the steam flow that escapes the debris bed accelerates the water flow. In the Reed model, there is no such interaction between steam and water, and water flows slowly through the pool region to replace the evaporating water in the porous zone. Also, the steam flow that exits from the porous zone is directly upwards, instead of being drawn towards the axis which is the case in the models with interfacial drag.

Based on the results, straightforward recommendations for the model selection are difficult to give. The best overall coolability is predicted by the Reed model but, due to the absence of the interfacial drag, the model cannot be considered to yield realistic results in the pool region. Moreover, studies suggest that the interfacial drag term is required to capture the pressure gradient correctly also in porous media which is important in estimating the coolability of debris beds with co-current flow (e.g. Schmidt, 2004).

The MTD model predicts that the dry zone is formed in the middle of the bed radius. Considering the 3D cylinder that is represented by the axisymmetric model, this would mean that the dry zone forms a ring near the surface of the debris bed which does not seem a very realistic shape for the dryout zone. The Reed model gives a somewhat similar dry zone (seen especially in the solid temperature graphs) but the point of minimum saturation is more localized in the MTD model.

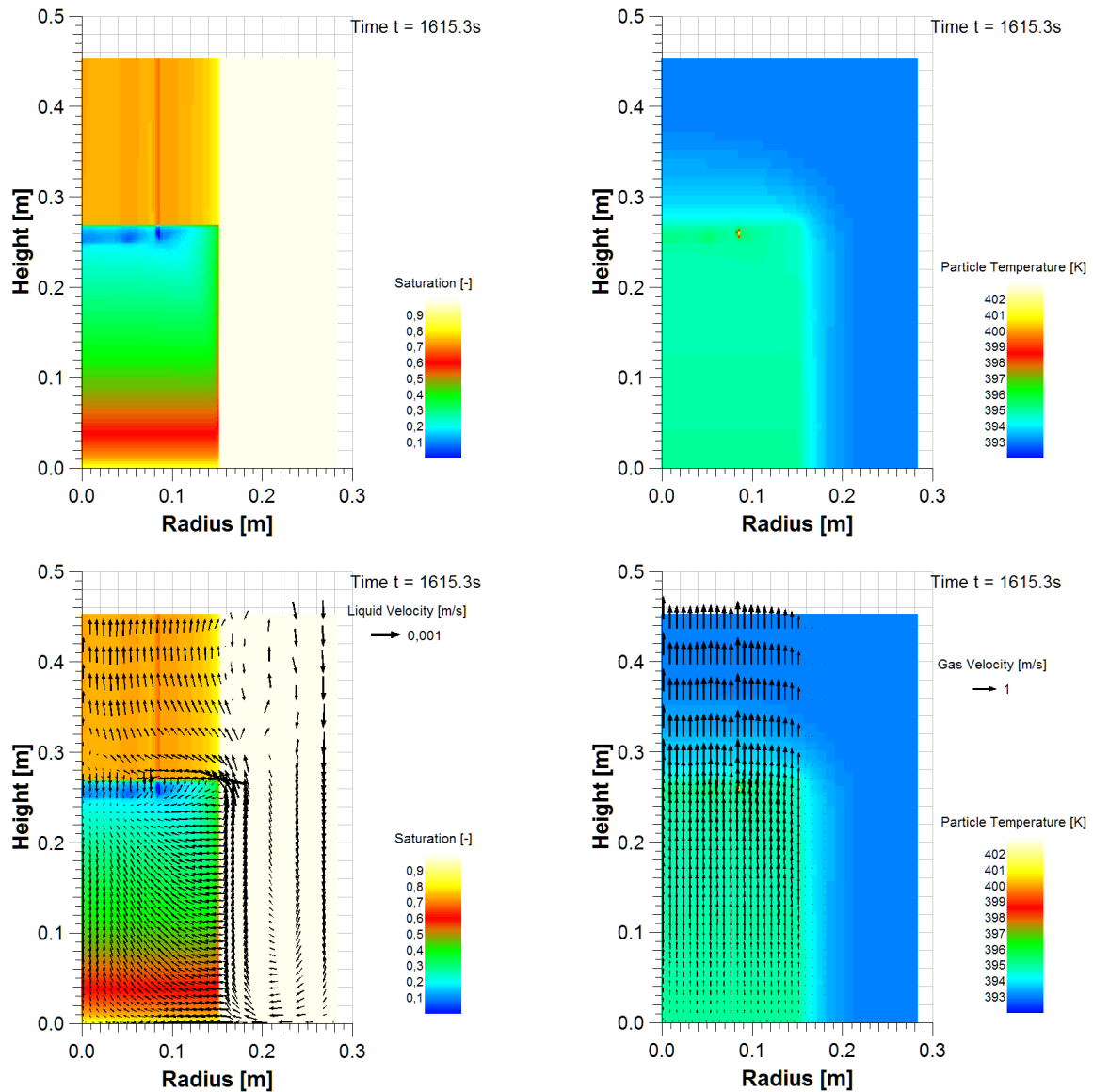


Fig. 3. Distributions of saturation (left) and particle temperature (right) in the COOLOCE-10 simulations using the Reed drag force model, 2 bar pressure. The vectors of liquid and gas pore velocity (physical velocity) are imposed on the bottom graphs.

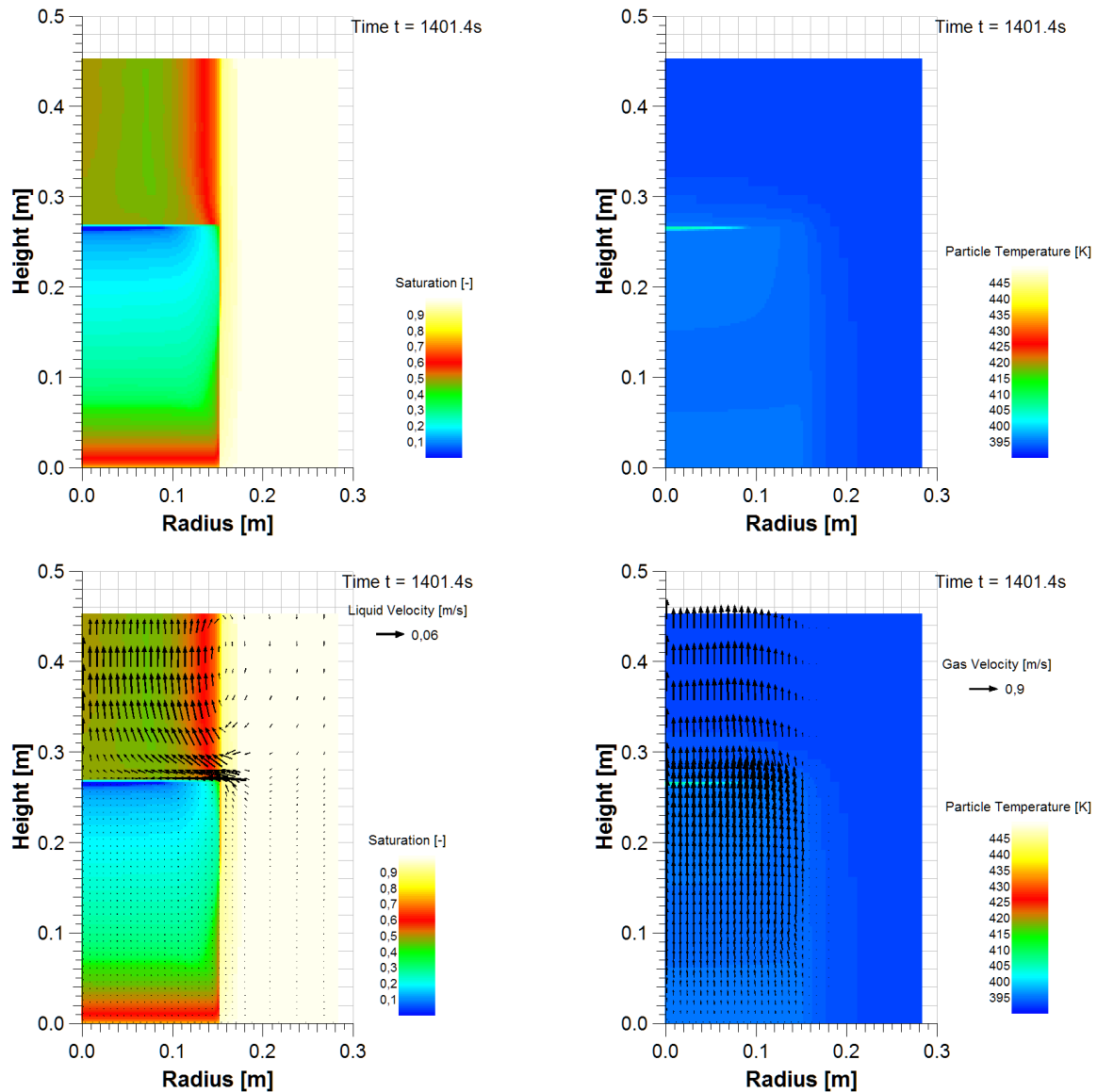


Fig. 4. Distributions of saturation (left) and particle temperature (right) in the COOLOCE-10 simulations using the Tung & Dhir drag force mode, 2 bar pressure. The vectors of liquid and gas pore velocity (physical velocity) are imposed on the bottom graphs.

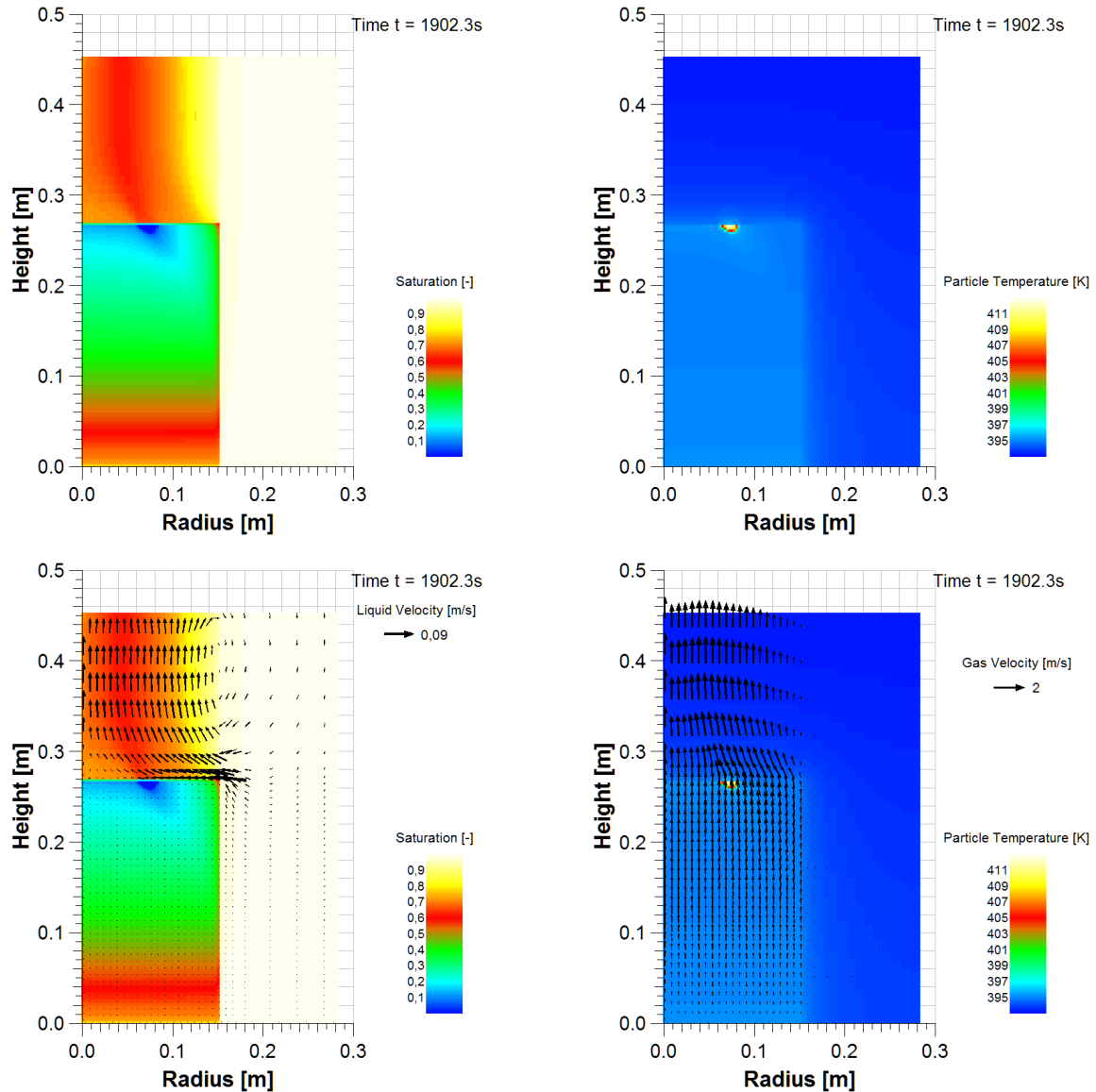


Fig. 5. Distributions of saturation (left) and particle temperature (right) in the COOLOCE-10 simulations using the modified Tung & Dhir drag force model, 2 bar pressure. The vectors of liquid and gas pore velocity (physical velocity) are imposed on the bottom graphs.

In all the cases, dryout starts in a small region in the upper part of the geometry. When heating power is further increased, the system stabilizes into a new steady-state in which the volume of the dryout zone is increased as a result of the increased steam production. According to the present simulations, the heat transfer from the solid particles to the gas phase is capable of significantly limiting the temperature increase. Thus, it is not well-established to consider the formation of the first dryout region as the limit of coolability.

The evolution of the maximum solid temperature of the simulation with the TD model is shown in Fig. 6. The heating power is increased by 1 kW every 500 s. At the dryout power of 46 kW (2330 kW/m<sup>3</sup>), the maximum temperature stabilizes at 407 K which is just 14 K above the saturation temperature. In the post-dryout conditions at 49 kW (2480 kW/m<sup>3</sup>), the temperature is 447 K which is still very low compared to the corium melting temperatures: about 3100 K for uranium oxide.

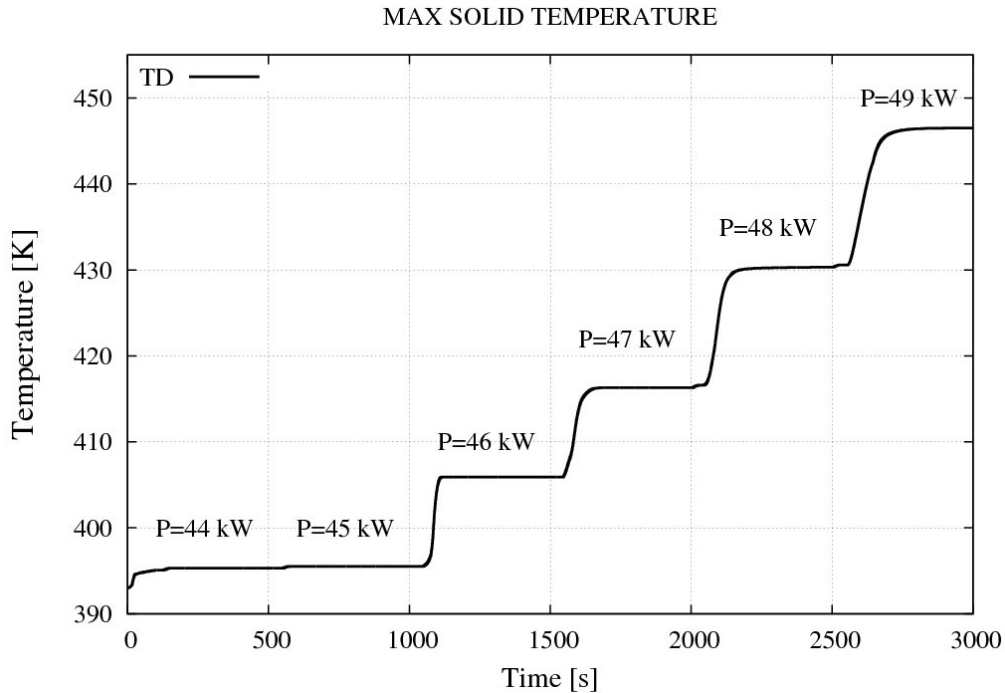


Fig. 6. Maximum solid temperature in the COOLOCE-10 simulation calculated with the Tung & Dhir model.

## 4.2 Laterally flooded cylinder (COOLOCE-11)

The cylinder of COOLOCE-11 is a special case because flooding is allowed only through the sidewall. The top plate on the debris bed (shown in Fig. 1(d)) acts as a simulant for agglomerated particles that form an impermeable layer on top of the particulate debris (cake). Due to the complexity of the debris bed formation process, it is not known which kind of cake or agglomerate formation would be most probable. A cake that covers the full surface of the bed is an extremity and, as such, not considered very likely. However, the bed is of interest as a code validation case due to the flooding mode not addressed before, and due to the very conservative assumption of the fully blocked top surface. Except for the impermeable top, the set-up is the same as in COOLOCE-10 (the same test bed was used in the two experiments).

In this case, the simulation results were somewhat contradictory to the experimental ones. In the experiments, the coolability was relatively good with the dryout power being greater than in the reference case of the top flooded cylinder by 10-40 % (1-7 bar), i.e. the lateral flooding only is more effective than pure top flooding. This was not seen in the simulations. Instead, the steam is accumulated below the impermeable top and the direction of flow is mainly vertical with little influence from the pool region to the porous region as shown in Fig. 7 which presents the saturation and particle temperature distributions in the 1.1 bar simulation. The power level in the figure, 21.9 kW, corresponds to the experimentally measured power.

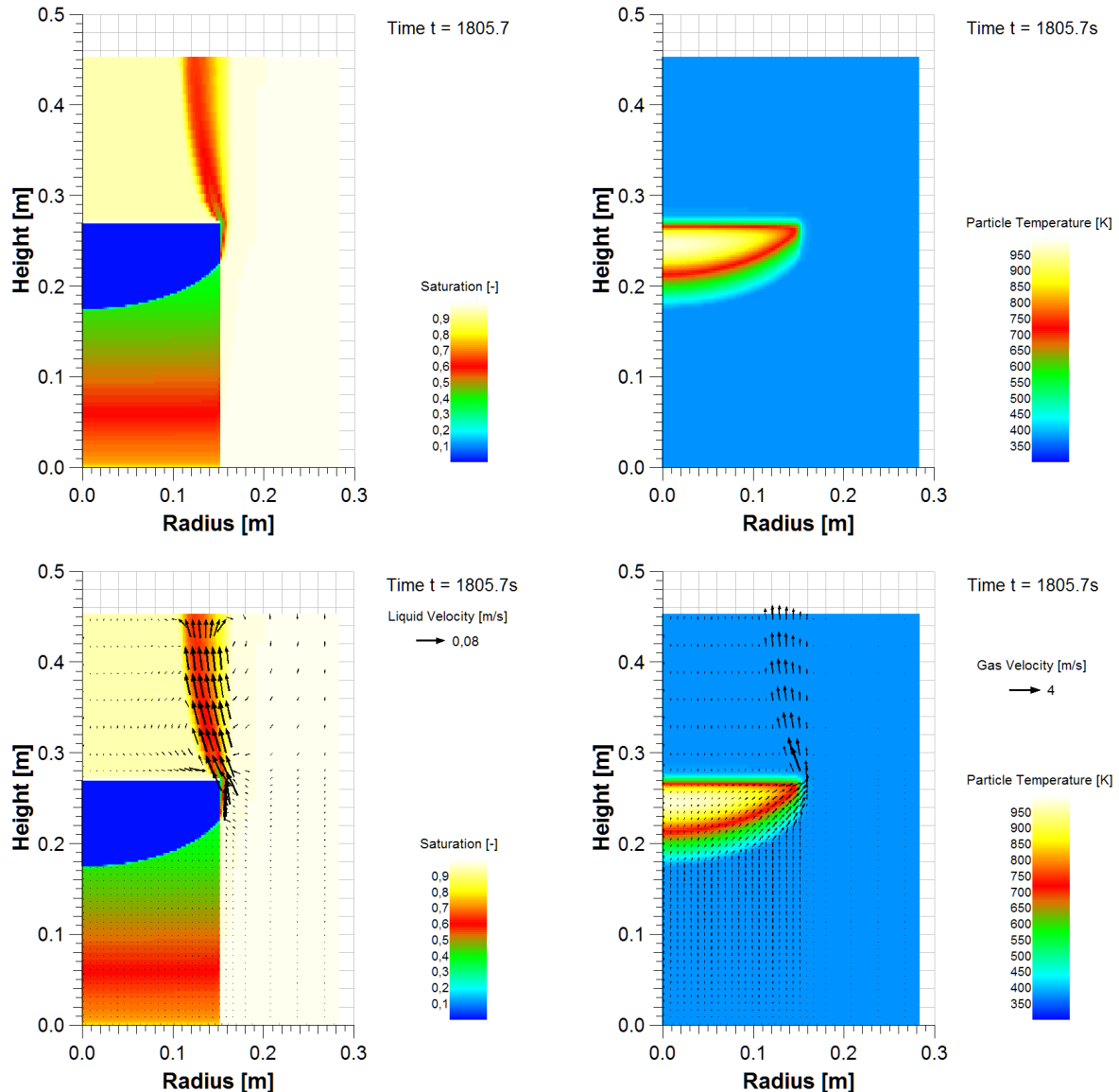


Fig. 7. Distributions of saturation (left) and particle temperature (right) in the COOLOCE-11 simulations using the modified Tung & Dhir drag force model, 1.1 bar pressure. The vectors of liquid and gas pore velocity (physical velocity) are imposed on the bottom graphs.

Without effective lateral flow, only a small power (1 kW) is required to accumulate the steam flow into a local dryout zone in the form of a thin, large bubble below the top plate. In the experiments, the TCs and heaters do not reach the top plate, the highest measurement points are at 225 mm, which means that the presence of a stable thin dryout zone cannot be excluded nor verified. If such a thin layer existed in the experiments, however, it had to be at least somewhat stable because otherwise dryout would have spread to the sensor locations earlier within the time frame of the experiment (the test bed was heated with 10kW power or more about 2-3 hours in six measurements).

It is important to note that the simulation does not reach steady-state; the temperature continues to increase at the average rate of 20°C/min until the end of the simulation at 2400s (40 min) at which point the temperature is about 1100 K. Because of this transient, the coolability potential suggested by the simulations is reduced compared to e.g. the conical bed and the fully flooded cylinder. This result appears to be overly conservative when compared to the experimental results. It is possible that the drag forces in the radial direction, in which the flow is not dominated by gravity and buoyancy, are not accurately enough captured with the available models.

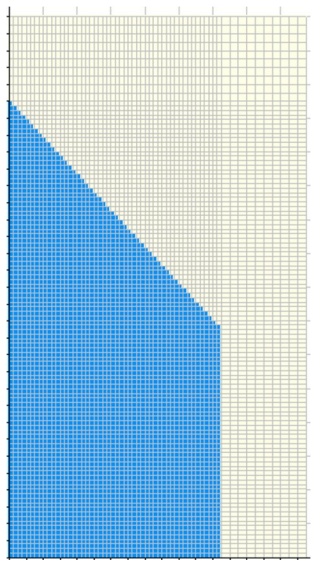
A parameter variation which accounted for the unheated particle layer in the experiments between the top plate and the tops of the heaters (40 mm thickness) was conducted. This had no effect on the formation of the large steam “bubble” below the top plate, and the dryout zone was even larger than in the homogeneously heated case.

The post-dryout temperature increase has not been studied experimentally because this would cause damage to the heaters and thermocouples due to overheating. The temperature increase observed during the (arbitrary) time interval between dryout and the power shutdown varies from slow, few centigrade increases to sharp increases of 20-30°C (Takasuo et al. 2013b).

### 4.3 Cone on a cylindrical base (COOLOCE-12)

The cone on a cylindrical base geometry addressed in COOLOCE-12 is a combination of the conical and cylindrical geometries. In a reactor scenario, the mass and volume of the corium allow the debris bed to spread partially against the walls of the containment, while it is possible that the top parts maintain the heap-like shape. The MEWA simulation set-up for this case is presented in Table 2. The comparison of the experimental and simulated dryout power for the different pressure levels is shown in Fig. 8. The pressure variations have been modelled by using the modified Tung & Dhir model because this model has been found to yield good results for the fully conical bed in previous studies (Rahman, 2013, Takasuo et al. 2012c).

Table 2. Simulation set-up for C-12.

Particle diameter	0.97 mm	
Porosity	0.38	
Material density	4200 kg/m <sup>3</sup>	
Thermal conductivity	2.0 W/mK	
Specific heat capacity	775 J/kgK	
Grid cell size	2.5 mm x 2.7 mm	
Time step size	Controlled by the code, 1.0e-6 – 2.0s	
Heating method	Homogenous (constant power density)	
Pressure	Experimental, 1.09-3.81 bar	
Boundary conditions (top)	Pressure, saturated liquid inflow	
Boundary conditions (side and bottom)	Adiabatic, no flow-through	



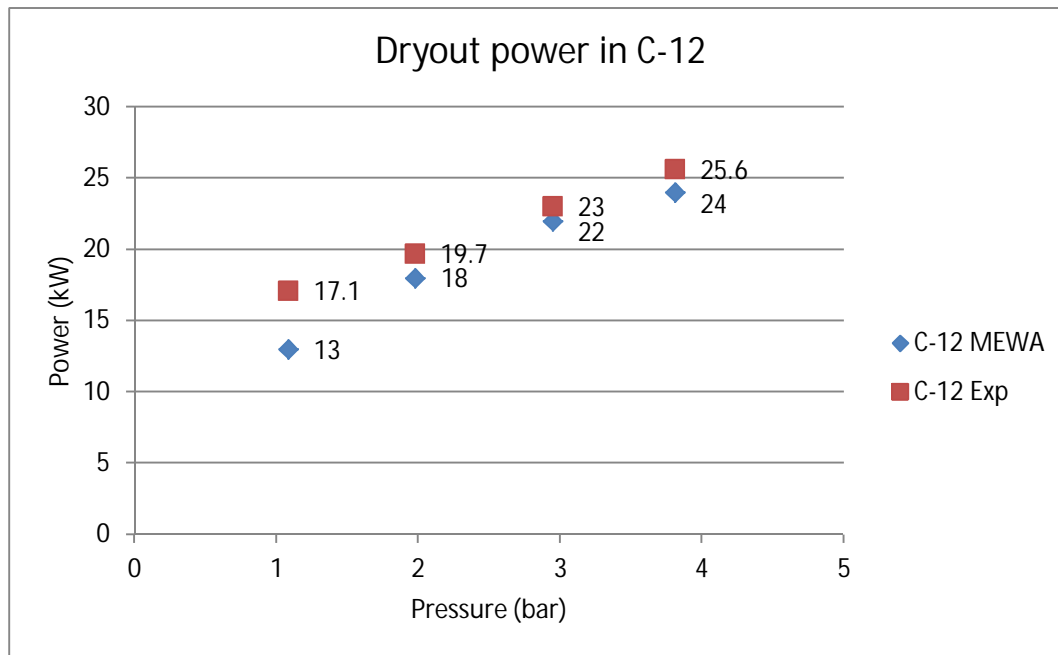


Fig. 8. Experimental and simulated dryout power in C-12 (cone on a cylindrical base) predicted with the modified Tung & Dhir model.

It is seen in Fig. 8 that the experimental and simulated powers are in a relatively good agreement. The greatest deviation is found at 1.1 bar. However, in the experiments, it was somewhat unclear whether the actual dryout occurred at 17.1 kW or at about 15 kW at which power the heater temperatures were already clearly increased, indicating conditions very close to the dryout limit. This ambiguity in the interpretation of the experimental results partially explains the difference at 1.1 bar.

The saturation and solid temperature distributions at 2.0 bar in dryout conditions (18 kW) are illustrated in Fig. 9. Dryout is formed in the tip of the conical part similarly to the fully conical geometry. The dryout location is not model-dependent as observed in the C-10 simulations. The dryout power density or the calculated DHF (DHF = power density  $\times$  height) at the tip of the geometry is very close to the one in the fully conical geometry (discussed in Takasuo et al. 2013c). Apparently, this is explained by (1) the similar height of the geometry in the centre which means similar accumulation of steam mass flux at the top boundary and (2) the impermeable cylindrical part being low enough not to significantly hinder the water flow downwards (counter-current flow limitation is not met).

In fact, the radial distance in the bottom of the *fully conical bed* is almost the same as the distance that the liquid travels by first flowing down near the boundary of the cylindrical part and the towards the centre in the *cone on a cylindrical base*. According to the results, the water infiltration laterally through the lower, bottommost regions of the fully conical bed is not more effective than the circulation that provides water in the cone on a base case in cooling the central top region (which is most vulnerable to dryout). It should be noted that the result is not to be generalized to all possible cases with different conical and cylindrical part dimensions. The dryout power is strongly dependent on the total height of the geometry – the flatter the better – and if the cylindrical part height is increased, the counter-current flow must become dominant at some point.



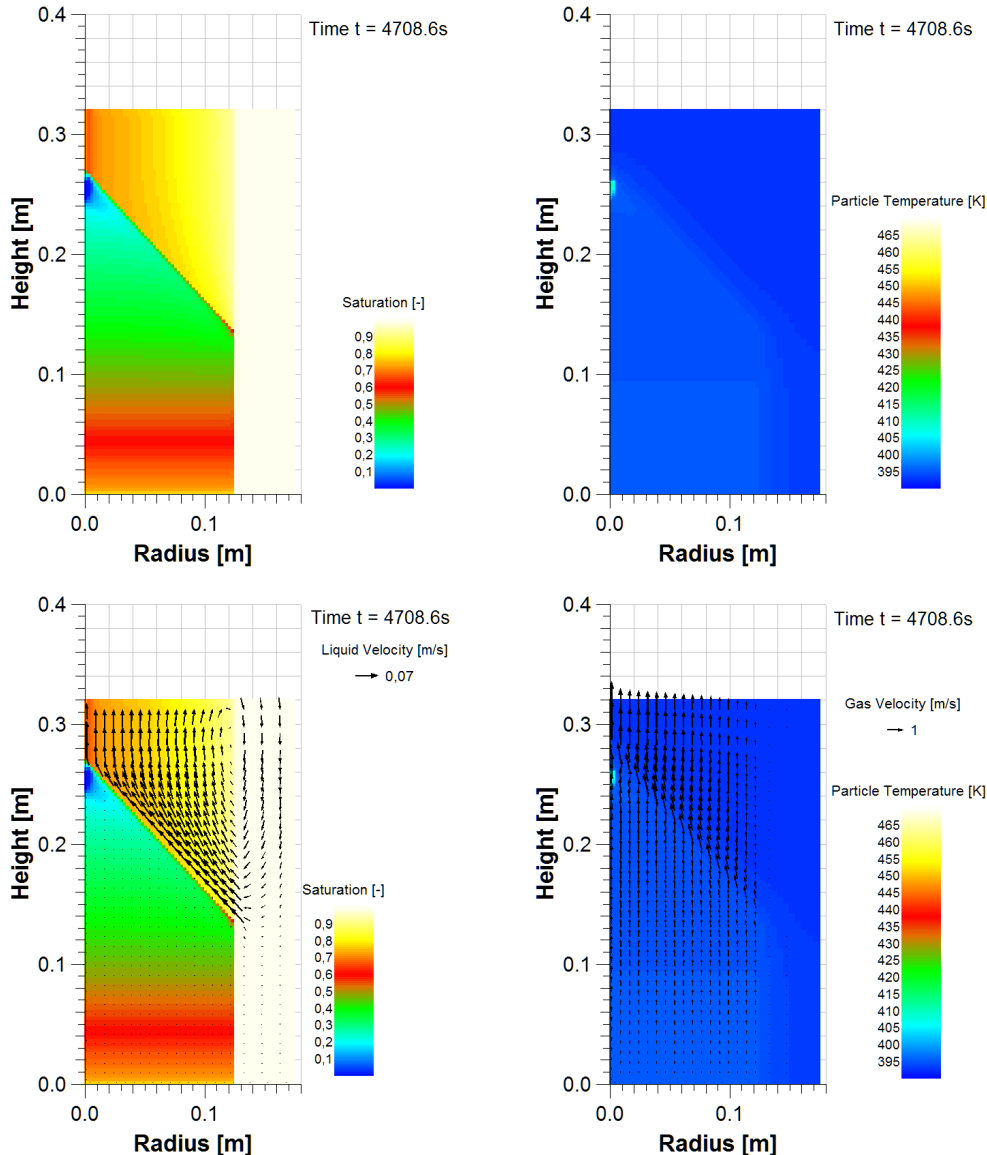


Fig. 9. Distributions of saturation (left) and particle temperature (right) in the COOLOCE-12 simulations using the modified Tung & Dhir drag force model, 2 bar pressure. The vectors of liquid and gas pore velocity (physical velocity) are imposed on the bottom graphs.

#### 4.4 Summary

In a broad sense, the simulations models are capable of predicting the dryout power and the relative coolability of the fully flooded cylinder (C-10) and the cone on a cylindrical base (C-12) with suitable model selections. However, in the case of C-10 the dependency of the simulation results on the drag force model is stronger than in the other geometries. In addition to the dryout power, the location of the incipient dryout and the flow field are somewhat different depending on which drag force model is applied.

The modified Tung & Dhir model has been previously validated against the fully conical geometry and combinations of top and bottom flooding configurations (Rahman, 2013) which

would make this model the logical choice for the fully flooded cylinder. The Reed model with no interfacial drag generally tends to underestimate coolability (greater void fractions with lower heating power). However, in this case, the best apparent result was obtained by the Reed model instead of the MTD model.

In the case of the laterally flooded cylinder (C-11), the simulations yield overly conservative results compared to the experiments. According to the simulations, the lateral flow from the pool into the porous zone is not very effective in maintaining the coolability, independently of the drag force model. Experimentally, the coolability of this case was rather good, better than in pure top-flooding, but this was not reproduced in the simulations.

A possible explanation to the simulation results of C-10 and C-11 is that the interfacial drag is not realistically captured when the flow direction is mainly lateral and/or the lateral flow is allowed to freely mix with top flooding. The semi-empirical drag force models have been developed based on experiments which examined top and bottom flooding (either forced or driven by the hydrostatic pressure of water column connected to the bottom of the debris bed). In comparison, the two COOLOCE geometry variations with free lateral surfaces are more challenging to model accurately.

The dryout behaviour of the cone on a cylindrical base (C-12) was very similar to that of the fully conical bed: both the dryout power density and the dryout location were similar. The partially closed geometry did not impair coolability compared to a cone of the same height. This was also rather well predicted by the simulation with the modified Tung & Dhir drag force model.

## 5. CFD simulations

---

The CFD simulations were performed with the commercial FLUENT CFD package by Ansys Inc. Compared to the MEWA simulations, the approach with FLUENT is more “typical” to CFD simulations. We have investigated the underlying mechanisms that affect the dryout formation by examining the saturation distributions, temperatures and velocities in the debris bed and the surrounding water pool in detail. This improves the general understanding of the flow phenomena in the debris bed-pool system and, thus, the formation of dryout in a manner that would be difficult to achieve only by power comparisons using strongly simplified porous media models. In addition, the observed differences between the experiments and the simulations can be elucidated.

On the other hand, it would be rather tedious to conduct lengthy CFD simulations of all the COOLOCE experiments including pressure variations, or to perform parameter variations to obtain a DHF distribution as a function of e.g. porosity. It is reasonable to limit the study to certain key geometries with representative bed parameters and, in the future, to cases with geometrical irregularities not scalable to 2D.

### 5.1 Physical models and implementation

#### 5.1.1 Conservation equations

There are two commonly applied CFD formulations to describe fluid flows in a porous medium, the physical (pore, interstitial) velocity formulation and the superficial velocity formulation. Both approaches are available in Fluent (2011b). The conservation equations based on the physical velocity formulation are computationally more difficult to solve, if the porosity varies significantly or the medium is hydrodynamically anisotropic.

##### 5.1.1.1 Physical velocity formulation

In the physical velocity formulation, the velocity in the balance equations is representing the actual velocity in the pores of the porous medium. Since in the porous medium approximation all quantities are representing average values over a representative elementary volume, the physical velocity is thus an average of the velocity in pores.

In multiphase CFD codes, the physical velocity based balance equations for porous media are similar to Eqs. (1) – (3) (Fluent 2011b). Computationally obtained results are reliable as long as the porous medium is homogenous and the flow is largely controlled by the friction forces. Applicability of Eqs. (1) – (3) is not obvious, when the porosity varies. In principle, specific interface models are needed for porosity steps. In practical applications, the influences of the porosity steps are, however, usually ignored. Furthermore, conservation equations similar to Eqs. (1) – (3) can and are used for free-flow zones ( $\varepsilon = 1$ ). In these applications, several terms are ignored in the derivation (i.e. the pressure fluctuation term) and some of them might be important.

One term missing in the momentum equation (Eq.(2)) is the momentum exchange between the phases due to the mass exchange term  $\Gamma$  in the continuity equation, Eq. (1). This term was implemented in the CFD simulations as follows

$$\overrightarrow{F_{r,g}} = -\overrightarrow{F_{r,l}} = \max(\Gamma, 0) \vec{v}_l - \max(-\Gamma, 0) \vec{v}_g \quad (21)$$

The momentum exchange resulting from the mass exchange is small in particle beds. The term might have some importance in the free-flow pool outside the bed. As noted in Section 3.1, the MEWA formulation for the momentum equation ignores the shear stress term  $\nabla \cdot (\varepsilon \alpha_i \vec{\tau}_i)$ . For isotropic and incompressible Newtonian fluids (i.e. for most common fluids), the shear stress can be calculated from

$$\vec{\tau}_i = \mu_i (\nabla \vec{v}_i + (\nabla \vec{v}_i)^T) \quad (22)$$

In CFD models, the frictional force  $\overrightarrow{F_{s,i}}$  (Eq. (2)) is commonly expressed as follows (Fluent 2011b)

$$\overrightarrow{F_{s,i}} = -\varepsilon^2 \alpha_i \mu_i D_i \vec{v}_i - \frac{1}{2} \varepsilon^3 \alpha_i \rho_i C_{2,i} |\vec{v}_i| \vec{v}_i \quad (23)$$

In the Fluent, the coefficients  $D_i$  and  $C_{2,i}$  are determined to obtain the same frictional forces  $\overrightarrow{F_{s,l}}$  and  $\overrightarrow{F_{s,g}}$  as in the MEWA code (Eqs. (5) and (6)). For all zones modelled as porous regions, the same models for the interfacial drag term  $\vec{F}_i$  were used as in the MEWA simulations. For open free-flow zones, the model of Schiller and Neumann (1935) was employed in order to obtain a correct slip velocity.

Considering the heat transfer, the MEWA code for the source terms in Eqs. (3) and (4) for the effective thermal conductivities was analyzed and followed closely in the Fluent implementation. The solid temperature is calculated utilizing a user-defined scalar transport equation.

#### 5.1.1.2 Superficial velocity formulation

In the superficial velocity formulation of the conservation equations, the velocity  $v$  in the conservation equations is replaced by the superficial (Darcy) velocity  $j$  defined as

$$j = \frac{Q}{A} \quad (24)$$

where  $Q$  is volume flow rate through the surface with the area  $A$ . Solving of the balance equations is easier as the superficial velocity does not change with the porosity. On the other hand, the acceleration and deceleration of the fluid at porosity steps and the corresponding pressure decreases and increases are ignored. As numerically significantly more stable, most of the porous media simulations are performed based on the superficial velocity approach. In a highly resistive porous medium, the convection and viscous terms (no turbulence) can be ignored and the momentum equation simplifies further and the pressure can be computed directly from a potential-flow formulation.

For multiphase flows, Fluent applies somewhat differently defined superficial velocity

$$j_{i,Fl} = \frac{Q_i}{\alpha_i A} \quad (25)$$

The conservation equations can thus be written as follows

$$\frac{\partial}{\partial t}(\alpha_i \rho_i) + \nabla \cdot (\alpha_i \rho_i \vec{j}_{i,Fl}) = \Gamma \quad (26)$$

$$\begin{aligned} \frac{\partial}{\partial t}(\alpha_i \rho_i \vec{j}_{i,Fl}) + \nabla \cdot (\alpha_i \rho_i \vec{j}_{i,Fl} \vec{j}_{i,Fl}) \\ = -\alpha_i \nabla p_i + \alpha_i \rho_i \vec{g} + \nabla \cdot (\alpha_i \vec{\tau}_i) + \frac{\vec{F}_{s,i}}{\varepsilon} + \frac{\vec{F}_i}{\varepsilon} + \frac{\vec{F}_{\Gamma,i}}{\varepsilon} \end{aligned} \quad (27)$$

$$\frac{\partial}{\partial t}(\alpha_i \rho_i h_i) + \nabla \cdot (\alpha_i \rho_i \vec{j}_{i,Fl} h_i) = \nabla \cdot (\lambda_{eff,i} \nabla T_i) + Q_{s,i} + Q_{evap,i} \quad (28)$$

The friction force terms are thus

$$\frac{\vec{F}_{s,i}}{\varepsilon} = -\alpha_i \mu_i D_i \vec{j}_{i,Fl} - \frac{1}{2} \alpha_i \rho_i C_{2,i} |\vec{j}_{i,Fl}| \vec{j}_{i,Fl} \quad (29)$$

The coefficients  $D_i$  and  $C_{2,i}$  are determined as in the physical velocity formulation. The pore velocity was used when calculating the interfacial drag force. The heat transfer models are the same as in the physical velocity formulation.

### 5.1.2 Turbulence modelling

Eqs. (1.) – (3) and (26) – (28) are commonly applied to turbulent multiphase flows in porous media and free-flow zones by adding an extra shear term  $\nabla \cdot (\varepsilon \alpha_i \vec{\tau}_{T,i})$  in the momentum equations. The calculation of the turbulent stress  $\vec{\tau}_{T,i}$  is commonly based on turbulence models. In Fluent

$$\vec{\tau}_{T,i} = \mu_{T,i} (\nabla \vec{v}_i + (\nabla \vec{v}_i)^T) - \frac{2}{3} (\rho_i k_i + \mu_{T,i} \nabla \cdot \vec{v}_i) \mathbf{I} \quad (30)$$

where  $\mu_{T,i}$  is the turbulent viscosity,  $k_i$  the turbulent kinetic energy and  $\mathbf{I}$  the identity tensor. The turbulent viscosity  $\mu_{T,i}$  and turbulent kinetic energy  $k_i$  are provided by the turbulence model.

In this study, two alternative multiphase turbulence models, k- $\varepsilon$  mixture turbulence model and k- $\varepsilon$  dispersed turbulence model, were used. For porous media, these models would need some modifications, but, for instance, the Fluent models do not have any corrections for porous media application. On the other hand, in highly resistive porous media like beds with small particles, under weak forces flow is largely laminar. Therefore, in this study flows in the porous zones were assumed laminar and turbulence was modelled only in free-flow zones, i.e. in the pool outside the beds.

#### 5.1.2.1 k- $\varepsilon$ mixture turbulence model

In the k- $\varepsilon$  mixture turbulence model, the turbulence kinetic energy and turbulence dissipation rate are solved for the mixture of the phases.

$$\frac{\partial(\rho_m k)}{\partial t} + \nabla \cdot (\rho_m \vec{v}_m k) = \nabla \cdot \left[ \frac{\mu_{T,m}}{\sigma_k} \nabla k \right] + G_k - \rho_m \epsilon \quad (31)$$

$$\frac{\partial(\rho_m \epsilon)}{\partial t} + \nabla \cdot (\rho_m \vec{v}_m \epsilon) = \nabla \cdot \left[ \frac{\mu_{T,m}}{\sigma_\epsilon} \nabla \epsilon \right] + \frac{\epsilon}{k} (C_{1\epsilon} G_k - C_{2\epsilon} \rho_m \epsilon) \quad (32)$$

where  $\epsilon$  is the turbulent dissipation rate,  $C_1$  and  $C_2$  are model constants and  $\rho_m$  and  $\vec{v}_m$  the mixture density and velocity. In our cases

$$\rho_m = \alpha_l \rho_l + \alpha_g \rho_g \quad (33)$$

$$\vec{v}_m = \frac{\alpha_l \rho_l \vec{v}_l + \alpha_g \rho_g \vec{v}_g}{\rho_m} \quad (34)$$

The mixture turbulent viscosity is calculated from

$$\mu_{T,m} = C_\mu \rho_m \frac{k^2}{\epsilon} \quad (35)$$

where  $C_\mu=0.09$ . The production term  $G_k$  is computed from

$$G_k = \mu_{T,m} (\nabla \vec{v}_m + (\nabla \vec{v}_m)^T) : \nabla \vec{v}_m \quad (36)$$

The k- $\epsilon$  mixture turbulence model is applicable when flow is stratified, the density ratio is close to 1 or phases separate (Fluent 2011a).

#### 5.1.2.2 k- $\epsilon$ dispersed turbulence model

In the Fluent computations, the k- $\epsilon$  dispersed turbulence model can also be used to model turbulence. For the primary phase  $q$ , the turbulence quantities are computed from modified k- $\epsilon$  transport equations (Fluent 2011a)

$$\begin{aligned} \frac{\partial(\alpha_q \rho_q k_q)}{\partial t} + \nabla \cdot (\alpha_q \rho_q \vec{v}_q k_q) \\ = \nabla \cdot \left[ \alpha_q \frac{\mu_{T,q}}{\sigma_k} \nabla k_q \right] + \alpha_q G_q - \alpha_q \rho_q \epsilon_q + \alpha_q \rho_q \Pi_{k,q} \end{aligned} \quad (37)$$

$$\begin{aligned} \frac{\partial(\alpha_q \rho_q \epsilon_q)}{\partial t} + \nabla \cdot (\alpha_q \rho_q \vec{v}_q \epsilon_q) \\ = \nabla \cdot \left[ \alpha_q \frac{\mu_{T,q}}{\sigma_\epsilon} \nabla \epsilon_q \right] + \alpha_q \frac{\epsilon_q}{k_q} (C_{1\epsilon} G_q - C_{2\epsilon} \rho_q \epsilon_q) + \alpha_q \rho_q \Pi_{\epsilon,q} \end{aligned} \quad (38)$$

where the source terms  $\Pi_{k,q}$  and  $\Pi_{\epsilon,q}$  represent the influence of the secondary phase on the primary phase. The Fluent closure models for the additional source terms  $\Pi_{k,q}$  and  $\Pi_{\epsilon,q}$  are relatively simple algebraic expressions but as several new parameters should be introduced, the formulation is omitted here. The formulation is given in the Fluent theory guide (Fluent 2011a). Turbulence in the secondary phase is calculated from an algebraic expression using the values of the turbulence quantities of the primary phase. The k- $\epsilon$  dispersed turbulence model is most applicable when the primary phase is clearly continuous and the secondary phase is dilute.

### 5.1.3 Verification of the CFD implementation

The Fluent implementation was verified by simulating a 1D particle bed in 3D. Physical conditions and material properties used in the test simulations are listed in Table 3. The height of the bed is 60 cm and it measures horizontally 2 cm x 2 cm. All cells are hexahedrons of size 2 cm x 2 cm x 2 cm.

Fig. 10 presents analytically obtained correlations between the heating power and the minimum liquid saturation for the Reed and MTD friction models. The correlations are calculated from simplified force balances (Eqs.(1) - (2)) without time dependent, convection and stress terms. The curves in Fig. 10 give the minimum liquid saturation close to the surface as a function of the heat flux. The minimum liquid saturation decreases as the heat flux increases. The DHF is the maximum heat flux value on a curve and determines the corresponding minimum liquid saturation. The curve is not applicable for liquid saturation values which are smaller than the one for the DHF (or, in other words, for heat fluxes greater than the DHF). The details of the analytical solution method will be described in 6.2.1.

Fig. 11 summaries comparison results for a heat flux of 150 kW/m<sup>2</sup>. The agreement is excellent expect for the liquid superficial velocity. The CFD results differ from the analytical and MEWA results in the lowest and uppermost cells. This is related to the well-known problem of the pressure gradient calculation and mainly to the selection of the pressure value on the wall boundaries. MEWA is equipped with special upper and lower boundary conditions. Similar boundary conditions could also be implemented in general-purpose CFD codes but they might not be applicable in different geometrical conditions. Although the cell centre values of the liquid superficial velocity in Fig. 11 are wiggling, the face values used when solving the balance equations behave smoother. Fig. 12 shows vertical profiles of the liquid saturation for a Fluent simulation with a heat flux of 280 kW/m<sup>2</sup>. The simulation agrees with Fig. 10.

*Table 3. Physical conditions and material properties in the CFD modelling of the 1D test case.*

Quantity (symbol)	Value (unit)
Pressure ( $p$ )	1.0 bar
Bed particle diameter ( $d$ )	1.0 mm
Bed porosity ( $\varepsilon$ )	0.40
Bed material density ( $\rho_s$ )	4200 kg/m <sup>3</sup>
Liquid density ( $\rho_l$ )	958.5kg/m <sup>3</sup>
Gas density ( $\rho_g$ )	0.59 kg/m <sup>3</sup>
Dynamic viscosity for liquid ( $\mu_l$ )	0.0002829 kg/sm
Dynamic viscosity for gas ( $\mu_g$ )	0.0000121 kg/sm
Specific heat capacity for bed ( $c_{p,s}$ )	775 J/kgK
Specific heat capacity for liquid ( $c_{p,l}$ )	4216 J/kgK
Specific heat capacity for gas ( $c_{p,g}$ )	2024 J/kgK
Thermal conductivity for bed ( $\lambda_s$ )	2.0 W/Km
Thermal conductivity for liquid ( $\lambda_l$ )	0.681 W/Km
Thermal conductivity for gas ( $\lambda_g$ )	0.02466 W/Km

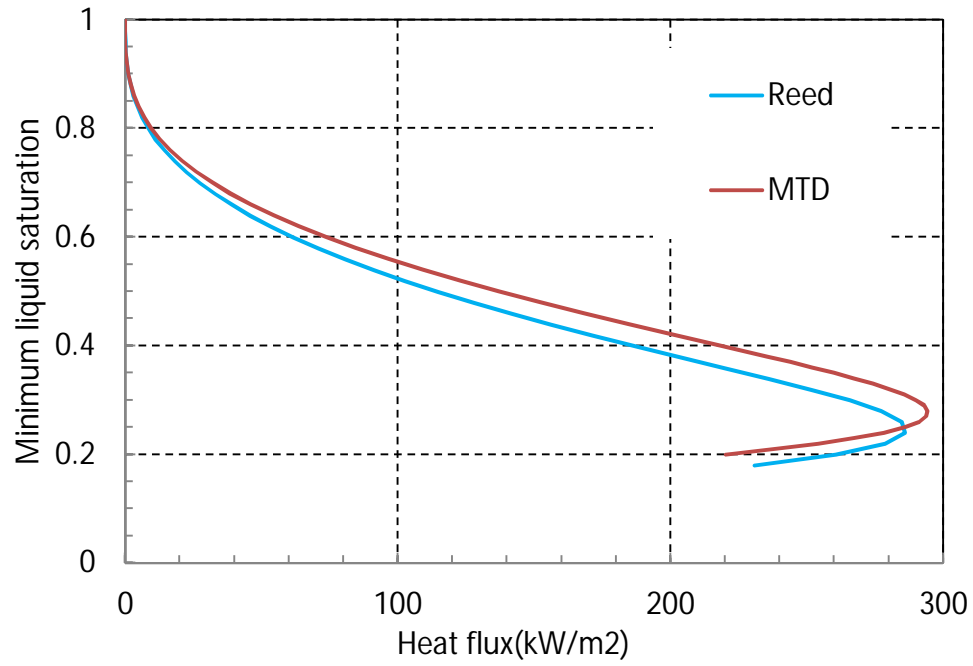


Fig. 10. Analytical correlation of the heat flux and the minimum liquid saturation for the Reed and MTD friction models in a 1D heated bed. The maximum heat flux defines the DHF and a corresponding minimum liquid saturation.



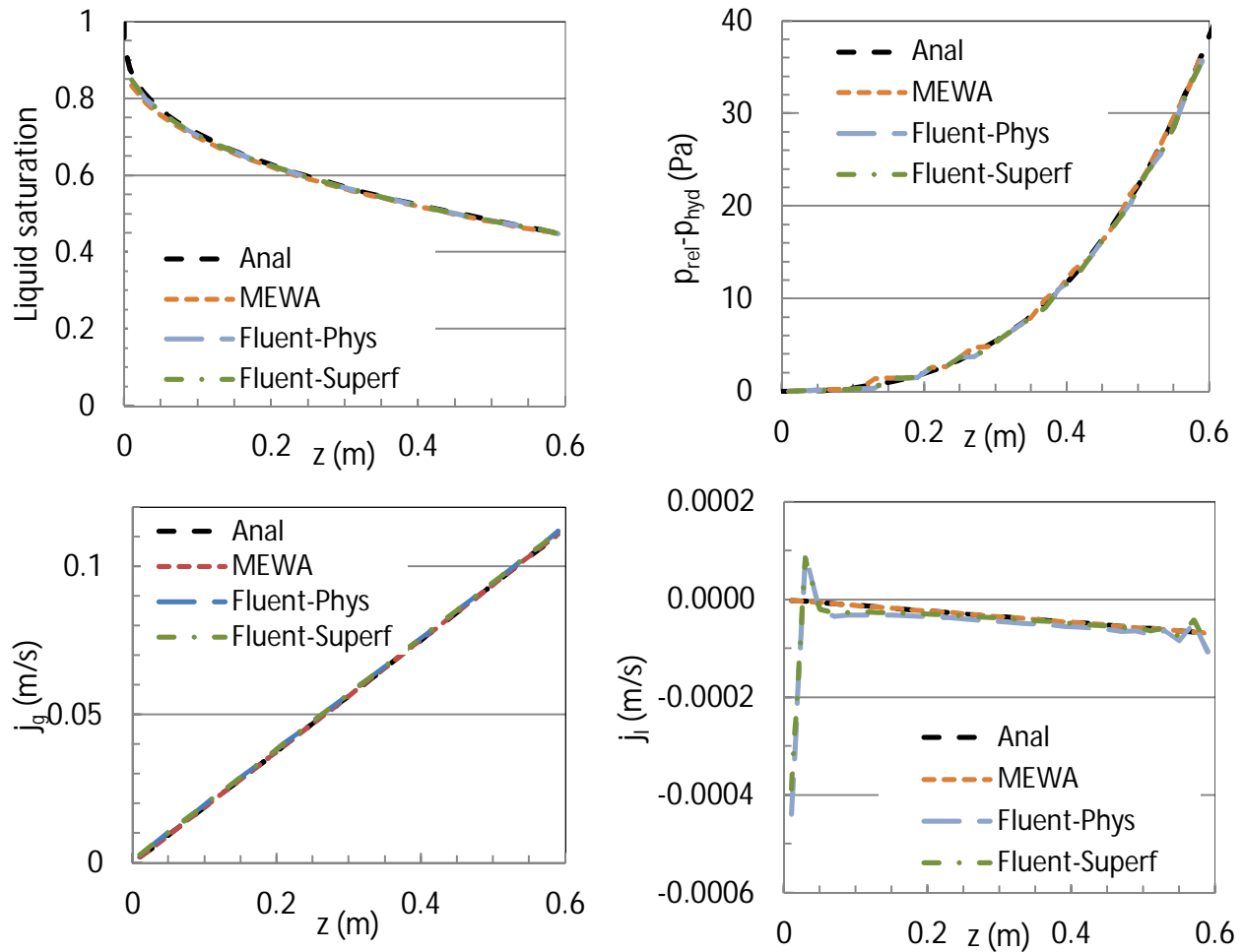


Fig. 11. Comparison of the Fluent simulation results to the analytical and MEWA simulation results for a 60 cm porous bed with a heating power of 150 kW/m<sup>2</sup>. Top left: liquid saturation, top right: relative pressure without the hydrostatic pressure, bottom left: superficial gas velocity, bottom right: superficial liquid velocity (Phys – physical velocity formulation, Superf – superficial velocity formulation). The Reed friction model assumed and  $p = 1$  bar.

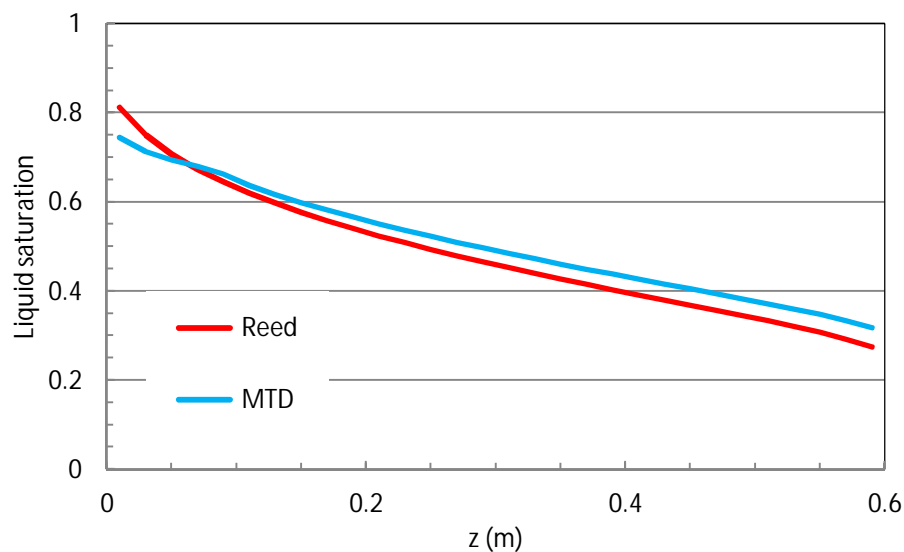


Fig. 12. Vertical profiles of the liquid saturation in the CFD simulations of a 60 cm porous bed with a heating power of 280 kW/m<sup>2</sup>.

## 5.2 Results

Next, the results of the CFD simulations for all geometry variations, excluding the cone on a cylindrical base, are presented and comparisons to the MEWA results are made. Different types of modelling options and mesh sensitivity have been tested for the fully conical bed. This is considered to be a key geometry because the pouring of granular material on a horizontal surface typically forms a conical heap. For the fully flooded cylinder, different drag force models were tested as a consequence of the observed dependence of the MEWA results on the model selection.

### 5.2.1 Cylindrical bed

The 2D simulations for the top-flooded cylindrical bed (shown in Fig. 1 (a)) were carried out assuming axisymmetry. The computational mesh was regular with 2.5 mm x 2.5 mm cells. The physical conditions and material properties are summarised in Table 4. Analytically obtained correlations between the heating power and the minimum liquid saturation for the Reed and MTD friction models are plotted in Fig. 13. The analytical correlation assumes 1D geometry. The dryout power is about 22 kW and 23.5 kW for the Reed and MTD models, respectively.

The CFD simulations were conducted with the superficial velocity formulation of Fluent. Both the Reed and MTD models were used and the total heating power varied from 20 kW to 24 kW. Similarly to the MEWA simulations, it is assumed that the heating power is evenly distributed in the bed. Fig. 14 shows the vertical profiles of the liquid saturation for the Reed and MTD friction models with three different heating power values. The Reed model result for the 23 kW power is not a steady state solution since the bed is not coolable and dryout is gradually reached. This is the same dryout power that has been obtained with MEWA in previous simulations with the same porosity, particle size and drag force model. It is seen that dryout occurs near the bottom of the bed after a saturation transient which is the expected behaviour for a top-flooded bed.

*Table 4. Physical conditions and material properties in the CFD modelling of the cylindrical bed.*

Quantity (symbol)	Value (unit)
Pressure ( $p$ )	1.1 bar
Bed particle diameter ( $d$ )	0.97 mm
Bed porosity ( $\varepsilon$ )	0.40
Bed material density ( $\rho_s$ )	4200 kg/m <sup>3</sup>
Liquid density ( $\rho_l$ )	956.3 kg/m <sup>3</sup>
Gas density ( $\rho_g$ )	0.655 kg/m <sup>3</sup>
Dynamic viscosity for liquid ( $\mu_l$ )	0.000273 kg/sm
Dynamic viscosity for gas ( $\mu_g$ )	0.0000122 kg/sm
Specific heat capacity for bed ( $c_{p,s}$ )	775 J/kgK
Specific heat capacity for liquid ( $c_{p,l}$ )	4217 J/kgK
Specific heat capacity for gas ( $c_{p,g}$ )	2032 J/kgK
Thermal conductivity for bed ( $\lambda_s$ )	2.0 W/Km
Thermal conductivity for liquid ( $\lambda_l$ )	0.6819 W/Km
Thermal conductivity for gas ( $\lambda_g$ )	0.025 W/Km

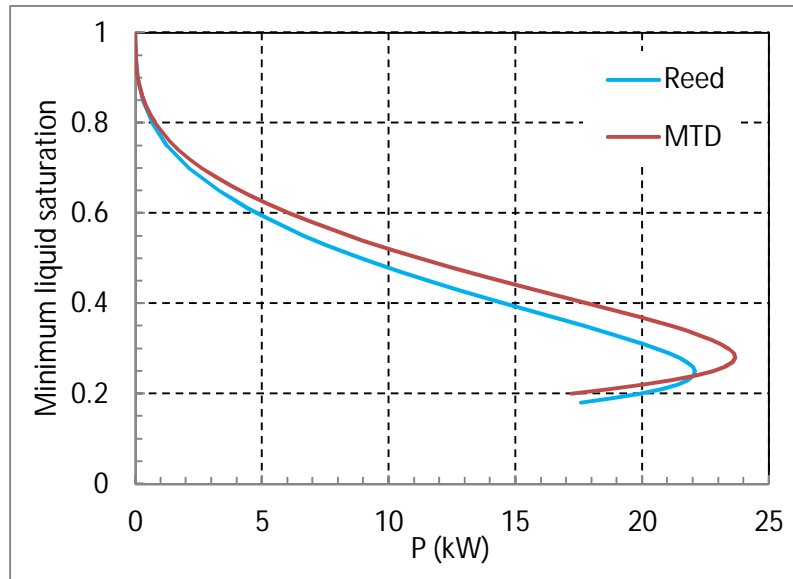


Fig. 13. Analytical correlation of the heating power and the minimum liquid saturation for the cylindrical bed.

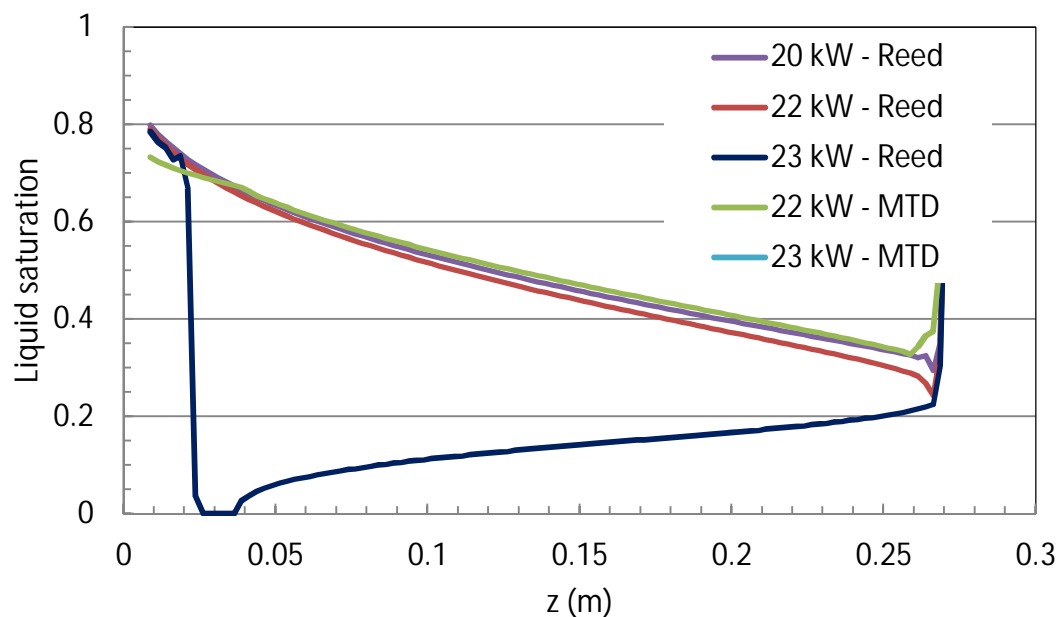


Fig. 14. Vertical profiles of the liquid saturation in the CFD simulations for the cylindrical bed (the 23 kW result for the Reed model is not in a steady state).

## 5.2.2 Conical bed

An extensive computational study was performed for the fully conical bed because this is the key geometry in the debris bed shape variations. The influence of the mesh and model parameters were studied. The physical conditions and material properties are summarised in Table 5. The pressure levels of 1.1, 2 and 3 bar which correspond to the experimental pressures were used in the simulations, and the influence of the pressure on the material properties was taken into account.

In most of the simulations, the total heating power was 26 kW. This is the coolability limit measured in the COOLOCE-6 experiment (1.1 bar). The influence of the heating power was also investigated but not to the extent that has been done with the MEWA code (stepwise increase with small power steps aiming to find out the accurate dryout power).

The superficial velocity formulation was applied. The MTD model was used in all of the simulations since this has been found to be a suitable model for the fully conical bed in previous MEWA studies, and also in the case of the cone on a cylindrical base. Two modelling alternatives we applied for the open pool outside the bed: The pool was modelled as a frictionless, free flow zone with a turbulent multiphase flow or as a porous zone with the same properties as in the MEWA simulations (porosity 0.99 and particle diameter 10 mm).

Table 5. Physical conditions and material properties in the CFD modelling of the conical bed.

Quantity (symbol)	Value			Unit
Pressure ( $p$ )	1.1	2	3	bar
Bed particle diameter ( $d$ )	0.95	0.95	0.95	mm
Bed porosity ( $\varepsilon$ )	0.39	0.39	0.39	-
Bed material density ( $\rho_s$ )	4200	4200	4200	kg/m <sup>3</sup>
Liquid density ( $\rho_l$ )	956.3	943.4	931.7	kg/m <sup>3</sup>
Gas density ( $\rho_g$ )	0.655	1.132	1.654	kg/m <sup>3</sup>
Dynamic viscosity for liquid ( $\mu_l$ )	0.000273	0.0002325	0.0002062	kg/sm
Dynamic viscosity for gas ( $\mu_g$ )	0.0000122	0.00001295	0.00001349	kg/sm
Specific heat capacity for bed ( $c_{p,s}$ )	775	775	775	J/kgK
Specific heat capacity for liquid ( $c_{p,l}$ )	4217	4241	4267	J/kgK
Specific heat capacity for gas ( $c_{p,g}$ )	2032	2099	2171	J/kgK
Thermal conductivity for bed ( $\lambda_s$ )	2.0	2.0	2.0	W/Km
Thermal conductivity for liquid ( $\lambda_l$ )	0.6819	0.6866	0.6888	W/Km
Thermal conductivity for gas ( $\lambda_g$ )	0.025	0.02701	0.02864	W/Km

#### 5.2.2.1 Comparison to MEWA results

A uniform mesh similar to the one used in the MEWA simulations was one of the meshes used in the 2D Fluent simulations, shown in Fig. 15. The same porous-media description as in the MEWA simulation was used for the pool outside the conical bed. The MTD friction model was used in both simulations. Fig. 16 and Fig. 17 compare the results of the MEWA and Fluent simulations for the total heating power of 26 kW.

Both models predict that dryout is formed in the tip of the cone as shown in the contour images of saturation and particle temperature in Fig. 16. In the Fluent simulation, the dryout zone and the region of increased temperature are larger than in the MEWA simulation. The greatest steam content is formed at the interface of the debris bed and the pool region in the Fluent simulation, and the dry zone spreads downwards in this area.

The velocity vectors in Fig. 17 show that a circulation is formed in the pool in both simulations. In the Fluent simulation, the flow in the porous zone is mostly co-current. Note that the contours of velocity are slightly different in the figure: Fluent shows the velocity magnitude, MEWA shows the axial (vertical) velocity (due to different visualization capabilities).

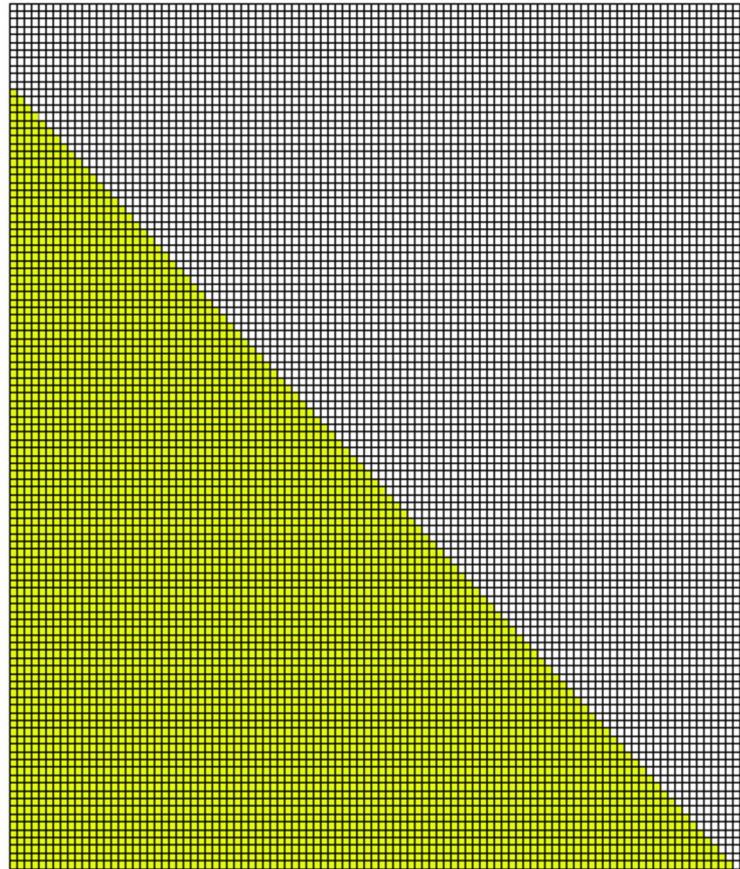


*Fig. 15. Computational mesh used in MEWA and Fluent simulations for the conical bed.*

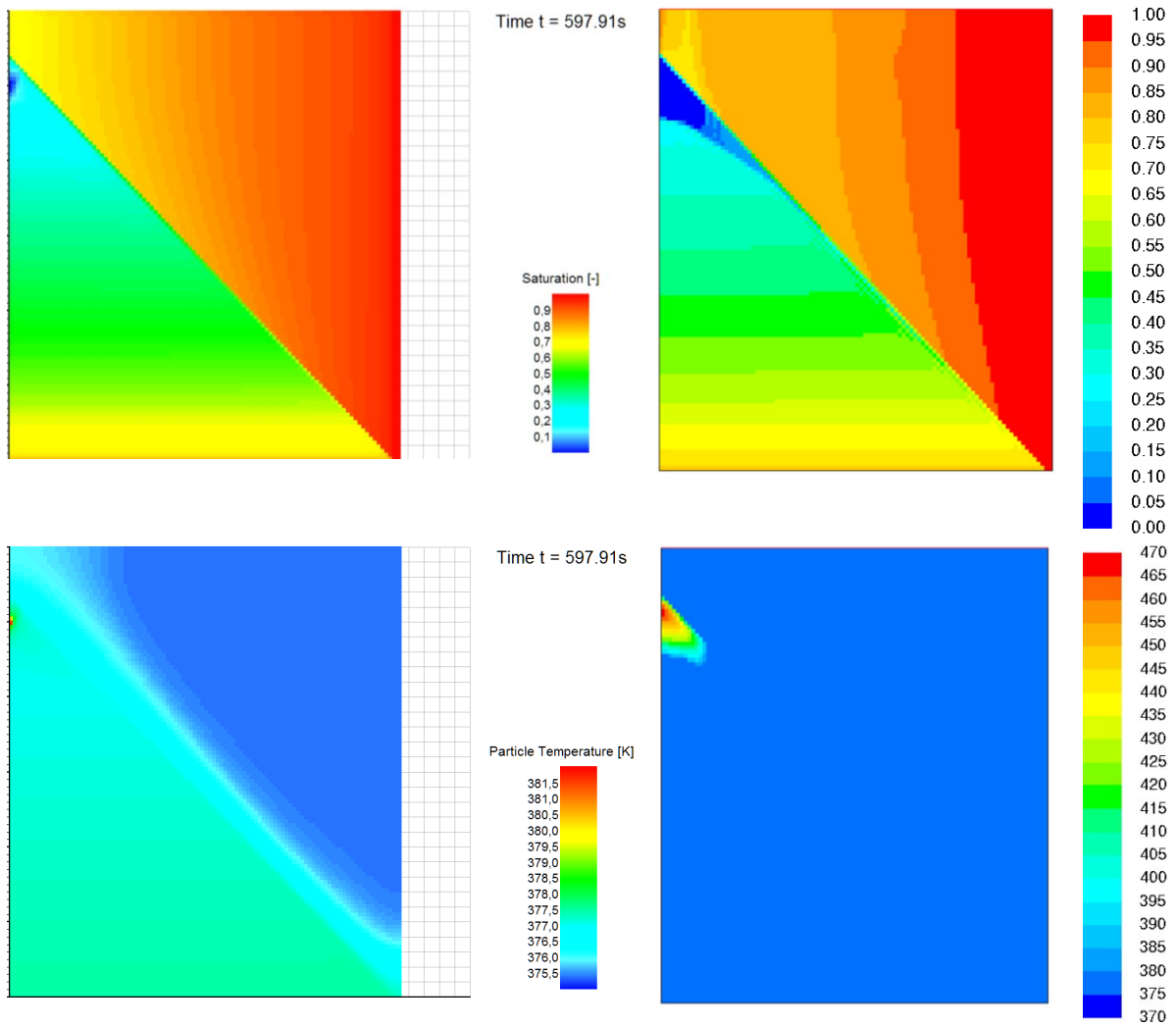


Fig. 16. Comparison of the MEWA (left) and CFD (right) results. Top row: Contours of the liquid saturation. Bottom row: Contours of the particle temperature (K). The CFD simulation assumes the open pool is a similar porous medium as in the MEWA simulation. The MTD model applied and the total heating power is 26 kW.



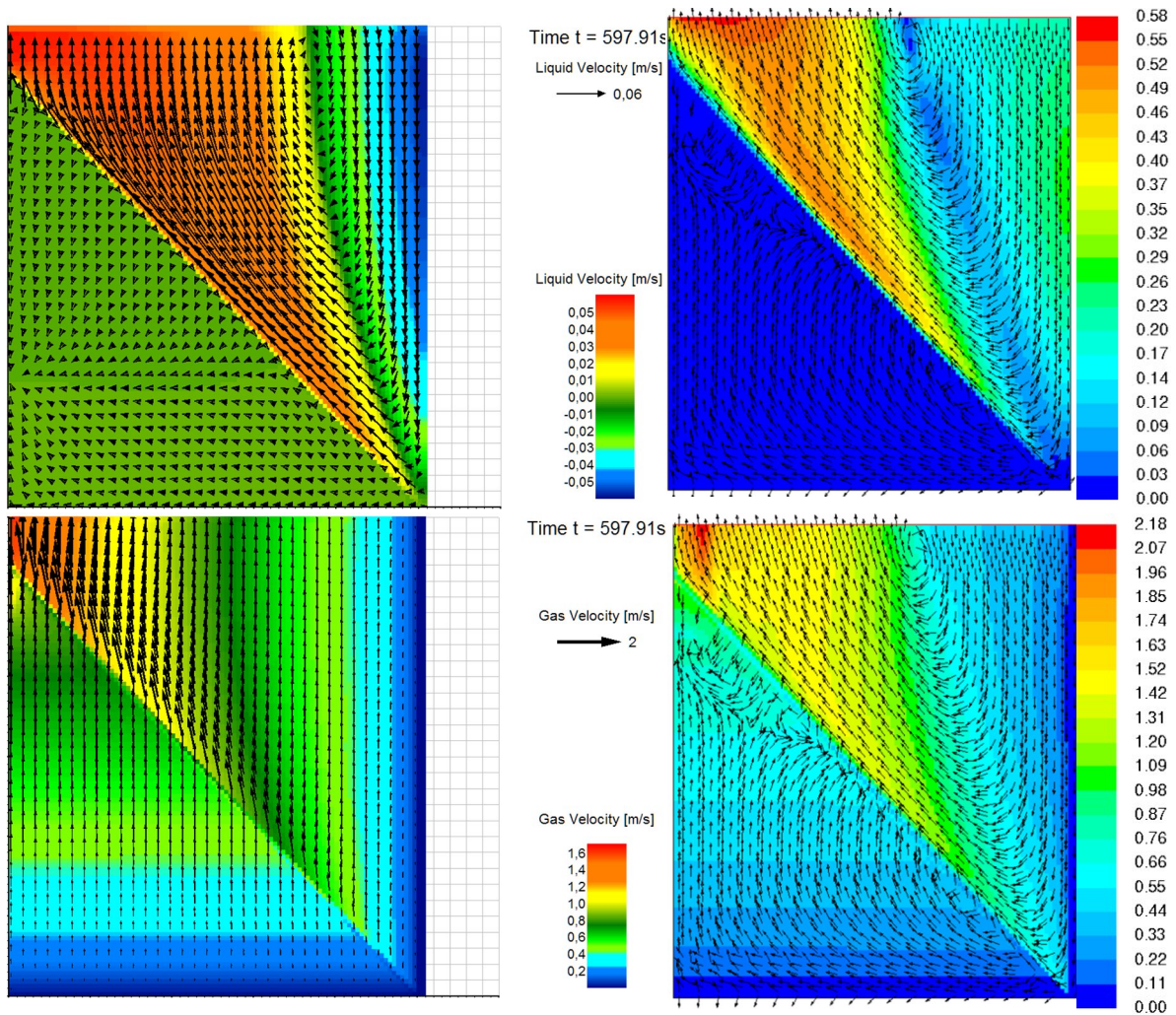


Fig. 17. Vectors of gas and liquid physical velocities in the MEWA (left) and CFD (right) simulations. In MEWA figures, the contours represent velocities in the axial direction. In CFD figures, the contours of velocity magnitude are presented. The MTD model is applied and the total heating power is 26 kW.

### 5.2.2.2 Influence of the pool model

In the CFD modelling discussed above, the pool outside the conical bed is assumed to be a porous bed with large porosity (99 %) and large particles (1 cm). The MTD-based friction forces were calculated accordingly and the flow was assumed to be laminar. In order to study the importance of these modelling assumptions, another, more realistic simulation was conducted. Now a turbulent multiphase flow is assumed for the open pool.

Selected simulation results are presented in Fig. 18 which can be compared to the results with the porous pool assumption in Fig. 16 and Fig. 17. Although the contour plots for the liquid saturation do not differ drastically, there are, however, some significant differences. In the open-pool simulation, the particle temperature does not increase more than 2 degrees compared to the 100 degree rise in the porous-pool simulation (Fig. 16). In case of the frictionless pool, the liquid velocity above the cone is larger resulting in a larger pressure above the cone tip and thus more flow downward. Consequently, large mass fluxes cool the solid particles more.

In addition, in the pool the maximum slip velocity is now about 0.5 m/s compared to about 1.5 m/s in the porous-pool simulation. The maximum slip velocity is still somewhat larger than the terminal slip velocity of about 0.35 m/s because the gas phase accelerates sooner above the bed.

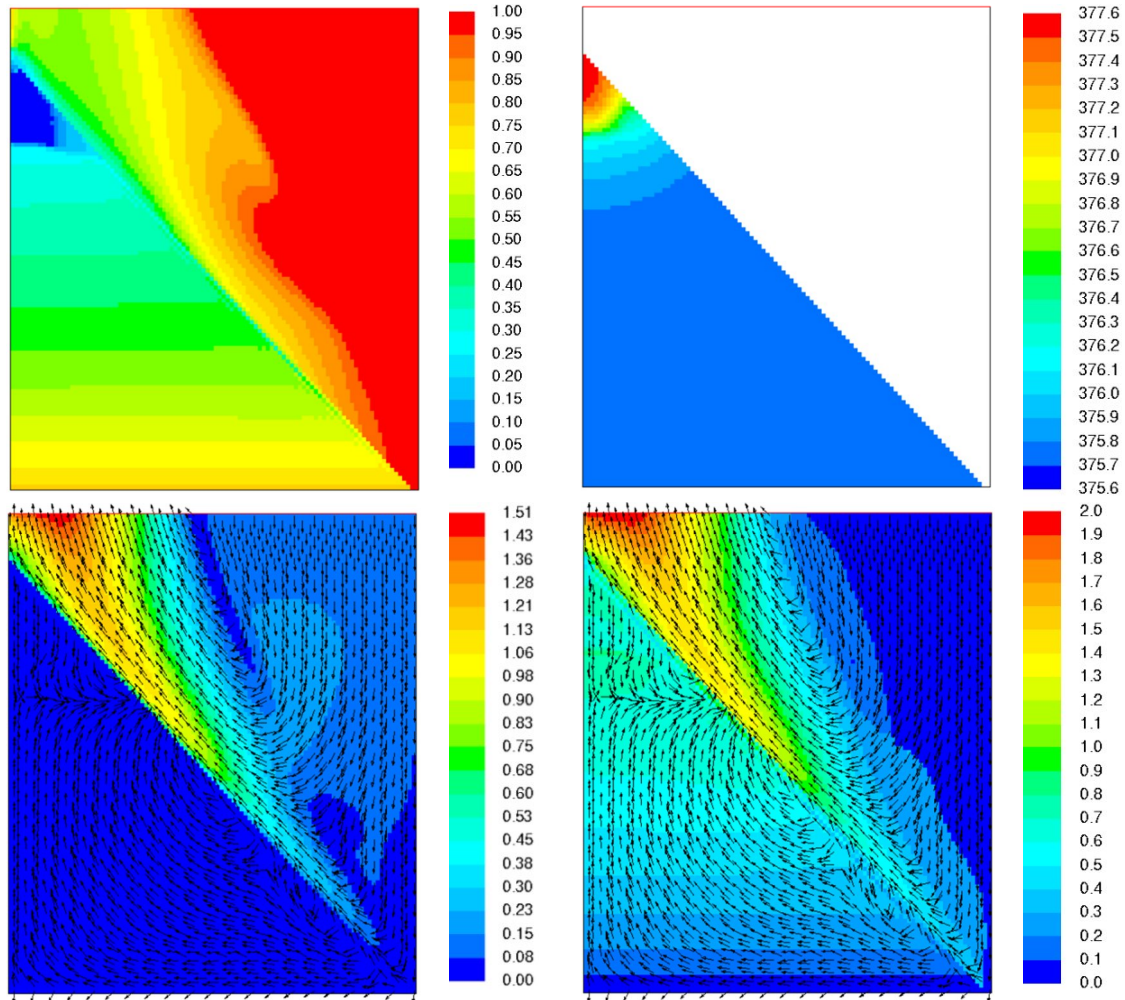


Fig. 18. Results for a CFD simulation assuming the open pool is a free-flow zone with a turbulent multiphase flow ( $k-\epsilon$  dispersed turbulence model). Top left: liquid saturation, top right: particle temperature (K), bottom left: magnitude of the physical liquid velocity (m/s), bottom right: magnitude of the physical gas velocity (m/s). The MTD model is applied and the total heating power is 26 kW.

### 5.2.2.3 Mesh dependency study

A mesh dependence study was conducted with four different spatial discretizations of the computational domain for the conical debris bed:

- MEWAMesh: the rectilinear 2D mesh used in the MEWA simulations (Fig. 15)
- DenseMesh: a relatively dense 2D mesh depicted in Fig. 19



- Adapt2x: a 2D mesh in which the geometry of the filling adapter is taken into account in the mesh and the mesh is adapted twice in the vicinity of the filling adapter (Fig. 20).
- 3DMesh: a relatively coarse 3D mesh (Fig. 21).

In the mesh dependency study, pressure was taken to be 1.1 bar and the total heating power 26 kW. The pool outside the bed was modelled as a frictionless free-flow zone with a turbulent multiphase flow. The dispersed k- $\epsilon$  turbulence model was utilized. The MTD friction model was used in the bed region.

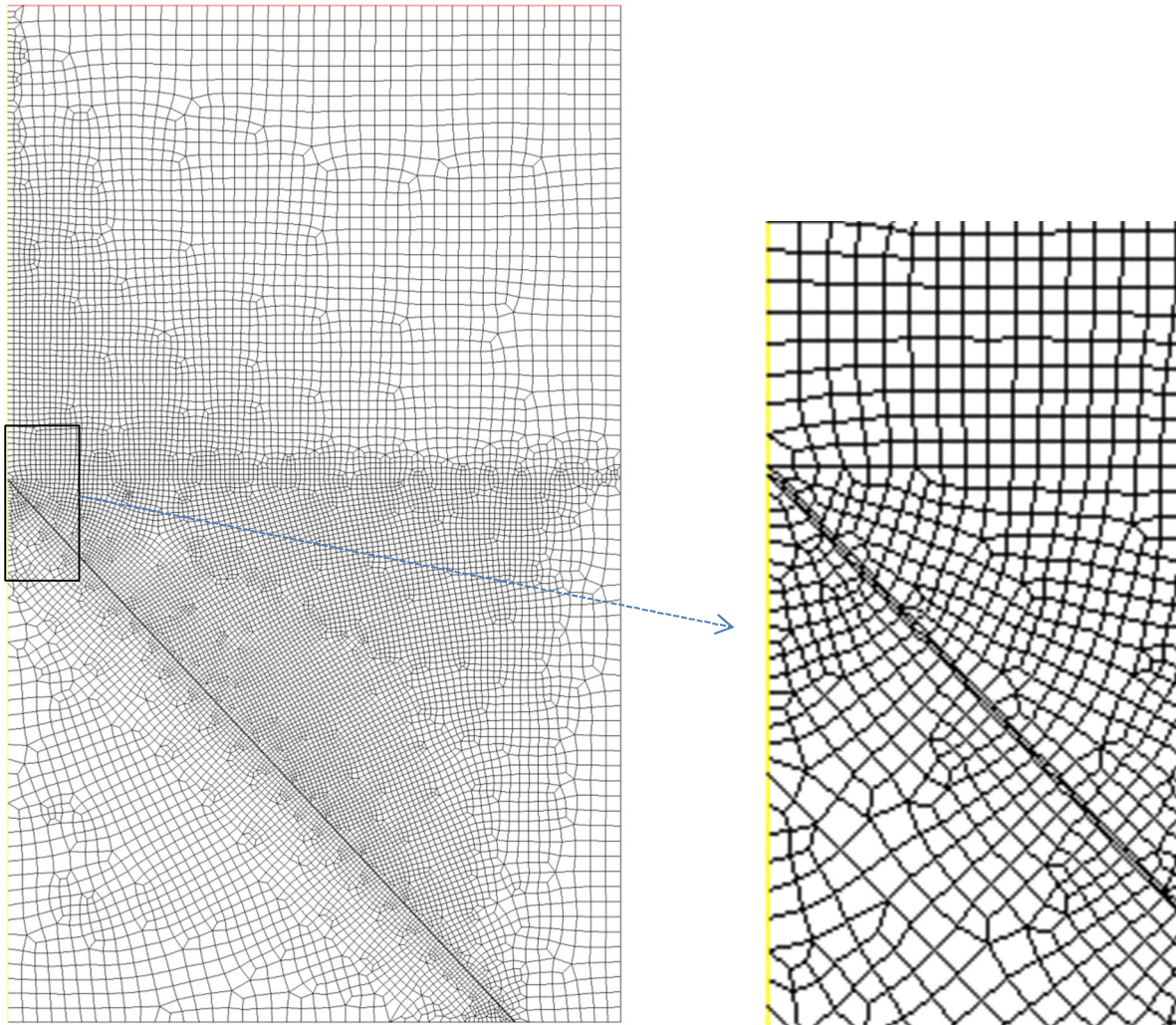


Fig. 19. Computational 2D mesh DenseMesh for the conical bed.

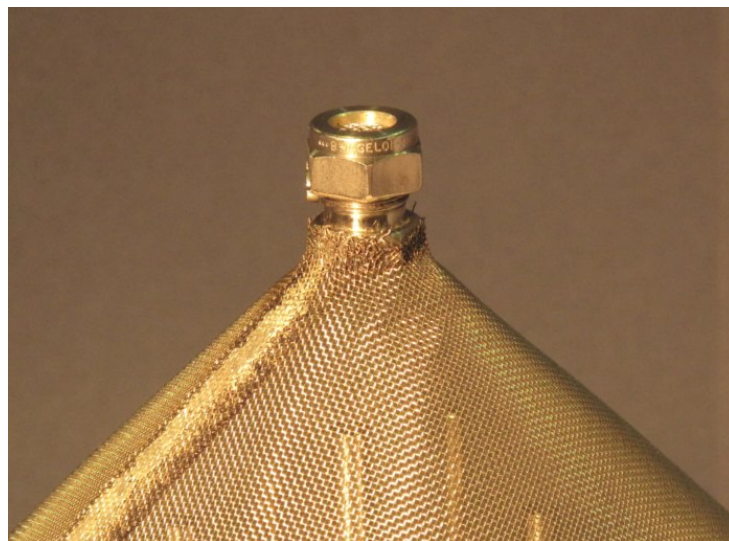
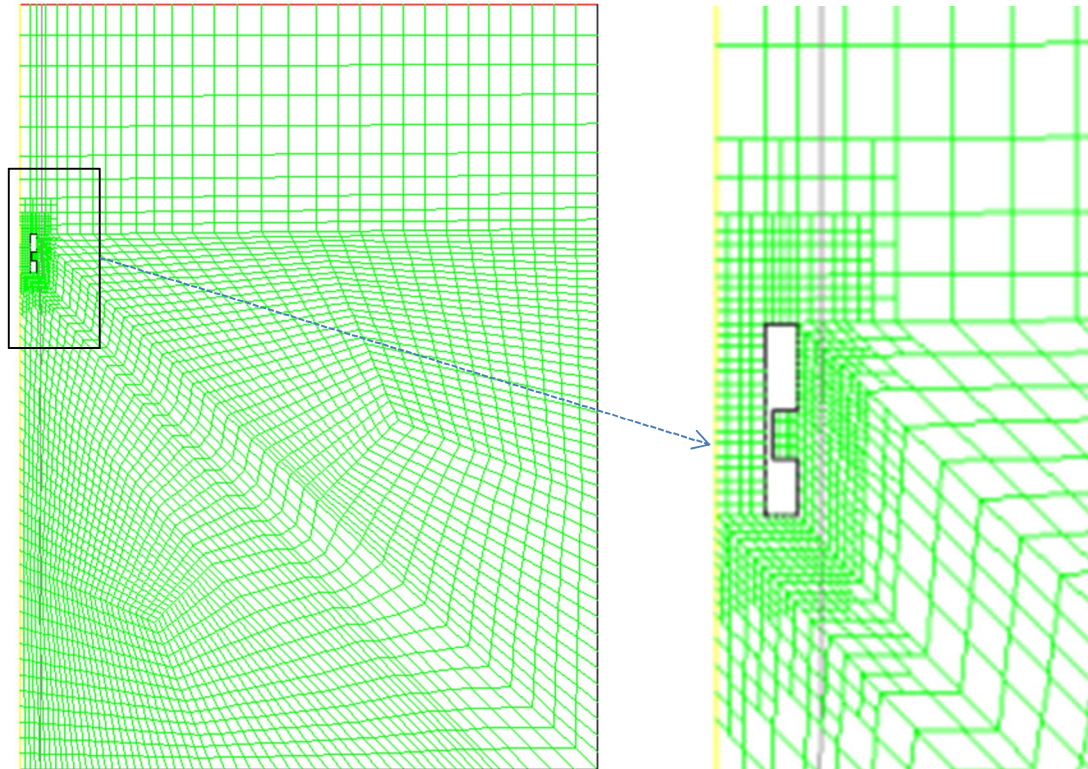
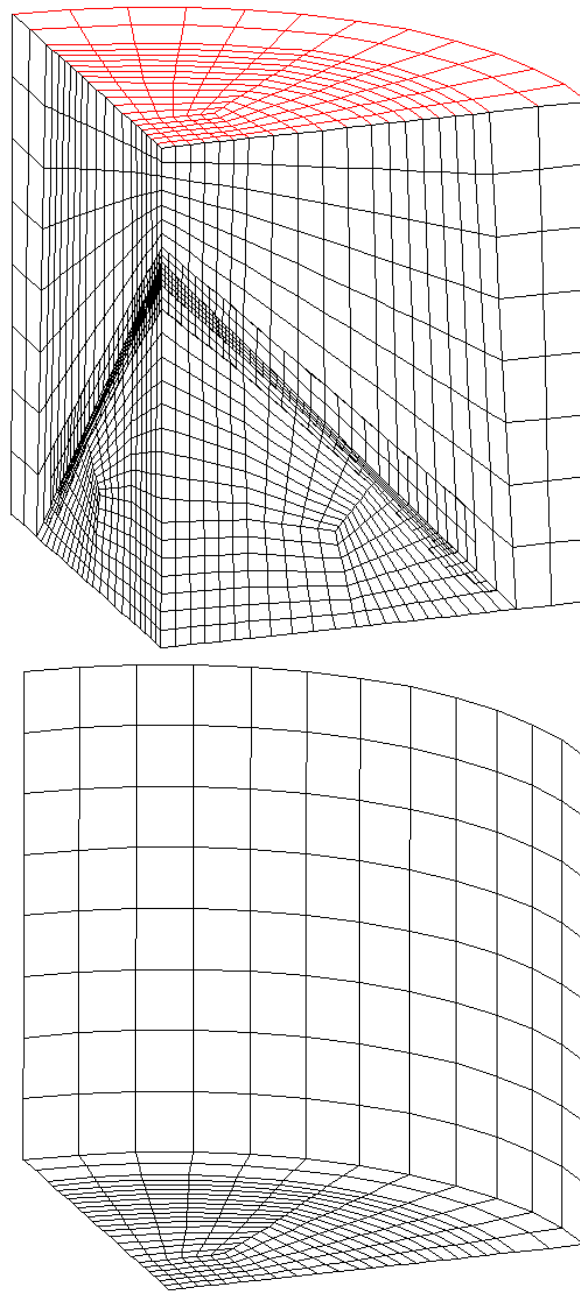


Fig. 20. Computational 2D mesh Adapt2x for the conical bed (top) and the structure in the top of the conical test bed which is modelled by the adaptation in the mesh (bottom).



*Fig. 21. Computational 3D mesh (3DMesh) for the conical bed.*

Fig. 22 and Fig. 23 show the contours of liquid saturation and particle temperature for all four meshes. The vertical lines represent the location of the multi-point thermocouple ( $r = 2.1$  cm) in the experiments. In all the cases, the approximate location and size of the dryout zone is similar. The particle temperature stabilizes to 380 – 570 K, with the MEWAmesh indicating the lowest temperature and the 3DMesh the highest. In three of the four meshes in the simulations (DenseMesh, Adapt2x and 3Dmesh) the dry zone reaches down along the surface of the cone (the interface of porous zone and pool).



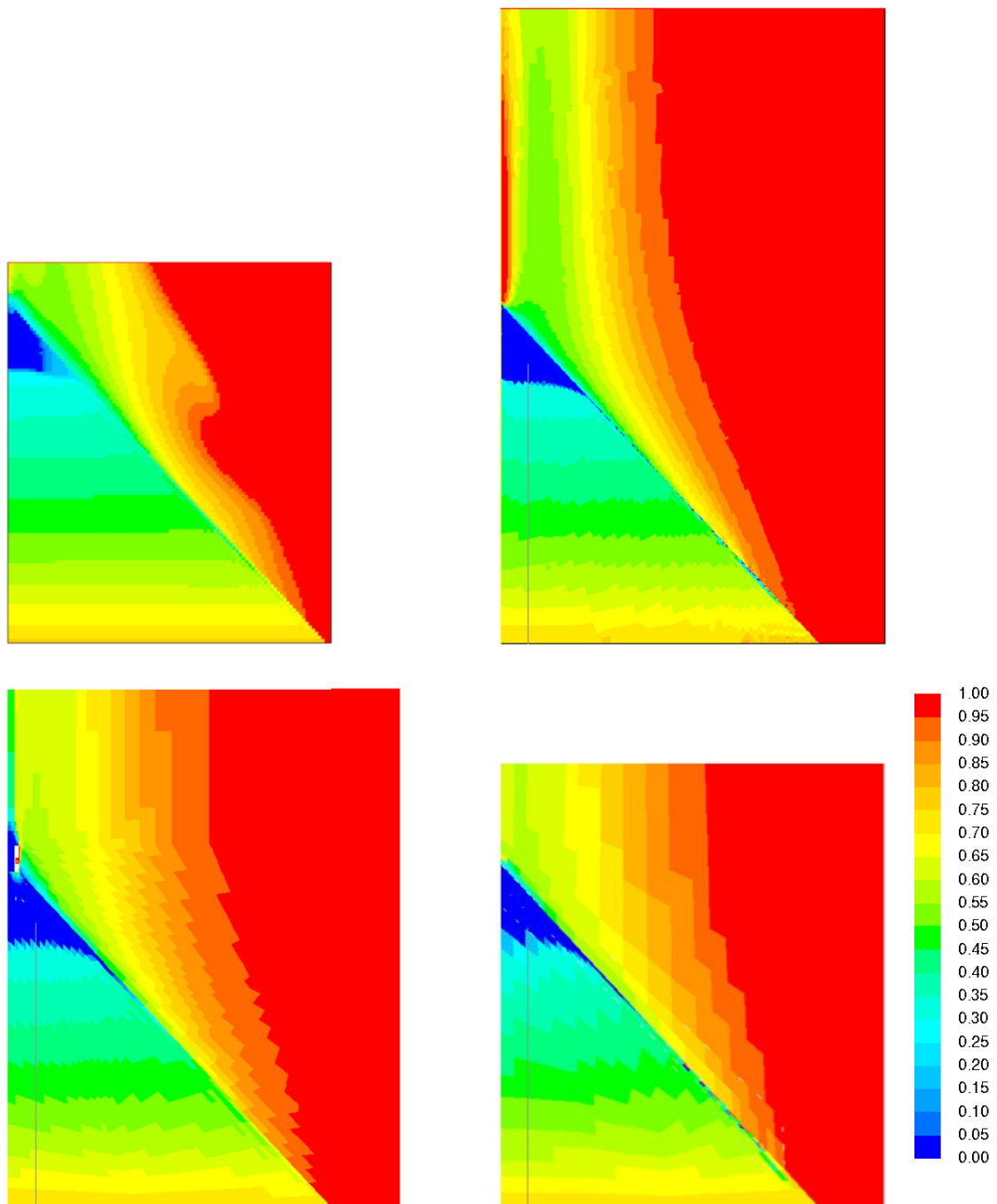


Fig. 22. Contours of the liquid saturation for the meshes MEWAMesh (top left), DenseMesh (top right), Adapt2x (bottom left,) and 3DMesh (bottom right) in the CFD simulation of the conical bed. The MTD model is applied and the heating power is 26 kW ( $p = 1.1$  bar).

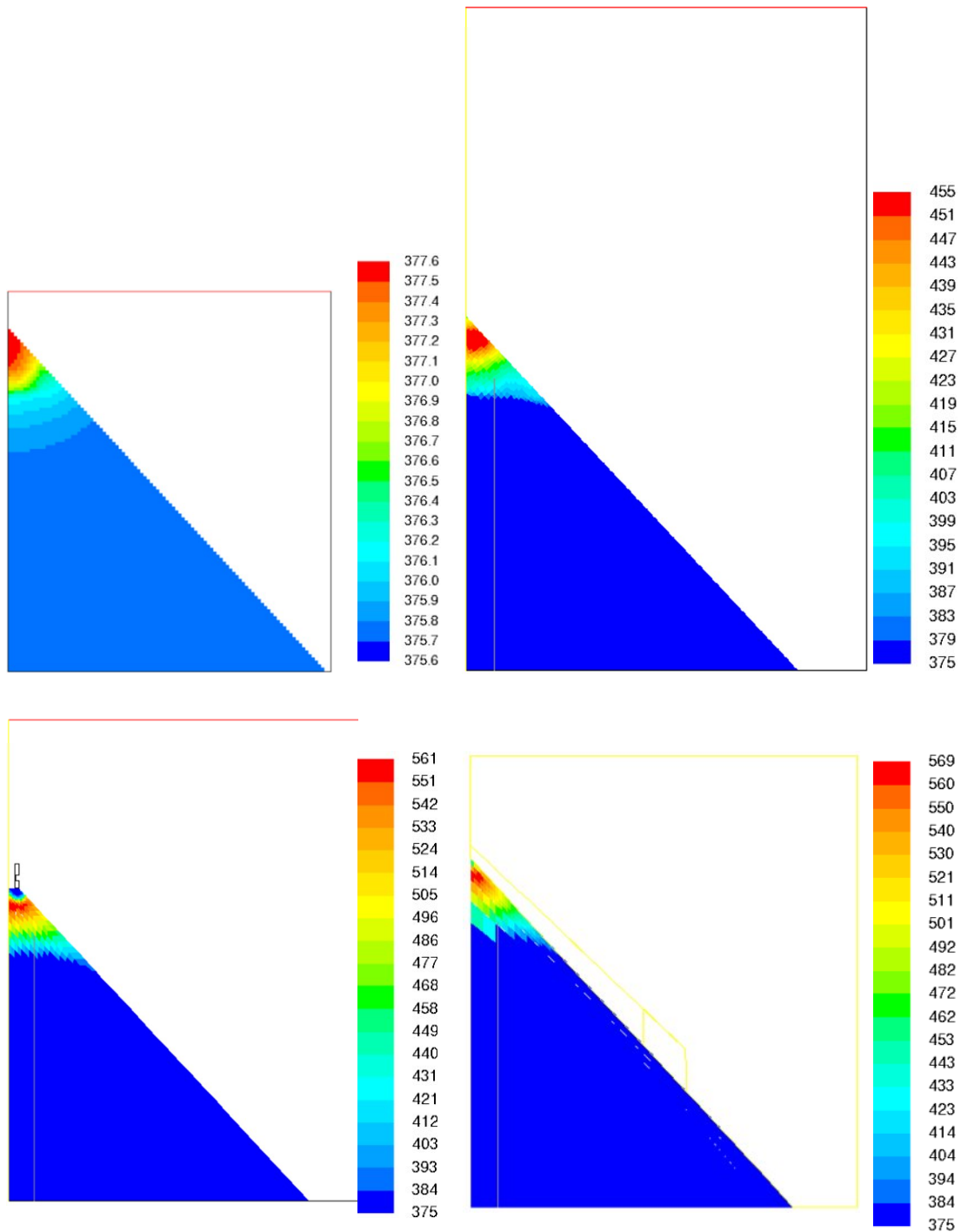


Fig. 23. Contours of the solid temperature for the meshes MEWAMesh (top left), DenseMesh (top right), Adapt2x (bottom left,) and 3DMesh (bottom right) in the CFD simulation of the conical bed. The MTD model applied and the heating power is 26 kW ( $p = 1.1$  bar).

#### 5.2.2.4 Influence of the heating power

The simulated liquid saturation for the three heating powers of 18, 26 and 30 kW is presented in Fig. 24 ( $p = 1.1$  bar). The solid temperature is presented in Fig. 25. The simulations were done with the Adapt2x mesh. It is seen that even with increasing heating power, the tip of the cone at the axis of the geometry does not dry out, rather, the dry zone is spread downwards near the surface of the cone. Dryout is already reached at the power of

18 kW which is not the case in MEWA simulations. In MEWA the dryout starts at 26 kW. Fluent predicts the incipient dryout to occur with lower power than MEWA but the dryout zone is very small and it may not make sense to take the formation of the first dry zone (or zero saturation) as the criterion for coolability. Instead, the temperature increase and the volume of the dryout zone should be considered.

The post-dryout temperatures in Fig. 25 at the different power levels show that the particle temperature stabilized to 480 – 660 K. For comparison, the particle temperature and saturation distributions in MEWA at 34 kW power are presented in Fig. 26. At this power level, the dryout zone size is comparable to the one in the Fluent simulations. In the end of the simulation, temperature is higher in the Fluent simulations but this is because the MEWA simulation did not reach steady-state within the simulation time.

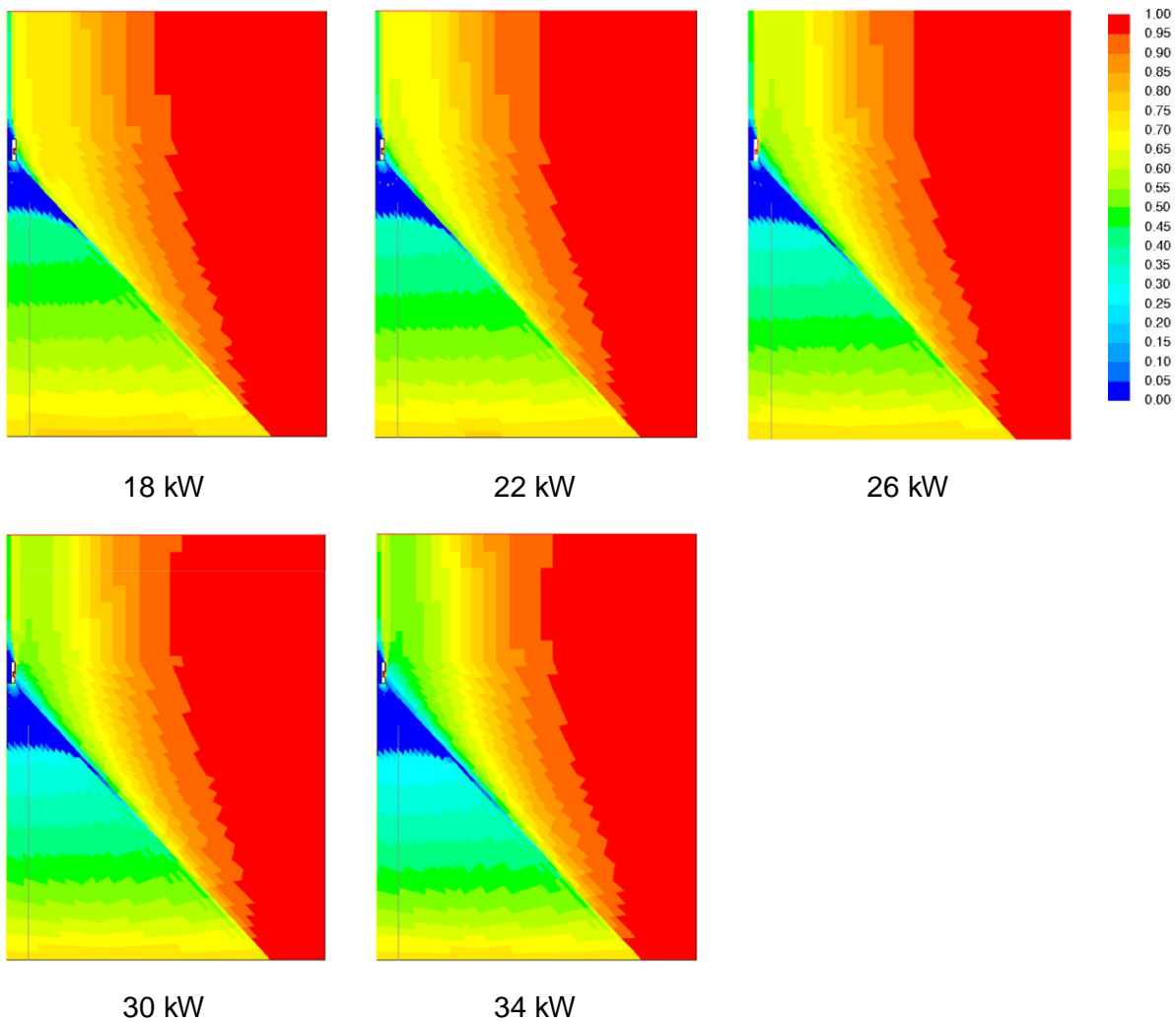


*Fig. 24. Contours of the liquid saturation. Computational results for the conical bed assuming the heating powers is 18, 22, 26, 30, and 34 kW. The MTD model applied in the CFD simulation ( $p = 1.1$  bar).*

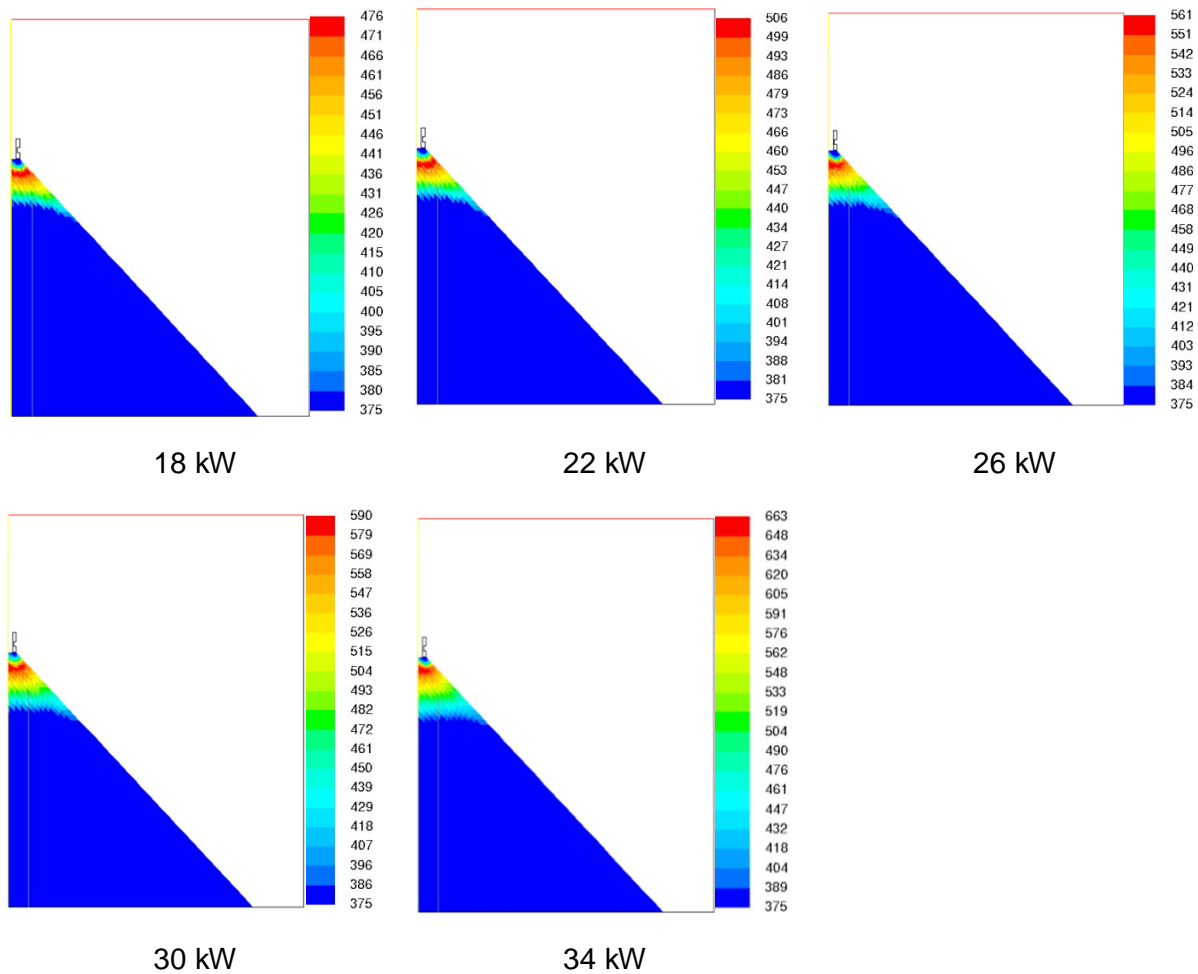


Fig. 25. Contours of the bed particle temperature. Computational results for the conical bed assuming the heating powers is 18, 22, 26, 30, and 34 kW. The MTD model is applied in the CFD simulation ( $p = 1.1$  bar).

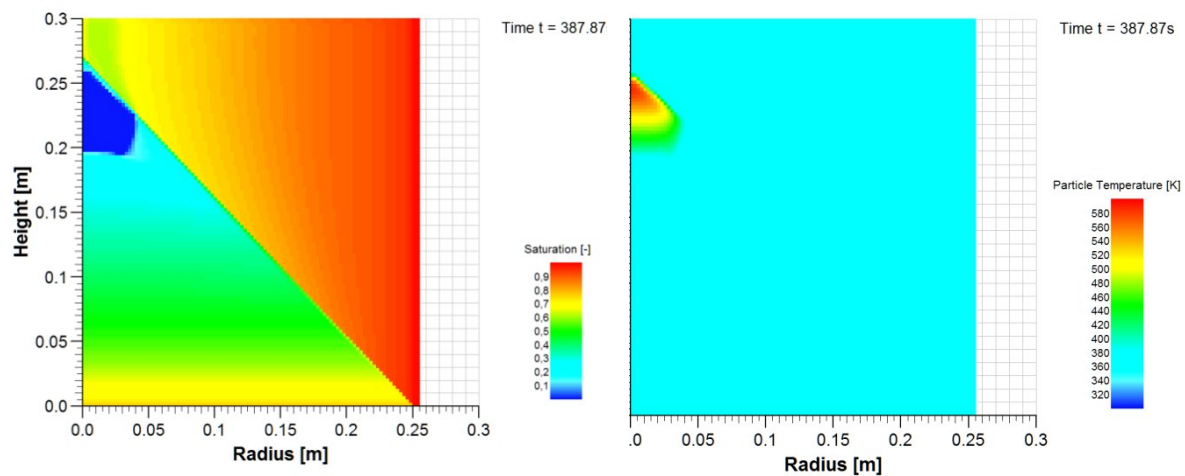


Fig. 26. Contours of the liquid saturation (left) and particle temperature (right) in the MEWA simulation at 34 kW power and MTD model ( $p = 1.1$  bar).



### 5.2.2.5 Pressure variations

Fig. 27 shows the contour plots of the liquid saturation from the CFD simulations of the conical bed for operating pressures 1.1, 2 and 3 bar. The volume of the dryout zone is decreased with increasing pressure. The results are consistent with the experimentally observed and analytically predicted increase in coolability with increasing pressure. This is mainly due to the increase in the steam density (smaller steam volume). However, the change is relatively small due to the sensitivity of the cone tip to local dryout and the increase to 3 bar does not completely remove the dry zone.

The contours of temperature at the different power levels are presented in Fig. 29. Correspondingly to the smaller dryout zone, the maximum solid temperatures are lower for higher pressures. (Note that the relative temperature increase is even smaller because the saturation temperature is greater in greater pressures.)

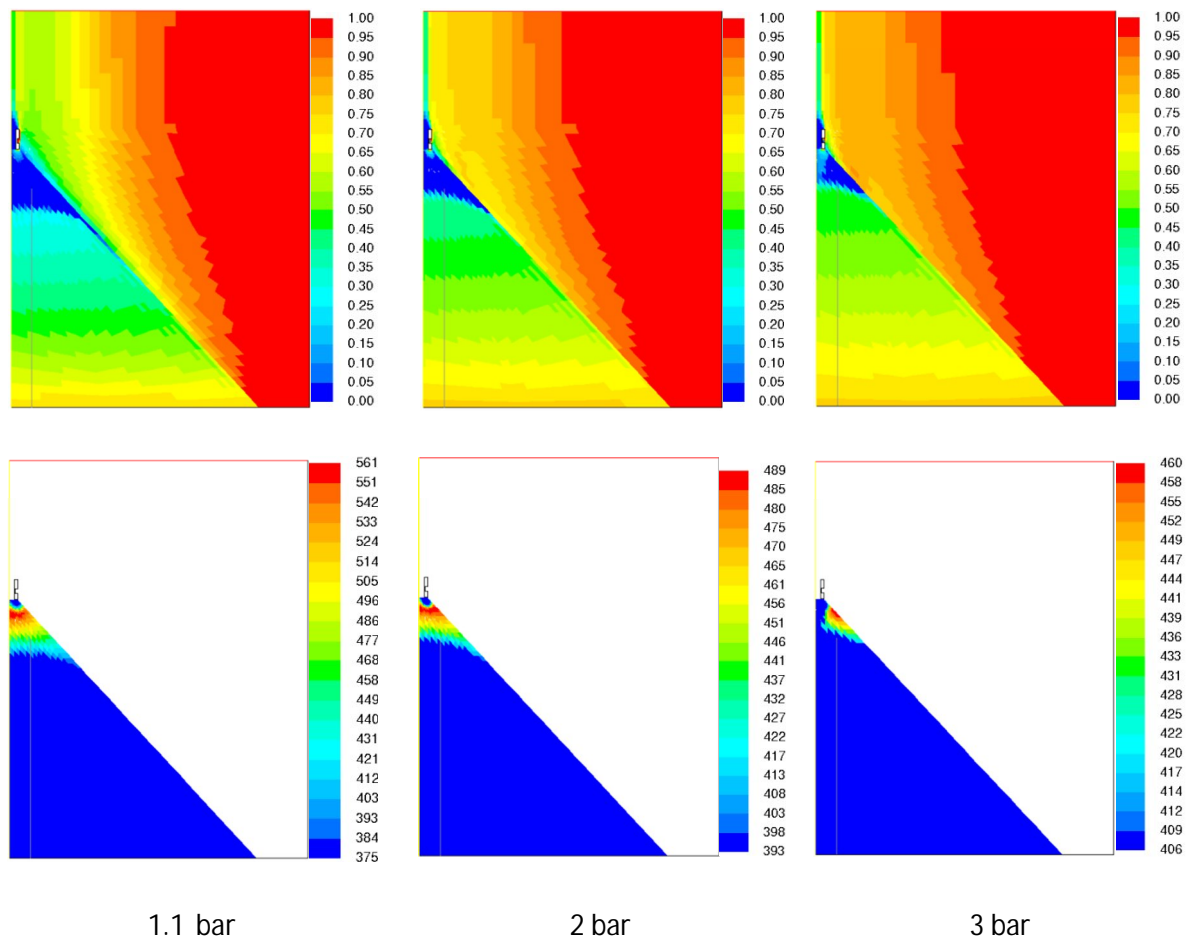


Fig. 27. Influence of pressure in the conical bed. Contours of the liquid saturation (top row) and bed particle temperature (K) (bottom row). Computational results for the operating pressure of 1.1, 2 and 3 bar (from left). The MTD model is applied in the CFD simulation and the heating power is 26 kW.

### 5.2.3 Fully flooded cylinder

The simulation set-up for the fully flooded cylinder, C-10, is presented in Fig. 5. A similar axisymmetric grid has been used as in the MEWA simulations. Simulations were conducted with the same three drag force models as the MEWA simulations (Reed, Tung & Dhir and modified Tung & Dhir) and, for each case, the porous media model and the free-flow model with turbulent multiphase flow were tested for the open pool region. In the cases with porous zone pool, the same properties as in the MEWA simulations were used (porosity 0.99 and particle diameter 10 mm).

Table 6. Physical conditions and material properties in the CFD modelling of the fully flooded cylinder.

Quantity (symbol)	Value (unit)
Pressure ( $p$ )	1.3 bar
Heating power	34(Reed)/41(TD)/42(MTD) kW
Bed particle diameter ( $d$ )	0.97 mm
Bed porosity ( $\varepsilon$ )	0.40
Bed material density ( $\rho_s$ )	4200 kg/m <sup>3</sup>
Liquid density ( $\rho_l$ )	952.8 kg/m <sup>3</sup>
Gas density ( $\rho_g$ )	0.765 kg/m <sup>3</sup>
Dynamic viscosity for liquid ( $\mu_l$ )	0.0002605 kg/sm
Dynamic viscosity for gas ( $\mu_g$ )	0.0000124 kg/sm
Specific heat capacity for bed ( $c_{p,s}$ )	775 J/kgK
Specific heat capacity for liquid ( $c_{p,L}$ )	4222 J/kgK
Specific heat capacity for gas ( $c_{p,g}$ )	2048 J/kgK
Thermal conductivity for bed ( $\lambda_s$ )	2.0 W/Km
Thermal conductivity for liquid ( $\lambda_l$ )	0.6835 W/Km
Thermal conductivity for gas ( $\lambda_g$ )	0.02551 W/Km

#### 5.2.3.1 Water pool as porous zone

The saturation distributions in dryout conditions in the Fluent simulations are compared to the corresponding MEWA distributions in Fig. 28 - Fig. 30. Here, the water pool is treated as a porous zone. The results obtained with the Reed model are shown in Fig. 28, the Tung & Dhir results in Fig. 29 and the modified Tung & Dhir results in Fig. 30. The flow patterns in the pool and in the porous zone in the Fluent simulations are shown in Fig. 36 - Fig. 41 which show the vectors of superficial fluid velocities (as in the Fluent formulation, divided by the phase volume fraction) with the three models.

It is seen that the general trends of saturation distribution and dryout formation are rather similar to the MEWA results, and a similar model dependency is seen. With the Reed model, the steam flow is directly upwards above the debris bed. With the other models with interfacial drag, the steam travels towards the centre with the liquid circulation. In the Fluent simulation near the central axis, there is a pressure increase which causes a small amount of liquid to enter downwards into the porous zone and the void fraction is very low near the centre above the bed. In the calculations with the TD model, the difference between Fluent and MEWA in the pool region is notable even though the saturation distributions in the porous zone are quite similar.

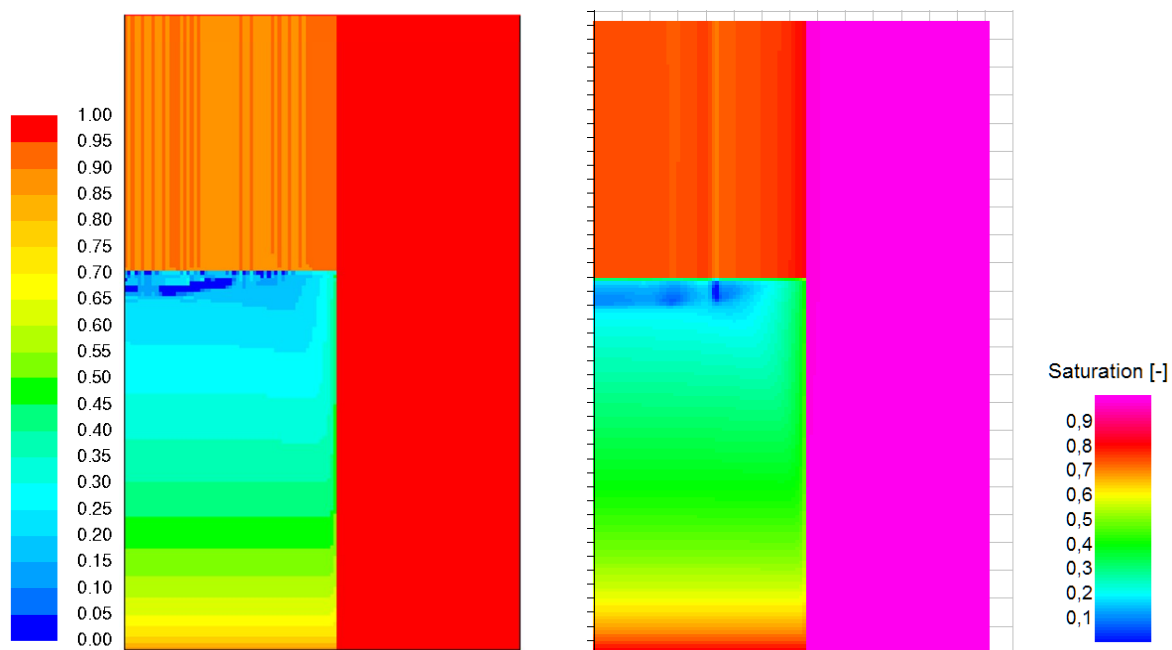


Fig. 28. Contours of liquid saturation in the Fluent simulation (left) and the MEWA simulation (right) with the Reed model and porous zone pool, power level 34 kW.

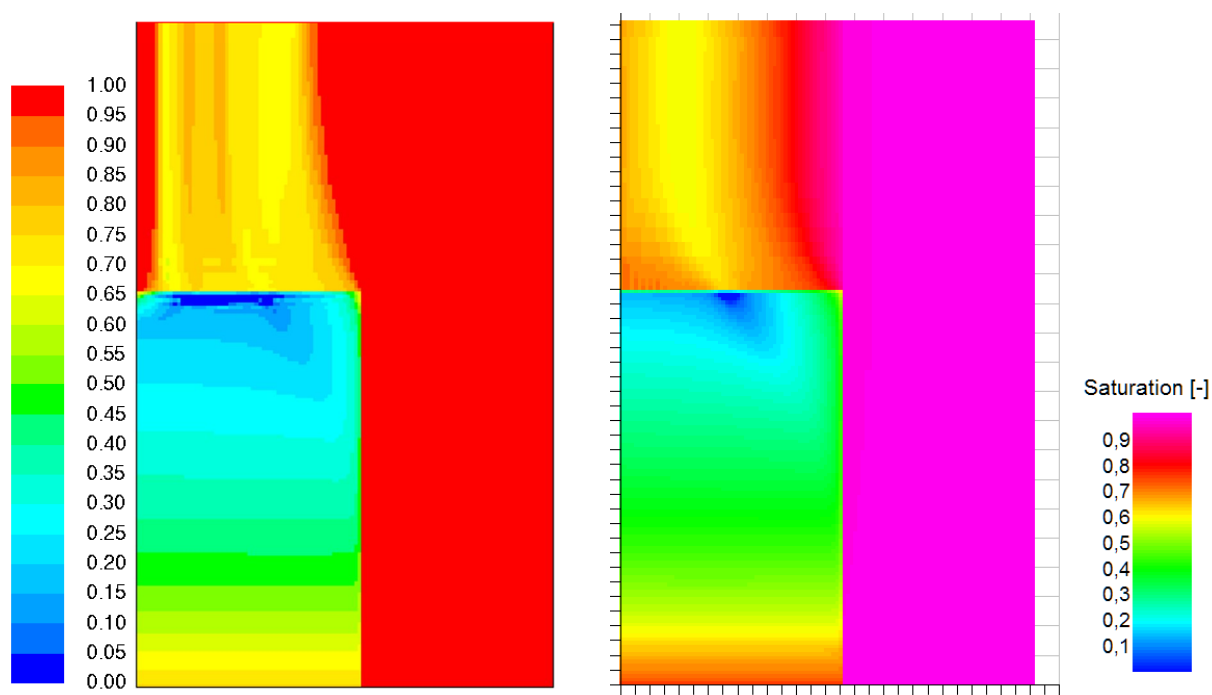


Fig. 29. Contours of liquid saturation in the Fluent simulation (left) and the MEWA simulation (right) with the MTD model and porous zone pool, power level 42 kW.

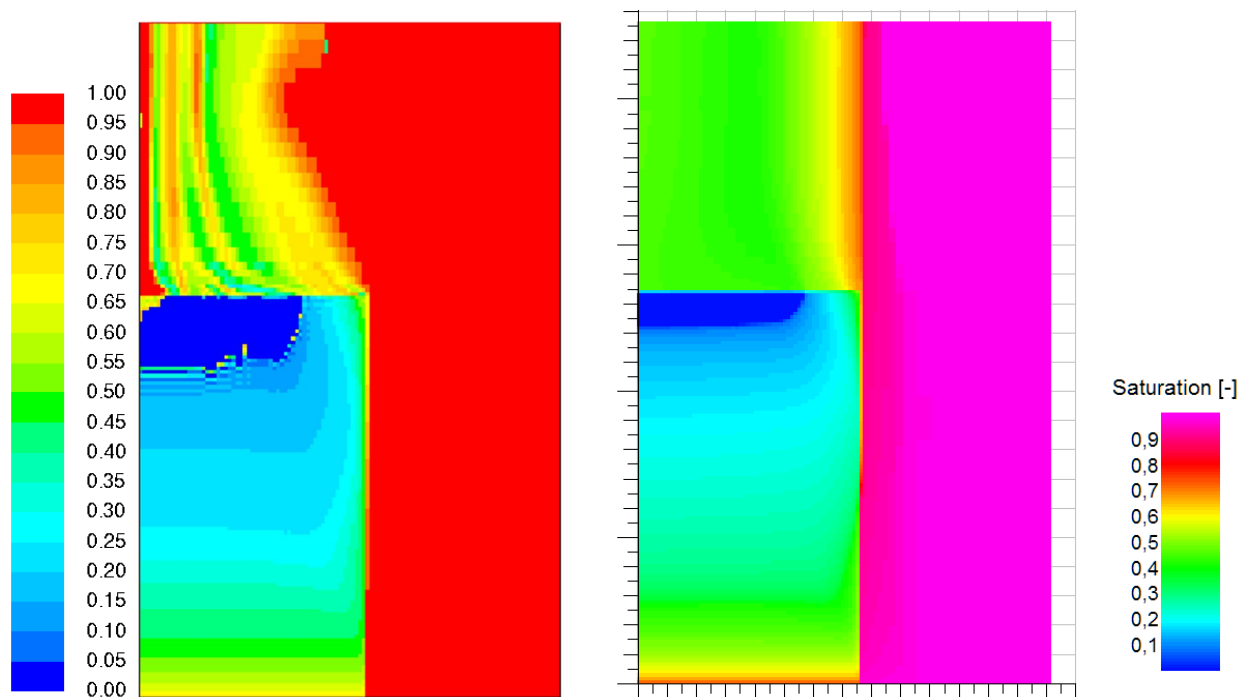


Fig. 30. Contours of liquid saturation in the Fluent simulation (left) and the MEWA simulation (right) with the TD model and porous zone pool, power level 41 kW (post-dryout conditions).

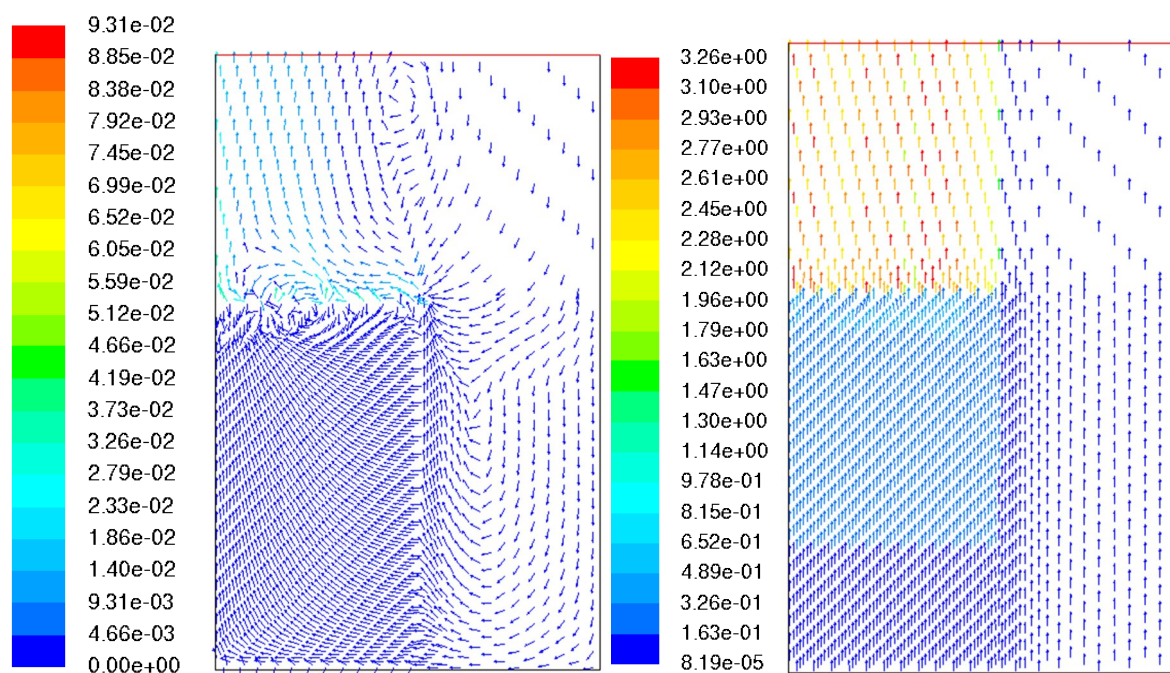


Fig. 31. Vectors of Fluent superficial velocity (superficial velocity / volume fraction) for liquid (left) and gas (right) in the fully flooded cylinder simulation with the Reed model, power level 34 kW.



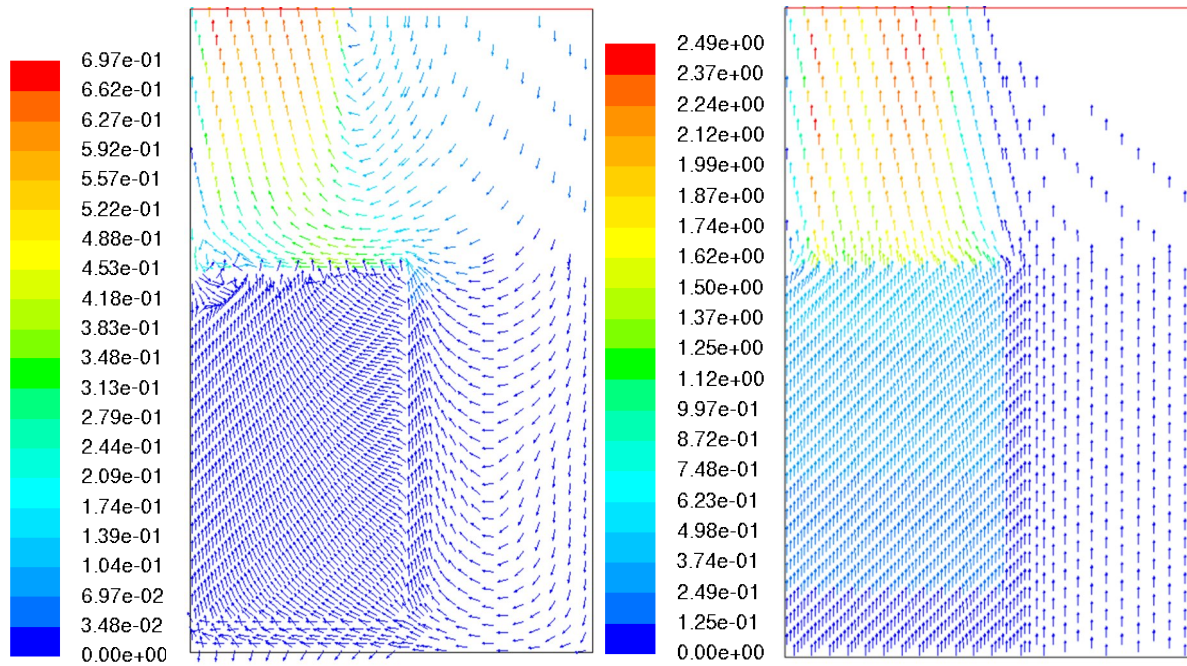


Fig. 32. Vectors of Fluent superficial velocity (superficial velocity / volume fraction) for liquid (left) and gas (right) in the fully flooded cylinder simulation with the MTD model, power level 42 kW.

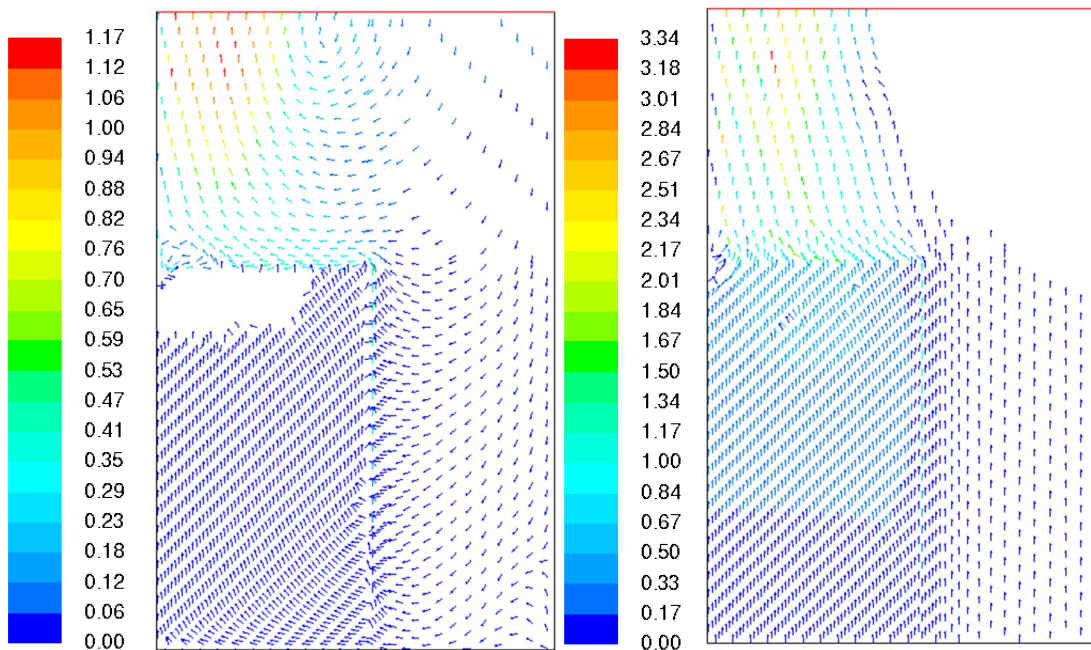


Fig. 33. Vectors of Fluent superficial velocity (superficial velocity / volume fraction) for liquid (left) and gas (right) in the fully flooded cylinder simulation with the TD model, power level 41 kW.

### 5.2.3.2 Water pool with free-flow models

The saturation distributions in dryout conditions in the Fluent simulations are compared to the corresponding MEWA distributions obtained by the different drag force models in Fig. 34 - Fig. 36. The vectors of Fluent superficial velocity are presented in Fig. 37 - Fig. 48. Here, the water pool is modelled as free-flow zone by using the model of Schiller and Naumann (1935) for interfacial drag and the k- $\epsilon$  turbulence model. In this case, the pool behaviour is not dependent on the porous media drag force models as in the previous simulations. The pool

flow appears to be more realistic. On the other hand, in the Reed and MTD simulations, the region of lowest saturation is formed as a thin layer near the surface of the bed.

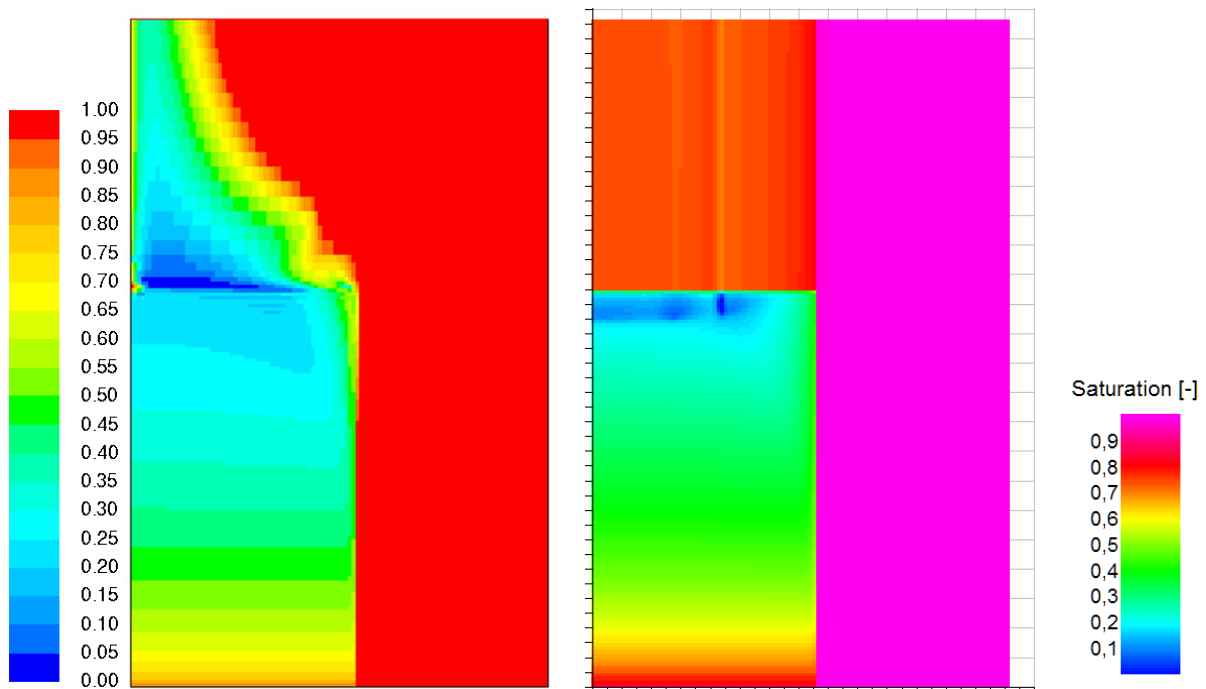


Fig. 34. Contours of liquid saturation in the Fluent simulation (left) and the MEWA simulation (right) with the Reed model and the free-flow pool, power level 34 kW.

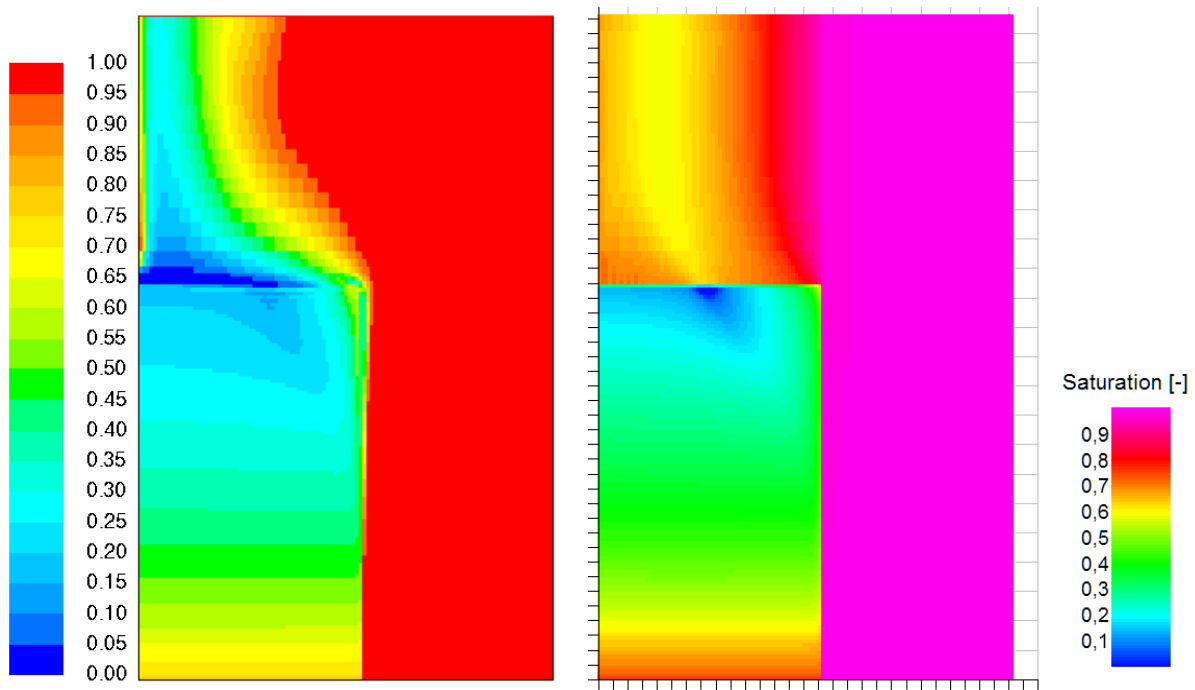


Fig. 35. Contours of liquid saturation in the Fluent simulation (left) and the MEWA simulation (right) with the MTD model and the free-flow pool, power level 42 kW.

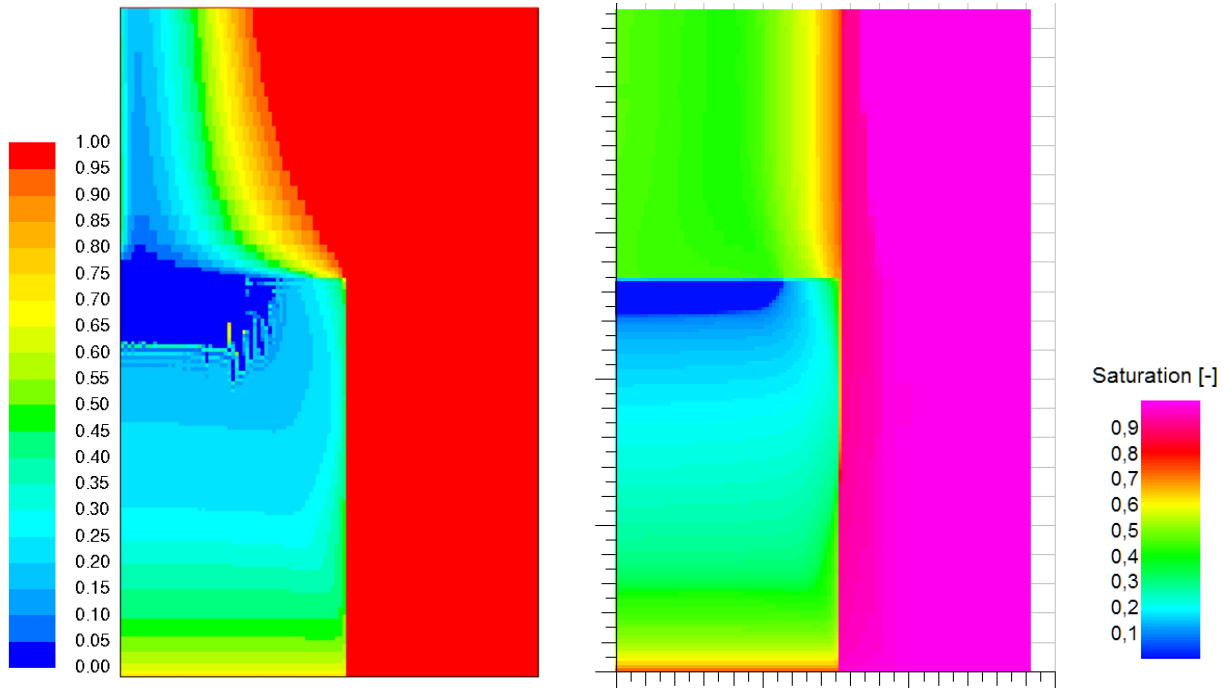


Fig. 36. Contours of liquid saturation in the Fluent simulation (left) and the MEWA simulation (right) with the TD model and the free-flow pool, power level 41kW.

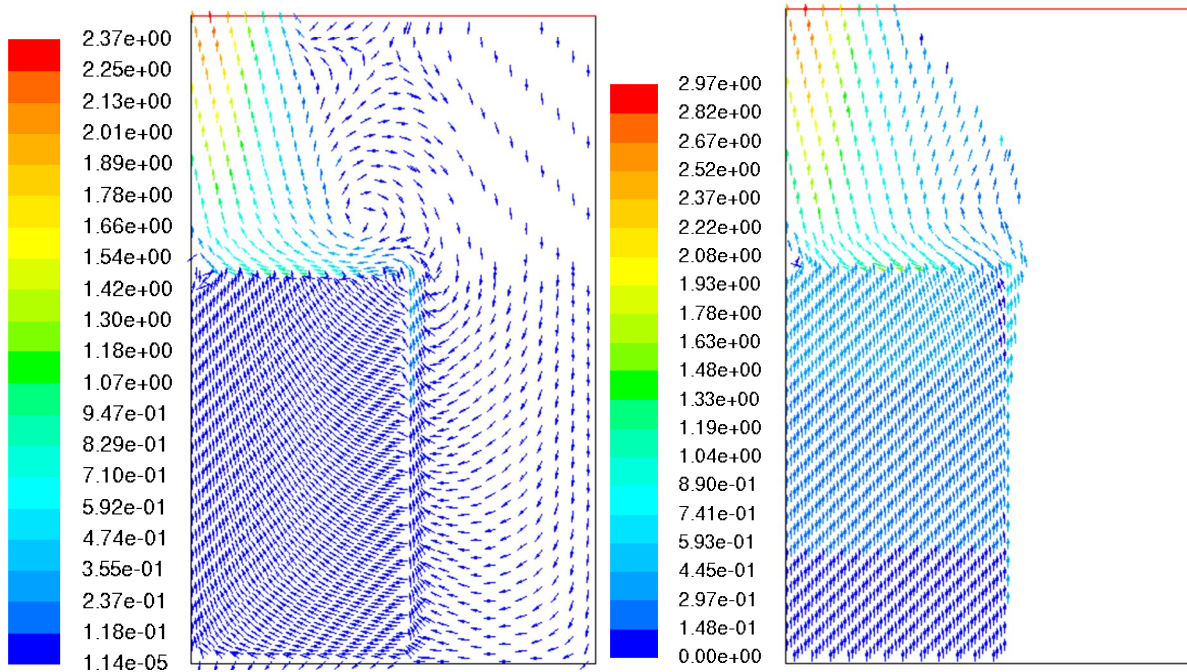


Fig. 37. Vectors of Fluent superficial velocity (superficial velocity / volume fraction) for liquid (left) and gas (right) in the fully flooded cylinder simulation with the Reed model, free flow pool and power level of 34 kW.



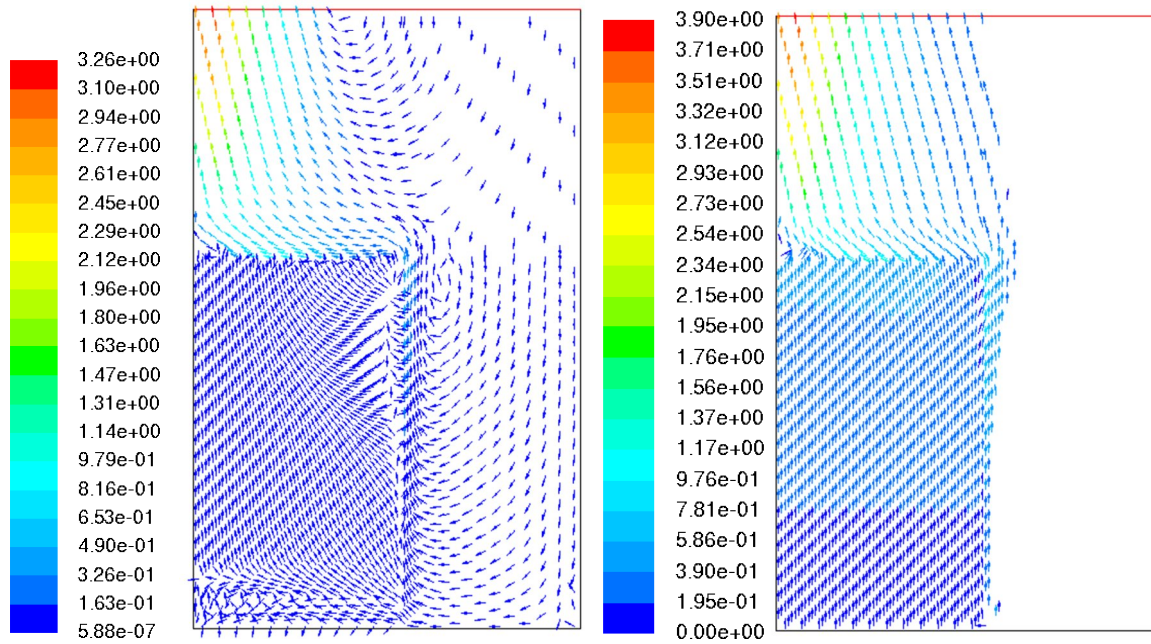


Fig. 38. Vectors of Fluent superficial velocity (superficial velocity / volume fraction) for liquid (left) and gas (right) in the fully flooded cylinder simulation with the MTD model, free flow pool and power level of 42 kW.

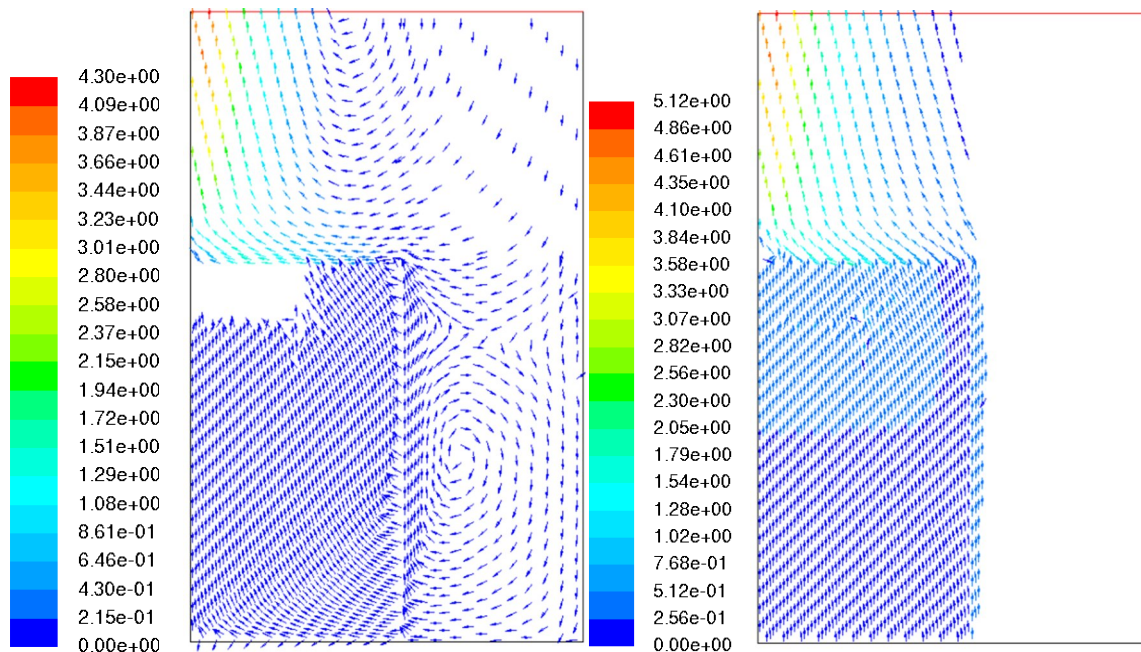


Fig. 39. Vectors of Fluent superficial velocity (superficial velocity / volume fraction) for liquid (left) and gas (right) in the fully flooded cylinder simulation with the TD model, free flow pool and power level of 41 kW.

## 5.2.4 Laterally flooded cylinder

In the 2D CFD simulations of the laterally flooded cylinder and the blocked top surface, the computational mesh is the same as in the MEWA simulation. The mesh is depicted in Fig. 40. The physical conditions and material properties are summarised in Table 7. The

simulations were conducted with the Fluent code applying the superficial velocity formulation. The total heating power is 10 kW.

The contours of the liquid saturation and particle temperature as well as the magnitude of the (physical) velocity with velocity vectors for both phases are shown in Fig. 41 and Fig. 42 for the MTD and Reed models, respectively. The results obtained using the MEWA code with the same 10 kW power are presented in Fig. 43. It is seen that the dryout zone location and size are very similar in both Fluent and MEWA simulations. In the MEWA simulation with 21.9 kW presented in Fig. 7, the dryout zone is larger which demonstrates the effect of the heating power in this case.

The heating power clearly has an effect on the size of the dryout zone but the result does not depend on the friction model or the code which is contrary to the results of the fully flooded cylinder. In the maximum particle temperatures at the end of the simulation, there is a difference between MEWA and Fluent but this is apparently due to different simulation times. The temperature remains transient in post-dryout conditions, increasing continuously.

Considering the pool region, the Reed model ignores the drag force between the liquid and gas phases and therefore, in the pool, the viscous forces in the Fluent simulation create vortices and a steady state is not achieved. With the MTD model, the drag force stabilizes the flow field. The magnitudes of the velocities are not very different. In all three cases, the slip velocity is unphysically large (up to around 4 m/s as it should not be less than 0.4 m/s). The friction model does not influence significantly the simulation results.

*Table 7. Physical conditions and material properties in the CFD modelling of the laterally flooded cylinder.*

Quantity (symbol)	Value (unit)
Pressure ( $p$ )	1.1 bar
Heating power	10 kW
Bed particle diameter ( $d$ )	0.97 mm
Bed porosity ( $\varepsilon$ )	0.40
Bed material density ( $\rho_s$ )	4200 kg/m <sup>3</sup>
Liquid density ( $\rho_l$ )	956.3 kg/m <sup>3</sup>
Gas density ( $\rho_g$ )	0.655 kg/m <sup>3</sup>
Dynamic viscosity for liquid ( $\mu_l$ )	0.000273 kg/sm
Dynamic viscosity for gas ( $\mu_g$ )	0.0000122 kg/sm
Specific heat capacity for bed ( $c_{p,s}$ )	775 J/kgK
Specific heat capacity for liquid ( $c_{p,l}$ )	4217 J/kgK
Specific heat capacity for gas ( $c_{p,g}$ )	2032 J/kgK
Thermal conductivity for bed ( $\lambda_s$ )	2.0 W/Km
Thermal conductivity for liquid ( $\lambda_l$ )	0.6819 W/Km
Thermal conductivity for gas ( $\lambda_g$ )	0.025 W/Km

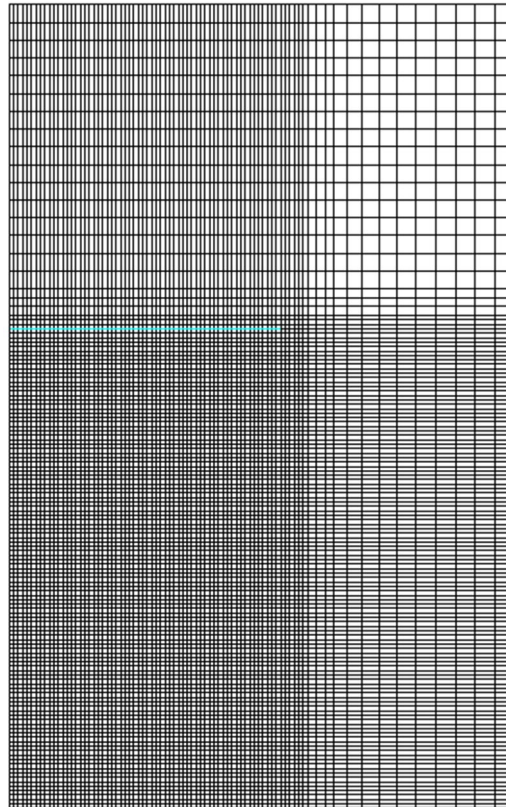


*Fig. 40. Computational mesh used in simulations for the laterally flooded cylinder (C-11), the highlighted region is the top plate.*

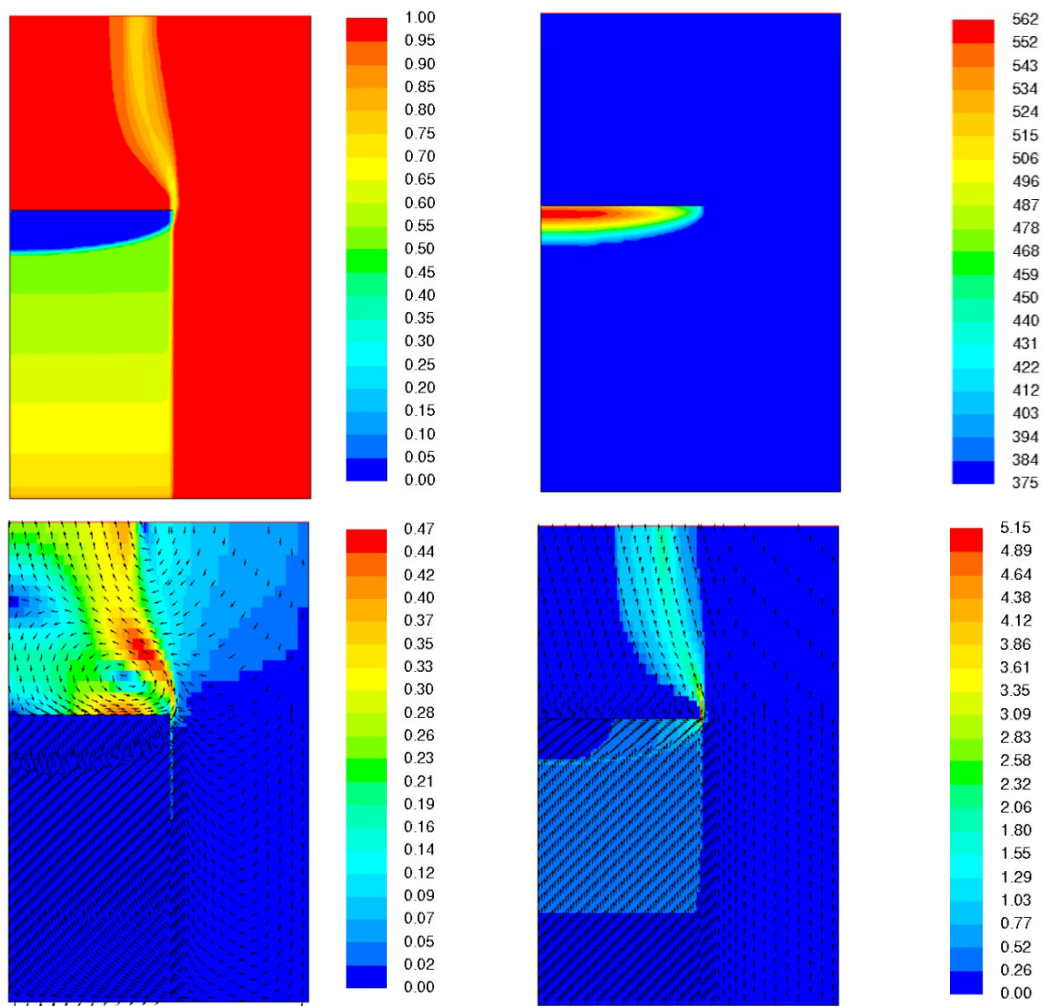


Fig. 41. CFD simulation results for the laterally flooded cylinder. Top row, left: liquid saturation, top row, right: particle temperature (K), bottom row, left: magnitude of the physical liquid velocity (m/s) with constant-length velocity vectors, bottom row, right: magnitude of the physical gas velocity (m/s) with constant-length velocity vectors. The MTD model applied ( $P = 10$  kW,  $p = 1.3$  bar).



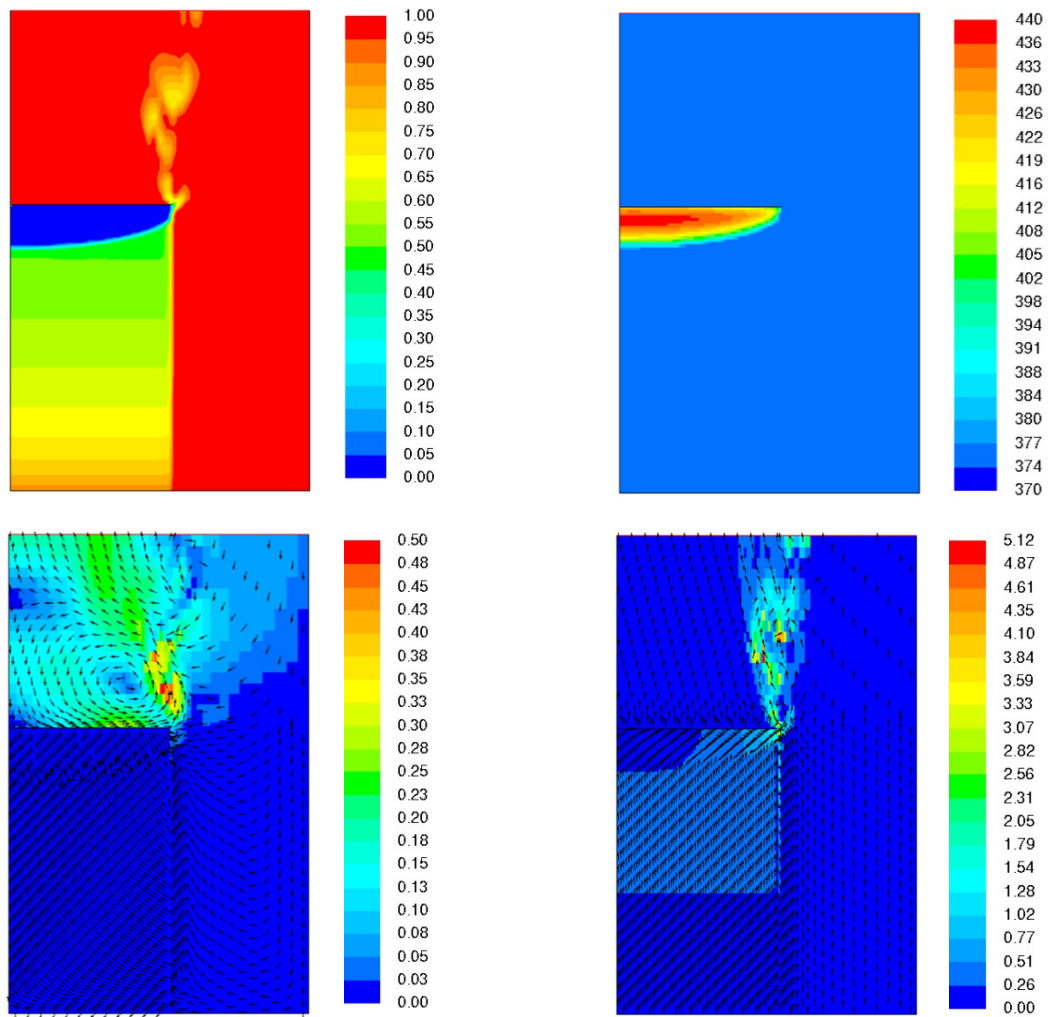


Fig. 42. CFD simulation results for the laterally flooded cylinder. Top left: liquid saturation, top right: particle temperature (K), bottom left: magnitude of the physical liquid velocity (m/s) with constant-length velocity vectors, bottom right: magnitude of the physical gas velocity (m/s) with constant-length velocity vectors. The Reed model is applied ( $P = 10 \text{ kW}$ ,  $p = 1.3 \text{ bar}$ ).

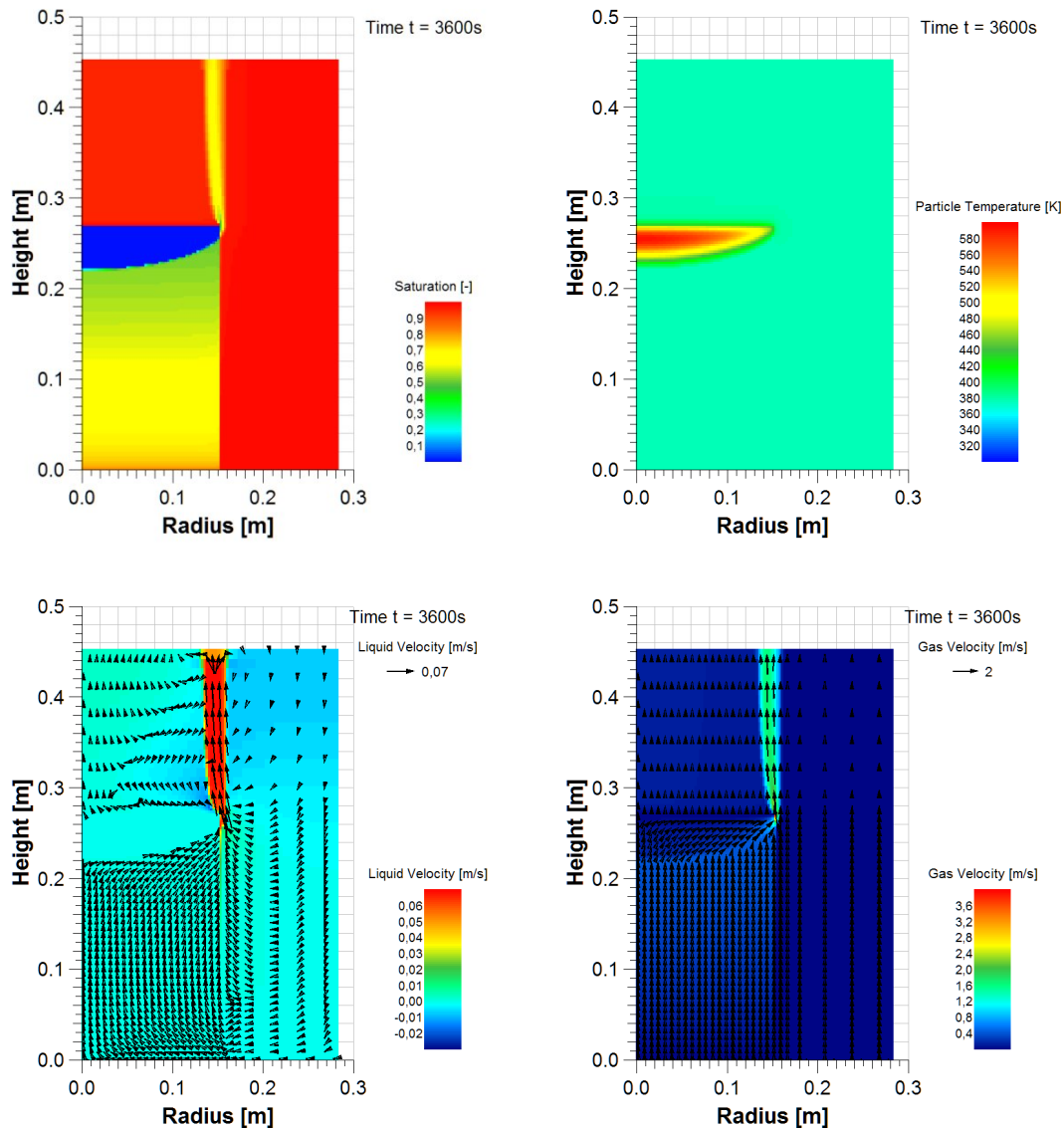


Fig. 43. MEWA results of the laterally flooded cylinder at 10 kW with the MTD model. Top left: liquid saturation, top right: particle temperature, bottom left: velocity vectors and magnitude of the axial liquid velocity, bottom right: velocity vectors and magnitude of the axial gas velocity ( $p=1.1$  bar).

### 5.3 Summary

The comparison of the CFD model predictions and the analytical and MEWA results in cases that can be treated as one-dimensional (the 1D verification model and the cylindrical test bed) suggests that the frictional pressure loss and heat transfer models have been successfully implemented into the CFD approach. Also, the CFD results of the fully flooded and laterally flooded cylinders show similar type of model and geometry dependency as the MEWA results.

A comprehensive assessment was performed for the conical bed geometry in which the dryout is formed locally in the tip of the cone. Compared to the MEWA simulation, the minimum dryout power is reached earlier but, at power levels exceeding the minimum dryout

power (post-dryout conditions) the dry zone is not significantly larger. The results are somewhat sensitive to the computational mesh and to the differences in the numerical solution methods of the two separate codes.

It was found that the 3D model yields results in a qualitative agreement with the 2D results. This indicates that the CFD approach is on a mature enough level to be applied to non-symmetric geometries not scalable to 3D, at least on the level allowed by the presently available physical models for isotropic porous media.

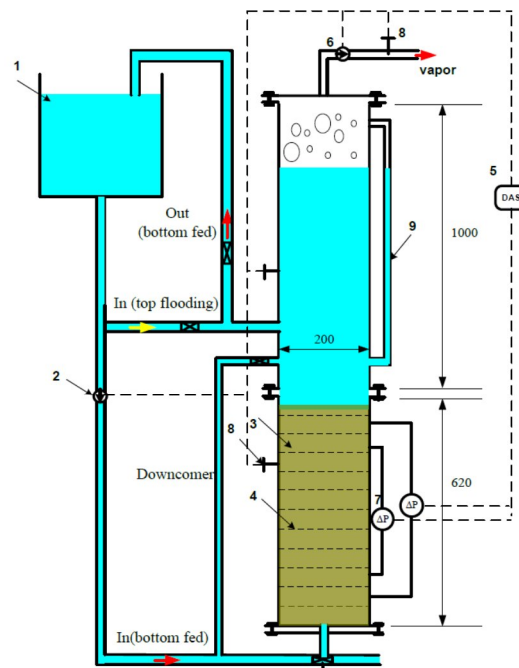
A problem with the highly local dryout zone (in principle, could be captured by a single grid cell) is that such a dryout is not seen in the experiments due to the limited number of measurements. Also, it does not seem likely that a small dryout zone in case of multi-dimensionally flooded geometry would spread uncontrollably if the excess power is moderate (coarsely below 1.5 times the minimum dryout power). Based on this, it is not well-established to attempt to fully eliminate zero saturation in the simulations to verify coolability. A suggested improved approach would consist of taking into account the size of the dryout zone (possibly cooled by the steam flow) and the associated increase of particle temperature, i.e. to answering the question does the temperature increase up to the debris re-melting temperature in different conditions.



## 6. Experimental DHF comparisons (POMECO and COOLOCE)

Debris bed coolability experiments were carried out with two different test facilities and using two types of simulant materials. The POMECO-HT test facility is operated by KTH (Royal Institute of Technology, Sweden) and the COOLOCE facility by VTT Technical Research Centre of Finland. Both facilities have been designed for measuring dryout in porous particle beds which simulate the core debris bed in a postulated severe accident in a Nordic boiling water reactor.

The POMECO-HT facility consists of the thermally-insulated porous bed test section with a water tank above it and a system to supply water for top and bottom flooding, while COOLOCE is a pool type test facility where the porous bed is submerged in water in a pressure vessel. Even though decay heat is simulated by electrical resistance heating in both facilities, the heater set-up is one of the main differences in the two test facilities. In POMECO-HT, the heaters are oriented horizontally and, in COOLOCE, the orientation is vertical (a choice originally made because of difficulties to install horizontal heaters in a conical test bed). The schematics of the test facilities are illustrated in Fig. 44 and Fig. 45. The main specifications and differences of the test bed sections are presented in Table 8.



- 1-water tank, 2-water flowmeter, 3-particle bed, 4-heaters, 5-data acquisition system,  
6-steam flowmeter, 7-pressure transducer, 8-thermocouples, 9-water level gauge

Fig. 44. Schematic of the POMECO-HT facility (Kudinov et al. 2013).

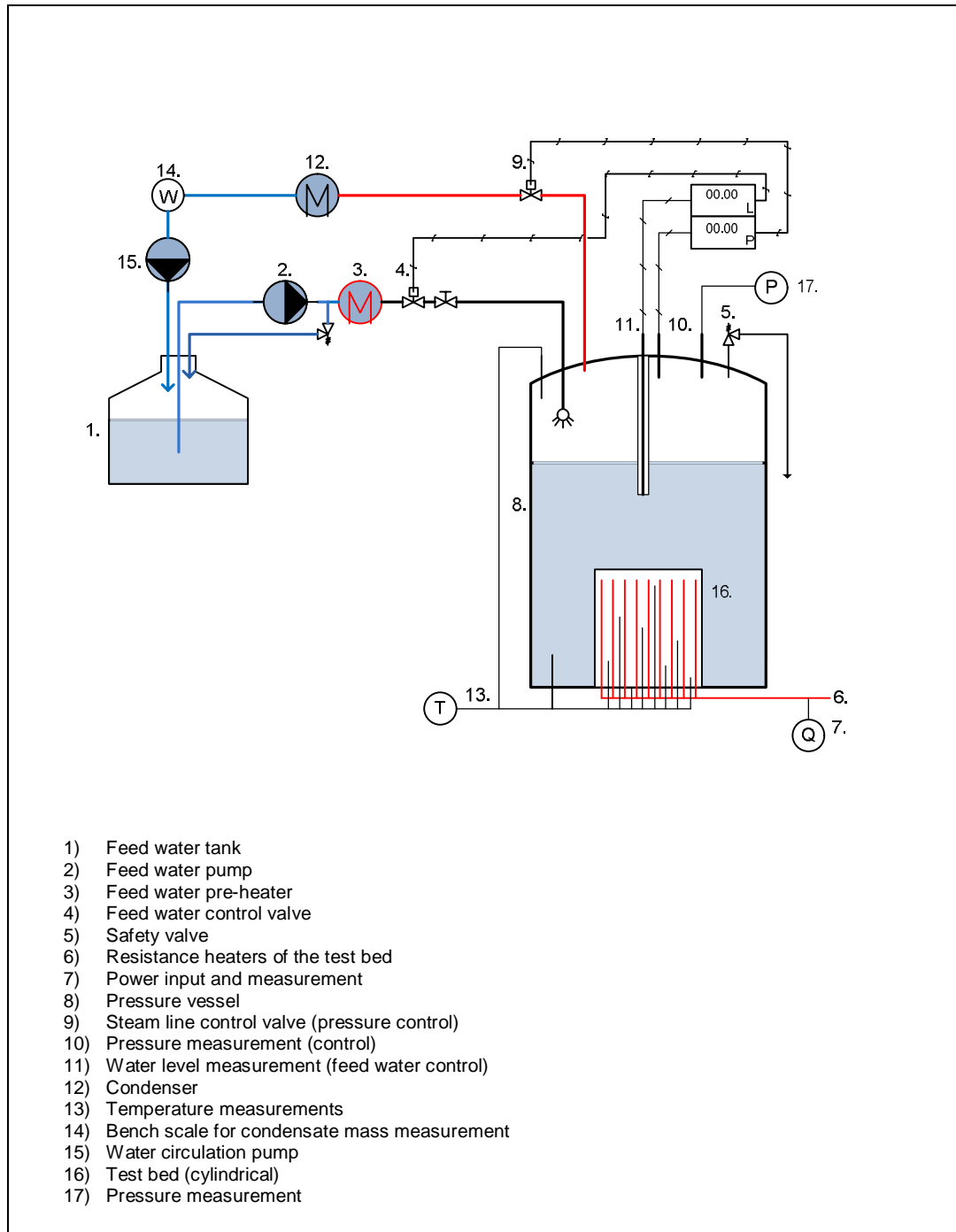


Fig. 45. Schematic of the COOLOCE facility (cylindrical test bed).

Table 8. The main specifications of the POMECO-HT and COOLOCE test beds.

	POMECO-HT	COOLOCE
Cross-section	200 x 200 mm square	155 mm radius, circular
Height	250 mm (max. 620 mm)	270 mm (fixed)
Heater radius	3 mm	6.3 mm
Test bed volume	10 l	20 l
Number of TCs	48 (max. 96)	70
% of total volume occupied by heaters and TCs	0.7	2.5

Dryout heat flux (DHF) was measured with both facilities for the following simulant materials: spherical zirconia/silica beads and irregularly-shaped alumina gravel. The ceramic beads have been used in most of the COOLOCE experiments and the alumina gravel in one COOLOCE experiment and in the STYX experiments, also by VTT.

The starting point in the assessment of the debris bed coolability is that the debris bed is homogeneously heated, as in the case of real debris with internal heat source. Another typical assumption in the modelling of a real debris bed – an experimental bed or a reactor scenario - is that the structure of the debris bed is homogeneous (isotropic) which means that single representative values for particle size and porosity are applicable throughout the debris as if the bed was monodisperse. The representative particle size can be derived from the size *distribution* of the bed particles and the logical choice for the representative porosity is the actual, carefully measured value of the bed porosity.

The requirement of homogeneous heating is not perfectly fulfilled with experimental facilities that utilize resistance heating with “cold” particles. Unless the heaters can be manufactured to imitate the shape of the bed particles, the presence of heaters inevitably causes anisotropy in the test bed. The thermocouples used to detect dryout have a similar effect. Moreover, the steam generation in the debris bed is not uniform but localized to the vicinity of the heaters. It is important that the disturbance caused by the heating arrangement, i.e. the anisotropy and the localized heating, is within acceptable boundaries. The effect of the heating arrangement (and the instrumentation in general) may be tested by direct comparisons of different experiments and comparing the experimental results to model predictions of the behaviour of isotropic porous media.

The objective of the experiments performed at KTH with POMECO-HT with the particle materials used in the COOLOCE experiments was to produce comparison data for estimating the effect of the heating arrangements and other test set-up related differences on the DHF measurement. Ideally, the DHF measured in the COOLOCE and POMECO-HT facilities is the same when the same simulant material is used and it is in good agreement with predictions given by well-established porous media models (fits to the two-phase version of the Ergun’s equation). Preceding the experiments, the suspected main source of deviation from the homogeneous configuration in the COOLOCE facility was the vertical orientation of the heaters; the increased porosity in the vicinity of the heaters would form “channels” through which steam could easily escape. In the case of horizontal heaters, the steam generation would still be local but, in the absence of vertical channels, the steam could be more evenly distributed in the test bed.

## 6.1 Results

### 6.1.1 Size measurements of spherical particles

The DHF measurement with POMECO-HT was conducted at atmospheric pressure. In COOLOCE, the pressure was increased by 0.1 bar due to counter-pressure in the steam line of the test facility (completely unpressurized conditions are unreachable with normal steam flow rates). KTH performed a pre-test measurement for the determination of the effective particle diameter using the two-phase flow loop facility POMECO-FL (Thakre et al. 2013). The effective diameter is the particle diameter obtained in a single-phase pressure loss measurement by fitting the measured pressure loss into the Ergun’s equation. The effective particle diameter according to this measurement was **0.8 mm** and the POMECO-FL test bed porosity was **0.399**. In the POMECO-HT experiment the, the test bed porosity was **0.371**.

Interestingly, the effective particle diameter is quite small considering the particle size distribution. A sample of about 1000 particles processed by image analysis at VTT showed that the mean particle size is **0.97 mm** with the standard deviation of 0.065 mm. A similar

analysis conducted for the ceramic beads at KTH (nominally the same particles but a different patch) showed a mean of **0.95 mm** with the standard deviation of 0.07 mm. In the VTT sample, the smallest particles were 0.815 mm and the largest 1.126 m. This would mean that the effective diameter of 0.8 mm would, curiously, not be within the particle size range.

To further verify the particle size distribution, VTT had samples of the particles measured with an analyser based on laser diffraction. The analyser measures the intensity of light scattered as a laser beam passes through a dispersed particulate sample. The volume-based size of the particles is calculated from the scattering pattern. According to this measurement, the volume mean of the particles is **0.975 mm** and the surface mean is **0.960 mm**. These are rather similar to the image processing results. The size distribution is shown in Fig. 46.

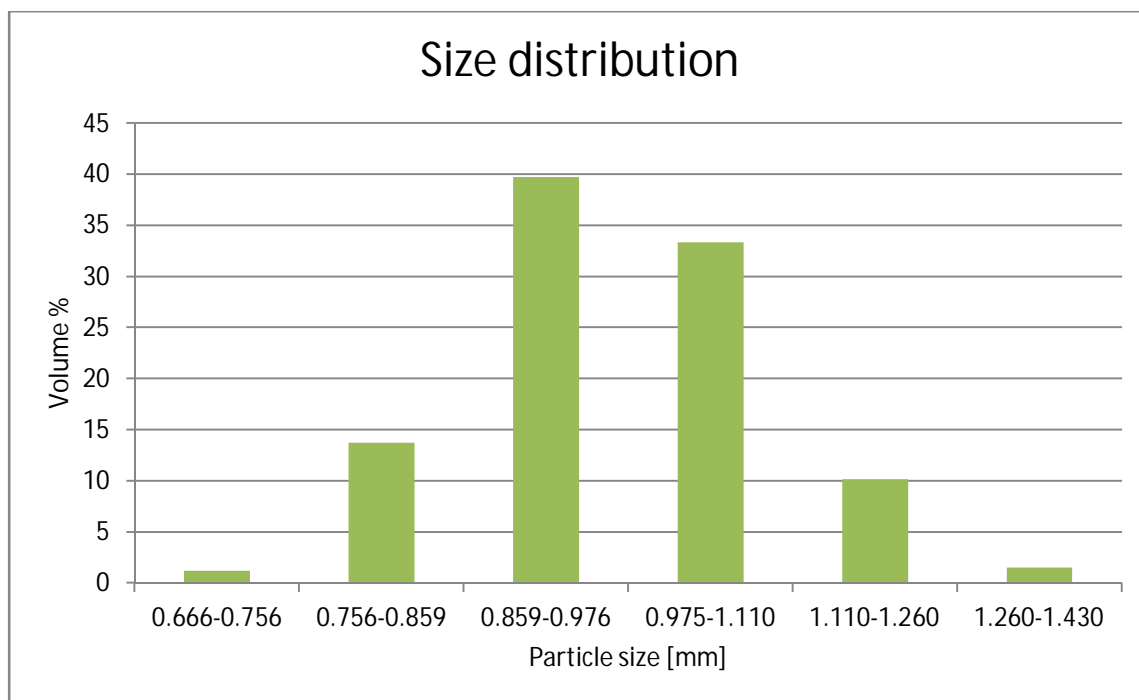


Fig. 46. Particle size distribution measured with laser diffraction analyser.

The main difference compared to the image analysis is that the measured size distribution is larger. Very small amounts (0.03-0.12%) of particles were even found in the size classes smaller than 0.666 mm and larger than 1.430 mm. Because visual inspections have not revealed any very small or very large beads, we believe that the extremes of the distribution might be caused by occasional impurities in the sample, or the conglomeration of several beads (sometimes seen in particles removed from the test facility). Of course, the same impurities are present in the experimental test bed.

The porosity of the cylindrical COOLOCE test bed is **0.390** based on the weight of the particles in the test bed and the particle density measured with a beaker. The heaters are not calculated as part of the porous matrix, the volume of the heaters has been subtracted from the total volume for which the porosity is calculated. Note that there is some uncertainty in this value: the density of the particle material is approximate which might cause an error the order of 1-2 % unit in the porosity. By filling the test bed with water prior to experiments, the porosity of **0.381** was obtained.

## 6.2 DHF results and comparisons

The measured DHF in POMECO-HT was 161.8 kW/m<sup>2</sup> and in the two measurements conducted with COOLOCE 270 kW/m<sup>2</sup> and 252 kW/m<sup>2</sup>. Clearly, the COOLOCE results were not reproduced in the POMECO-HT experiments as the difference is as high as 90 - 108 kW/m<sup>2</sup>. Three possible differences in the test set-ups which could explain the observed difference in DHF can be identified:

1. pressure
2. porosity
3. heater arrangement, test bed anisotropy and other facility-specific factors, e.g. test procedure and instrumentation

Next, we investigate the possible contribution of porosity and pressure difference. If these can be identified, the remaining unexplained difference is caused by the heating arrangement and other facility and measurement specific factors. At this point, it is worth mentioning that the heater arrangement and the resulting test bed anisotropy are not the only differences between POMECO and COOLOCE facilities. The two facilities have been designed independently from each other, the test procure has been independently decided within the two organizations and, also, the performance of the data acquisition systems may differ. The possible effect of these differences is not presently known.

System pressure has an effect on DHF through fluid properties and latent heat. As a rule, DHF and coolability increase with increasing pressure. Porosity (as well as particle size) has a significant effect on DHF; for greater porosity, the cross-section available for fluid flow is greater and fluid particle drag is reduced. This increases coolability. Here, we estimate the effects of pressure and porosity by varying these parameters and solving the DHF for each case using the classical drag force laws based on the Ergun's equation. The DHF is solved analytically from the momentum and mass balance by assuming that the debris bed is one-dimensional and uniformly heated.

### 6.2.1 Analytical solution method

The one-dimensional single-phase pressure loss in porous media is obtained by the Ergun's equation:

$$\frac{dP}{dz} = \frac{\mu}{K} j + \frac{\rho}{\eta} |j| j \quad (39)$$

where  $\rho$  is density (kg/m<sup>3</sup>),  $\mu$  is viscosity (Pa-s),  $j$  is superficial velocity (m/s),  $K$  is permeability (m<sup>2</sup>) and  $\eta$  is passability (m). The Ergun's model is extended to two-phase flow as described in Section 3 by relative permeability and relative passability,  $K_{rl}$  and  $\eta_{rl}$  for liquid, and  $K_{rg}$  and  $\eta_{rg}$  for gas. By using this model for the pressure loss, the one-dimensional momentum equations may be written as

$$-\frac{dP}{dz} - \rho_l g = \frac{\mu_l}{K K_{rl}} j_L + \frac{\rho_l}{\eta \eta_{rl}} |j_L| j_L - \frac{F_i}{1 - \alpha} j_r \quad (40)$$

$$-\frac{dP}{dz} - \rho_g g = \frac{\mu_g}{K K_{rg}} j_g + \frac{\rho_g}{\eta \eta_{rg}} |j_g| j_g - \frac{F_i}{\alpha} j_r \quad (41)$$

where  $j_r$  is relative velocity (m/s),  $\alpha$  is void fraction (-) and  $F_i$  is the interfacial drag (N/m). The single-phase and relative permeabilities and passabilities are as described in Section 3.

The one-dimensional, time-independent mass conservation equations for the two-phases are

$$\rho_L \frac{dj_L}{dz} = -\Gamma \quad (42)$$

$$\rho_G \frac{dj_G}{dz} = \Gamma \quad (43)$$

where  $\Gamma$  is evaporation rate (kg/m<sup>3</sup>/s). In steady-state conditions for a top-flooded bed, the superficial phase velocity corresponds to the evaporation mass flow rate and it is a function of height:

$$j_l = -\frac{Qz}{\rho_l \Delta H_{evap}} \quad (44)$$

$$j_g = \frac{Qz}{\rho_g \Delta H_{evap}} \quad (45)$$

In these conditions, the heat flux  $q$  (W/m<sup>2</sup>) through a horizontal cross-section of the bed is the power density  $Q$  (W/m<sup>3</sup>) multiplied by the height of the cross-section ( $q = Qz$ ). The maximum void fraction is reached at the top. By neglecting the interfacial friction and eliminating the pressure gradient, the momentum balance can be expressed with the following equation:

$$(\rho_l - \rho_g)g = \left( \frac{\mu_G}{KK_{rG}} j_G + \frac{\rho_G}{\eta \eta_{rG}} |j_G| j_G \right) - \left( \frac{\mu_L}{KK_{rL}} j_L + \frac{\rho_L}{\eta \eta_{rL}} |j_L| j_L \right) \quad (46)$$

The heat flux for any void fraction between 0 and 1 can be solved from Eq. (46) after inserting the expressions for superficial velocities and the permeabilities and passabilities. In this void fraction interval a single maximum value for the heat flux exists. This is the maximum heat flux that has a steady-state solution for the mass and momentum conservation equations. The absence of a steady-state is interpreted as the onset of dryout which means that the maximum heat flux yielded by this function is the DHF. Thus, the DHF for 1-D bed can be calculated with moderate effort by finding the maximum heat flux in the void fraction range.

## 6.2.2 Analytical and experimental DHFs

First, let us examine how well the experimental DHFs are predicted by the models when the “best estimates” of particle size and porosity presented above are applied. Fig. 47 shows the DHF measured experimentally and the DHF calculated by using Eq. 9 and the Reed drag force model ( $n=3$ ,  $m=5$ ). It is seen that the result of the POMECO-HT experiment can be well predicted with this model by applying the measured bed porosity and the effective particle diameter measured with the POMECO-FL facility (although the porosity was greater in POMECO-FL).

Then, of course, this calculation underestimates the COOLOCE DHF which was about 40% higher. The difference in porosity from 0.371 to 0.390 is not enough to explain the difference as shown by the cases in Fig. 47. However, it is seen that if – instead of the effective particle diameter – the mean diameter of 0.97 mm and the porosity of 0.390 is applied, the model produces a DHF very close to the one measured by VTT. The best result for the COOLOCE facility is reproduced with the actual porosity, and the particle diameter straightforwardly obtained from the particle size distribution. The pressure difference of 0.1 bar has been taken



into account in the calculations (as a change of material properties). The experimental DHF value is taken as the average of the two COOLOCE measurements, 261 kW/m<sup>2</sup>.

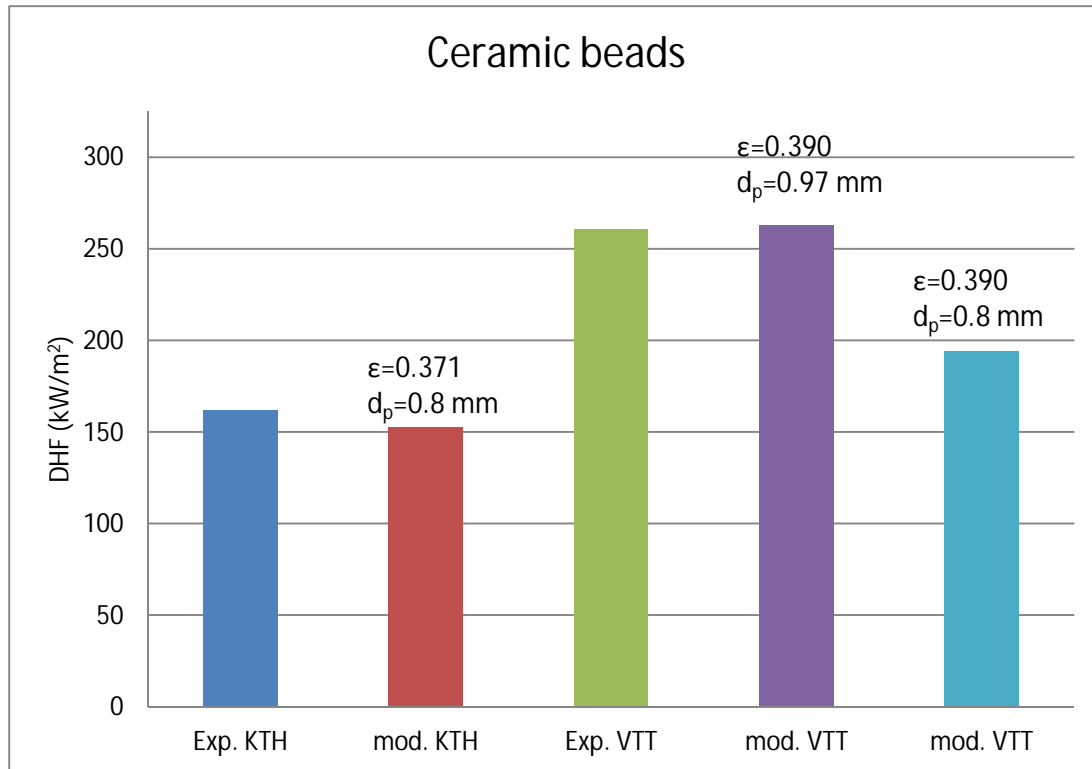


Fig. 47. Comparison of POMECO-HT (KTH) and COOLOCE (VTT) DHFs and the predictions obtained by the analytical solution with the Reed drag force model.

In addition to the physical parameters such as porosity and particle size, the drag force models, i.e. the powers of the void fraction in relative permeability and passability, have an effect on coolability. This is demonstrated in Fig. 48 which shows the comparison of the COOLOCE DHF to the calculated results with the different classical models. The experimental result is closest to the result by the Reed model. The results of the parameter variations with which we may quantify the possible contributions of pressure difference, particle size and porosity to the observed DHF difference (assuming that the aforementioned classical model is reliable) are presented in Fig. 49.

The difference between POMECO-HT and COOLOCE DHFs is about 100 kW/m<sup>2</sup>. According to the model, the porosity difference between the two test facilities could explain about 40 kW/m<sup>2</sup> and the pressure difference about 10-15 kW/m<sup>2</sup>. This leaves about 45-50 kW/m<sup>2</sup> of unexplained difference associated to the test conditions. By adjusting the particle size in the model from 0.8 mm to 0.97 mm, this difference can be covered, still within the size range of the particles which demonstrates the high sensitivity of DHF to particle size. However, for the purpose of the comparison experiment, the particle size cannot be considered an adjustable parameter because the same particle material has been used in POMECO-HT and COOLOCE (although there may be minor shifts in the particle properties between different batches). The same is true for the two-phase flow model parameters. For instance, taking the effective particle diameter of 0.8 mm for both test facilities, a calculation exercise shows that the Lipinski model would be slightly more suitable for the COOLOCE experiments as it yields a greater DHF by about 14 kW/m<sup>2</sup> compared to the Reed model but this is not informative of the possible causes of the DHF difference.

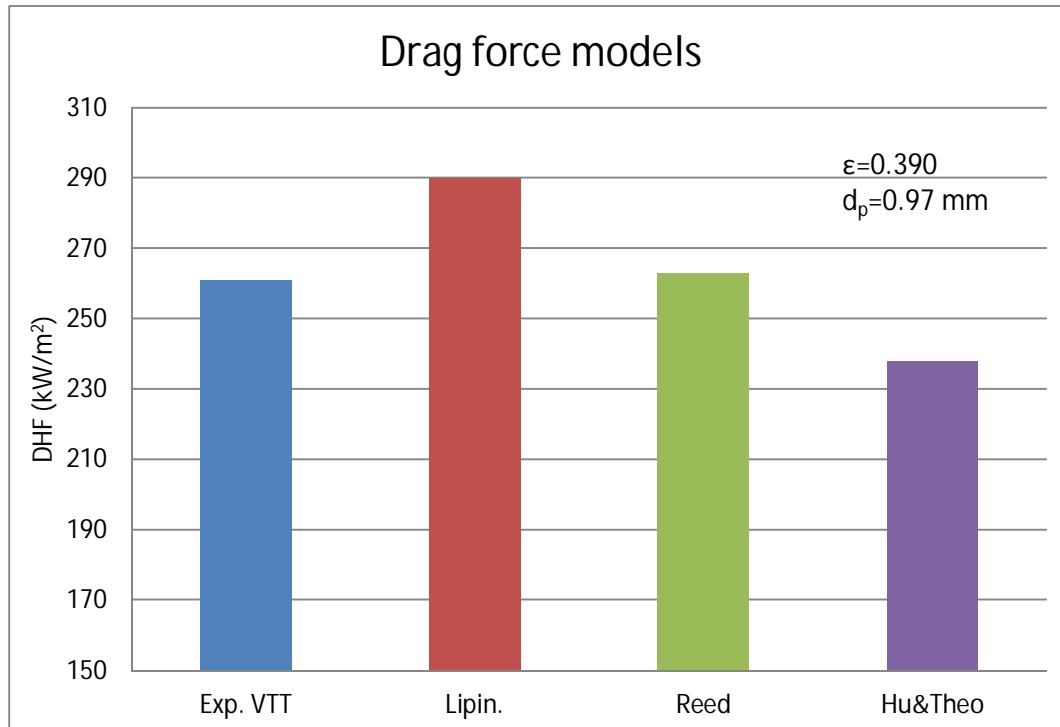


Fig. 48. Comparison of the experimental result and predictions by the different drag force models.

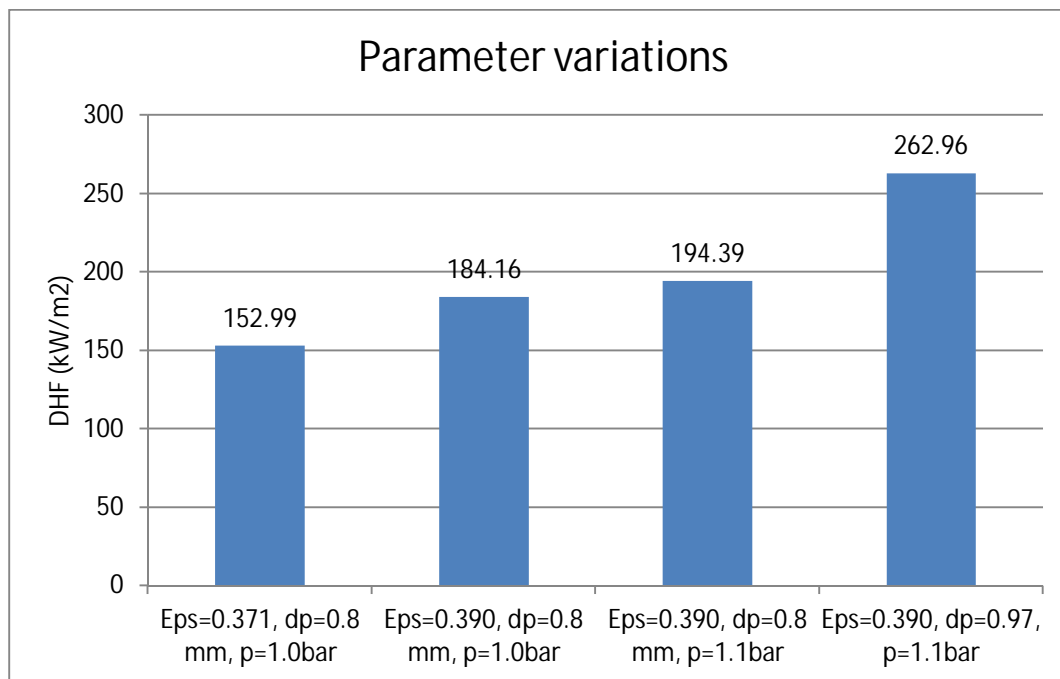


Fig. 49. Effect of pressure and porosity on DHF according to the analytical model (Reed drag force model).

## 6.3 Summary

The measured DHF in the COOLOCE and POMECO-HT test facilities under top flooding conditions showed a notable difference even though the same particle material was used; the POMECO DHF was about 40% lower. An analysis based on the classical models for predicting 1-D debris bed coolability suggests that the known porosity and pressure differences in the test conditions do not fully explain the DHF difference. Corrected with the estimated contributions of these differences, the POMECO DHF is about 20% lower than the one in COOLOCE. This may be caused by the greater volume and the different heater orientation in COOLOCE.

It is of interest to notice that – regardless of the notable difference – a good agreement between experimental and analytical results for both test facilities can be obtained by applying two different methods for defining the representative particle diameter. The best results for the COOLOCE experiments were straightforwardly given by the average diameter. For POMECO-HT, the best agreement is found by a smaller diameter; the effective diameter obtained from fitting a single-phase pressure loss into the Ergun's equation. The difference in these two diameters, being only 0.17 mm, is adequate to increase the DHF by about 20% due to the sensitivity of the DHF to particle size. In general, the uncertainty caused by the test arrangement is coarsely of the same magnitude than the uncertainty related to particle diameter and porosity.

A concern with the effective diameter obtained by single-phase pressure loss measurements may be that the contributions of particle diameter and porosity are not distinguished. The effective particle diameter depends on both pressure loss and porosity. For a different type of single-phase flow loop, the porosity might change as a result of the pipe diameter change or instrumentation. Then, the DHF predicted by the model would change as well and the agreement with the experimental DHF data might be poorer. In addition, it has also been suggested that two separate effective diameters should be considered for the debris bed mechanical properties (determining e.g. the pressure loss) and the thermal properties (determining the dryout limit) (Chikhi et al. 2013).

## 7. Conclusions

---

In the first and second parts of the present work, the coolability of porous debris beds with different geometries (spatial distributions) have been assessed by using 2D and 3D simulation methods. The main goal was to validate the simulation codes and models against the various debris bed geometries examined in the COOLOCE experiments. The 2D simulations were conducted with the MEWA code by Stuttgart University. The 3D simulations were performed with the commercial CFD code Fluent. Both approaches utilize similar porous media models in calculating the two-phase flow and heat transfer in the porous bed.

The focus of the MEWA simulations was on the following multi-dimensionally flooded debris bed geometries: fully flooded cylinder (open sidewall and top), laterally flooded cylinder (open sidewall) and the cone on a closed cylindrical base. These geometries comprise the COOLOCE experimental series 10-12. In the Fluent simulations, the focus was on the verification of the model implementation, comparisons to MEWA results and the extension of the modelling approach to full 3D. Full 3D calculations were conducted for the conical test bed.

The results of the MEWA simulations for the fully flooded cylinder showed that the predicted dryout behaviour depends of the applied model to a greater extent than in other geometries. The best agreement with the experimentally measured dryout power was obtained with a model that does not include an explicit consideration of gas-liquid drag (Reed model). This is

somewhat contrary to expectations, and the model selection for this type of multi-dimensional flow case is not obvious. For the laterally flooded cylinder, the MEWA predictions of dryout power were overly conservative compared to the experimental results and not sensitive to the model selections. This suggests that the present models have difficulties in capturing the flow behaviour in case the role of lateral flooding is significant compared to the gravity and buoyancy controlled (co- and counter-current) flows in vertical direction. For the cone on a cylindrical base, the results are consistent with the fully conical geometry and dryout was accurately predicted by the modified Tung & Dhir model with explicit gas-liquid drag.

The qualitative agreement between the CFD results and the MEWA results was relatively good. Some differences related to numerical issues and different computational grids were seen. In case of the conical bed, the tip of the cone is more vulnerable to dryout in the CFD simulations than in the MEWA simulations. On the other hand, the temperature excursions in the CFD simulations in dryout conditions, with moderate excess power, were limited. In future studies, rather than using the formation of the first dry zone as the coolability limit, it would be reasonable to determine the long-term coolability based on the volume and temperature of the dryout zone (which would also be experimentally detectable).

The application of the free-flow models (including turbulence) to the pool region in the Fluent simulations resulted in more realistic simulation of flows in the water pool surrounding the debris bed, e.g. a more realistic slip velocity was obtained. The pool model selection has limited local effects in the porous region.

In the third part of the study, an insight into the uncertainty in the experimental determination of DHF has been provided. Experiments with a top-flooded bed have been conducted with the COOLOCE facility at VTT and the POMECO facility at KTH with the same particle material. The comparisons revealed the effect of the non-modifiable part of the test set-up such as the heating and instrumentation systems. It was found that the unexplained difference between the test facilities was about 20%, i.e. of the same order than the “typical” uncertainty from porosity and particle diameter.

## References

---

Bürger, M., Buck, M., Schmidt, W., Widmann, W. 2006. Validation and application of the WABE code: Investigations of constitutive laws and 2D effects on debris coolability. Nuclear Engineering and Design 236 (2006), pp. 2164-2188.

Chikhi, N., Coindreau, O., Li, L.X., Ma, W.M., Taivassalo, V., Takasuo, E., Leininger, S., Kulenovic, R., Laurien, E. Evaluation of an Effective Diameter to Study Quenching and Dry-out of Complex Debris Bed. 6<sup>th</sup> European Review Meeting on Severe Accident Research (ERMSAR-2013), Avignon, France, October 2-4, 2013.

Ergun, S. 1952. Fluid flow through packed columns. Chemical Engineering Progress 48, pp. 89-94.

Fluent. 2011a. ANSYS FLUENT Theory Guide, Release 14.0, Southpointe, ANSYS, Inc.

Fluent. 2011b. ANSYS FLUENT User's Guide, Release 14.0, Southpointe, ANSYS, Inc.

Hovi, V. 2013. Porflo Development 2012, Research Report VTT-R-00991-13, Espoo, VTT.

Imura, S., Takegoshi, E. 1974. Effect of Gas Pressure on the Effective Thermal Conductivity of Pack Beds. Heat Transfer Japanese Research, Vol. 3, No. 4, 13 p.

Hu, K., Theofanous, T.G. 1991. On the measurement and mechanism of dryout in volumetrically heated coarse particle beds. *International Journal of Multiphase Flow*, 17 (No. 4).

Kudinov, P., Konovalenko, A., Grishchenko, D., Yakush, S., Basso, S., Lubchenko, N., Karbojian, A. 2013. Investigation of debris bed formation, spreading and coolability. NKS-R Report, NKS-287, August 2013. ISBN 978-87-7893-362-1.

Lienhard, J.H. 2012. *A Heat Transfer Textbook*, 4th edition. Phlogiston Press, Cambridge, Massachusetts, USA.

Lipinski, R.J., 1982. A Model for Boiling and Dryout in Particle Beds. US Nuclear Regulatory Committee, NUREG/CR-2646, SAND82-0765.

Lipinski, R.J. 1984. A coolability model for postaccident nuclear reactor debris. *Nuclear Technology*, 65, pp. 53-66.

Rahman, S. 2013. Coolability of Corium Debris under Severe Accident Conditions in Light Water Reactors. Doctoral thesis, Institut für Kernenergetik und Energiesysteme, Universität Stuttgart, IKE 2-155. ISSN-0173-6892.

Ranz, W.E., Marshall, W. R. 1952. Evaporation from drops. *Chemical Engineering Progress*, 48, pp. 141-146.

Reed, A.W. 1982. The effect of channeling on the dryout of heated particulate beds immersed in a liquid pool. Doctoral Thesis, Department of Mechanical Engineering, Massachusetts Institute of Technology, 1982.

Rohsenow, W. 1952. A method of correlating heat transfer data for surface boiling of liquids. *Trans. ASME*, 74, pp. 969-976.

Schiller, L., Naumann, Z.Z. 1935. A drag coefficient correlation. *Ver. Deutsch. Ing.*, 77, pp. 318-325.

Schmidt, W. 2004. Influence of Multidimensionality and Interfacial Friction on the Coolability of Fragmented Corium. Doctoral Thesis. Institut für Kernenergetik und Energiesysteme. IKE 2-149. ISSN-0173-6892.

Schulenberg, T., Müller, U. 1986. A refined model for the coolability of core debris with flow entry from the bottom. *Proceedings of the Sixth Information Exchange Meeting on Debris Coolability*. EPRI NP-4455. Los Angeles, March 1986.

Takasuo, E., Holmström, S., Kinnunen, T., Pankakoski, P.H. 2012a. The COOLOCE experiments investigating the dryout power in debris beds of heap-like and cylindrical geometries. *Nuclear Engineering and Design*, 250, pp. 687-700.

Takasuo, E., Kinnunen, T., Holmström, S. 2012b. COOLOCE particle bed coolability experiments with a cylindrical test bed: Test series 8-9. Research report VTT-R-07224-12. 44 p.

Takasuo, E., Holmström, S., Kinnunen, T., Pankakoski, P.H., Hovi, V., Ilvonen, M., Rahman, S., Bürger, M., Buck, M., Pohlner, G. 2012c. Experimental and Computational Studies of the Coolability of Heap-like and Cylindrical Debris Beds. 5<sup>th</sup> European Review Meeting on Severe Accident Research (ERMSAR-2012), Cologne, Germany, March 21-23, 2012.



Takasuo, E., Kinnunen, T., Holmström, S, Lehtikuusi, T. 2013a. COOLOCE coolability experiments with a cylindrical debris bed and lateral flooding: COOLOCE-10. Research Report VTT-R-0463-13. 16 p.

Takasuo, E., Kinnunen, T., Holmström, S, Lehtikuusi, T. 2013b. COOLOCE debris bed coolability experiments with an agglomerate simulant: Test series 11. Research Report VTT-R-03316-13. 22 p.

Takasuo, E., Kinnunen, T., Lehtikuusi, T. 2013c. COOLOCE-12 debris bed coolability experiment: Cone on a cylindrical base. Research Report VTT-R-07967-13. 18 p.

Thakre, S., Ma, W., Kudinov, P., Bechta, S. Study on Effective Particle Diameters and Coolability of Particulate Beds Packed with Irregular Multi-size Particles. NKS-DECOSE Report-2/2012 2013-06-17.

Tung, V.X. and Dhir, V.K., 1988. A Hydrodynamic Model for Two-Phase Flow through Porous Media. International Journal of Multiphase Flow, 14, No. 1, pp. 47-65.

Vortmeyer, D. 1978. Radiation in Packed Solids. 6th International Heat Transfer Conference, Toronto, Canada, 1978.

Title	A study on the coolability of debris bed geometry variations using 2D and 3D models
Author(s)	Eveliina Takasuo, Veikko Taivassalo, Ville Hovi
Affiliation(s)	VTT Technical Research Centre of Finland
ISBN	978-87-7893-393-5
Date	June 2014
Project	NKS-R / DECOSE
No. of pages	66
No. of tables	8
No. of illustrations	49
No. of references	28
Abstract max. 2000 characters	<p>In the first and second parts of the present work, the coolability of porous debris beds with different geometries (spatial distributions) has been assessed by using 2D and 3D simulation methods. The 2D simulations were conducted with the MEWA code by Stuttgart University. The 3D simulations were performed with the commercial CFD code Fluent, after the implementation of the porous media models as user defined functions into the code. The focus of the MEWA simulations was on the following multi-dimensionally flooded debris bed geometries: fully flooded cylinder (open sidewall and top), laterally flooded cylinder (open sidewall) and the cone on a closed cylindrical base. These geometries comprise the COOLOCE experimental series 10-12. In the Fluent simulations, the focus was on the verification of the model implementation, comparisons to MEWA results and the extension of the modelling approach to full 3D. Full 3D calculations were conducted for the conical test bed. In the third part, an insight into the uncertainty in the experimental determination of DHF is provided. Experiments with a top-flooded bed have been conducted with the COOLOCE facility at VTT and the POMECO facility at KTH with the same particle material. The comparisons revealed the effect of the non-modifiable part of the test set-up such as the heating and instrumentation systems.</p>
Key words	severe accident, debris bed, coolability, numerical simulation, CFD